Helmholtz-Zentrum Berlin für Materialien und Energie und Institut für Physik,
Universität Potsdam

Control over spin and electronic structure of MoS_2 monolayer via interactions with substrates

Dissertation
zur Erlangung des akademischen Grades
"doctor rerum naturalium" (Dr. rer. nat.)
in der Wissenschaftsdisziplin Experimentalphysik

eingereicht an der
Mathematisch-Naturwissenschaftlichen Fakultät
der Universität Potsdam

von
Vladimir Voroshnin

Universität Potsdam, 2023

Hauptbetreuer*in:	apl. Prof. Dr. Oliver Rader
Betreuer*innen:	Dr. Alexander Fedorov
Gutachter*innen:	apl. Prof. Oliver Rader, Prof. Denis Vyalikh, Prof. Laubschat Clemens
Day of the defense:	March 14th, 2023

Signature from head of PhD committee:

Published online on the
Publication Server of the University of Potsdam:
https://doi.org/10.25932/publishup-59070
https://nbn-resolving.org/urn:nbn:de:kobv:517-opus4-590709

Abstract

The molybdenum disulfide (MoS_2) monolayer is a semiconductor with a direct bandgap[1] while it is a robust and affordable material. It is a candidate for applications in optoelectronics[2] and field-effect transistors[3]. MoS_2 features a strong spin-orbit coupling which makes its spin structure promising for acquiring the Kane-Mele topological concept[4] with corresponding applications in spintronics and valleytronics [5, 6].

From the optical point of view, the MoS_2 monolayer features two valleys in the regions of $\overline{\mathrm{K}}$ and $\overline{\mathrm{K}'}$ points. These valleys are differentiated by opposite spins and a related valley-selective circular dichroism[7, 8].

In this study we aim to manipulate the MoS_2 monolayer spin structure in the vicinity of the $\overline{\mathrm{K}}$ and $\overline{\mathrm{K}'}$ points to explore the possibility of getting control over the optical and electronic properties. We focus on two different substrates to demonstrate two distinct routes: a gold substrate to introduce a Rashba effect and a graphene/cobalt substrate to introduce a magnetic proximity effect in MoS_2.

The Rashba effect[9] is proportional to the out-of-plane projection of the electric field gradient. Such a strong change of the electric field occurs at the surfaces of a high atomic number materials and effectively influence conduction electrons as an in-plane magnetic field. A molybdenum and a sulfur are relatively light atoms, thus, similar to many other 2D materials, intrinsic Rashba effect in MoS_2 monolayer is vanishing small. However, proximity of a high atomic number substrate may enhance Rashba effect in a 2D material as it was demonstrated for graphene previously[10].

Another way to modify the spin structure is to apply an external magnetic field of high magnitude (several Tesla)[11], and cause a Zeeman splitting, the conduction electrons. However, a similar effect can be reached via magnetic proximity [12, 13] which allows us to reduce external magnetic fields significantly or even to zero. The graphene on cobalt interface is ferromagnetic [14] and stable for MoS_2 monolayer synthesis. Cobalt is not the strongest magnet; therefore, stronger magnets may lead to more significant results.

Nowadays most experimental studies on the dichalcogenides (MoS_2 included) are performed on encapsulated heterostructures that are produced by mechanical exfoliation[7, 11, 15]. While mechanical exfoliation (or scotch-tape method) allows to produce a huge variety of structures, the shape and the size of the samples as well as distance between layers in heterostructures are impossible to control reproducibly. In our study we used molecular beam epitaxy (MBE) methods to synthesise both MoS_2/Au(111) and MoS_2/graphene/Co systems. We chose to use MBE, as it is a scalable and reproducible approach, so later industry may adapt it and take over.

We used graphene/cobalt instead of just a cobalt substrate because direct contact of MoS_2 monolayer and a metallic substrate may lead to photoluminescence (PL) quenching[16–18] in the metallic substrate. Graphene and hexagonal boron nitride monolayer are considered building blocks of a new generation of electronics also commonly used as encapsulating materials for PL studies[19]. Moreover graphene is proved to be a suitable substrate for the MBE growth of transitional metal dichalcogenides (TMDCs)[20].

In chapter 1, we start with an introduction to TMDCs. Then we focus on MoS_2 monolayer state of the art research in the fields of application scenario; synthesis approaches; electronic, spin, and optical properties; and interactions with magnetic fields and magnetic materials. We briefly touch the basics of magnetism in solids and move on to discuss various magnetic exchange interactions and magnetic proximity effect. Then we describe MoS_2 optical properties in more detail. We start from basic exciton physics and its manifestation in the MoS_2 monolayer. We consider optical selection rules in the MoS_2 monolayer and such properties as chirality, spin-valley locking, and coexistence of bright and dark excitons.

Chapter 2 contains an overview of the employed surface science methods: angle-integrated, angle-resolved, and spin-resolved photoemission; low energy electron diffraction and scanning tunneling microscopy.

In chapter 3, we describe MoS_2 monolayer synthesis details for two substrates: gold monocrystal with (111) surface and graphene on cobalt thin film with Co(111) surface orientation. The synthesis descriptions are followed by a detailed characterisation of the obtained structures: fingerprints of MoS_2 monolayer formation; MoS_2 monolayer symmetry and its relation to the substrate below; characterisation of MoS_2 monolayer coverage, domain distribution, sizes and shapes, and moiré structures.

In chapter 4, we start our discussion with MoS_2/Au(111) electronic and spin structure. Combining density functional theory computations (DFT)

and spin-resolved photoemission studies, we demonstrate that the MoS_2 monolayer band structure features an in-plane Rashba spin splitting. This confirms the possibility of MoS_2 monolayer spin structure manipulation via a substrate. Then we investigate the influence of a magnetic proximity in the MoS_2/graphene/Co system on the MoS_2 monolayer spin structure. We focus our investigation on MoS_2 high symmetry points: $\overline{\Gamma}$ and $\overline{K}$. First, using spin-resolved measurements, we confirm that electronic states are spin-split at the $\overline{\Gamma}$ point via a magnetic proximity effect. Second, combining spin-resolved measurements and DFT computations for MoS_2 monolayer in the $\overline{K}$ point region, we demonstrate the appearance of a small in-plane spin polarisation in the valence band top and predict a full in-plane spin polarisation for the conduction band bottom.

We move forward discussing how these findings are related to the MoS_2 monolayer optical properties, in particular the possibility of dark exciton observation. Additionally, we speculate on the control of the MoS_2 valley energy via magnetic proximity from cobalt. As graphene is spatially buffering the MoS_2 monolayer from the Co thin film, we speculate on the role of graphene in the magnetic proximity transfer by replacing graphene with vacuum and other 2D materials in our computations.

We finish our discussion by investigating the K-doped MoS_2/graphene/Co system and the influence of this doping on the electronic and spin structure as well as on the magnetic proximity effect.

In summary, using a scalable MBE approach we synthesised MoS_2/Au(111) and MoS_2/graphene/Co systems. We found a Rashba effect taking place in MoS_2/Au(111) which proves that the MoS_2 monolayer in-plane spin structure can be modified. In MoS_2/graphene/Co the in-plane magnetic proximity effect indeed takes place which rises the possibility of fine tuning the MoS_2 optical properties via manipulation of the the substrate magnetisation[21].

This page was intentionally left empty.

To my family, colleagues and friends.

Acknowledgements

I would like to acknowledge all the friends and family members who supported me in doing a Ph.D. degree and all the colleagues who participated in the wide range of the demonstrated in this work experiments and theoretical computations.

For STM experiments and TB and DFT calculations, I asked collaborators to perform special experiments and calculations. STM experiments were kindly provided by Dr. Maxim Krivenkov, the tight-binding calculations by Dr. Niels Ehlen, and the DFT calculations by Artem Tarasov.

Contents

This page was intentionally left empty.

Abbreviations

Common abbreviations

2D, 3D	two-dimensional, three-dimensional
UHV	ultra-high vacuum
E_F	Fermi level

Methods

ARPES	angle resolved photoemission spectroscopy
CVD	chemical vapor deposition
DFT	density functional theory
LEED	low energy electron diffraction
PEEM	photoemission electron microscopy
PES	photoelectron spectroscopy
STM	scanning tunneling microscopy
TB	tight binding
XPS	x-ray photoelectron spectroscopy

Symbols, units, definitions

k_B	Boltzmann constant	$8.617\,\mathrm{eV/K}$
Å	angstrom	$10^{-10}\,\mathrm{m}$
c	speed of light in vacuum	$2.998 \times 10^{10}\,\mathrm{cm/s}$
eV	electron volt	$1.602 \times 10^{-19}\,\mathrm{J}$

This page was intentionally left empty.

Chapter 1

Transitional metal dichalcogenides and MoS_2 monolayer: state of the art

Transition metal dichalcogenides (TMDCs) are MX_2 structures where M stands for transition metals, while X stands for for chalcogens. In this work we are focusing on group VI semiconducting dichalcogenides, where M stands for Molybdenum (Mo) and Tungsten (W) and X for Sulfur (S), Selenium (Se), and Tellurium (Te)[22, 23]. Spatially, TMDCs monolayers represent a sandwich with transition metal layer between two chalcogen layers (X-M-X), where M is covalently bonded to six X atoms. They feature a hexagonal (honeycomb) lattice which is similar to graphene but with a threefold symmetry (C3)[24].

In a general context, the whole TMDCs family features diverse properties: from insulating HfS_2 and semiconducting MoS_2 to semi-metallic WTe_2 and $TeSe_2$ and then to metallic NbS_2 and VS_2. Some members, such as bulk $NbSe_2$ and TaS_2, demonstrate superconductive, charge density wave, and Mott transition[25].

The group VI TMDCs monolayers demonstrate direct band gaps of around 2 eV in the regions of $\overline{\mathrm{K}}$ and $\overline{\mathrm{K}'}$ points[26]. Moreover, in this regions, TMDCs feature spin-split band states[27] due to strong spin–orbit interaction.

Given TMDCs are not ferromagnetic and have a broken centre-symmetry, the spin splitting at opposite k values must show the opposite sign. This leads to a spin-valley locking effects[28]. Simply speaking, $\overline{\mathrm{K}}$ and $\overline{\mathrm{K}'}$ valleys correspond to excitations taking place in $\overline{\mathrm{K}}$ and $\overline{\mathrm{K}'}$ points of TMDs Brillouin zones. Due to optical selection rules circularly polarized light allows to selectively induce transitions in a particular valley: σ^+ pumps the $\overline{\mathrm{K}}$, while σ^- pumps the $\overline{\mathrm{K}'}$ valley[29]. Exited to different valleys, electrons feature an opposite spin and can hardly switch to a different valley, as it is required to swap the spin in the process.

1.1 TMDCs as building blocks

TMDCs monolayers are a branch of the large family of 2D materials and can serve as building blocks for the van-der-Waals type heterostructures[30]. The idea behind it is to stack different classes of 2D crystals on top of each other to produce electronic and optical devices. The assembled artificial pseudo-2D material has van-der-Waals-like forces which are sufficient to stabilise the stack[31].

The fundamental feature that allows silicon to have limitless application is that pure silicon is a semiconductor, while silicon dioxide easily formed on the surface and not propagating to the bulk is a dielectric. One can also dope silicon and obtain electron or hole semiconductors. It allows us to use a planar technology to take a silicon crystal as a substrate and form different types of interfaces that for further applications. The combination of 2D crystals with different electronic properties in a selected order goes with the same logic.

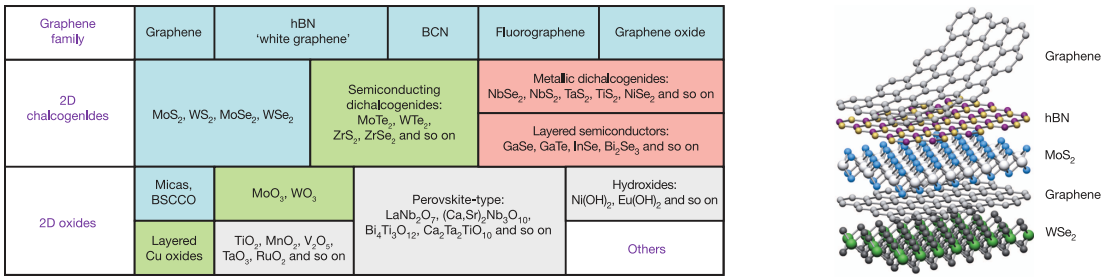

Figure 1.1: The table on the left represents a 2D library of the materials that can be potentially used for van-der-Waals heterostructures. Blue indicates monolayers stable under room temperature and ambient atmosphere. Green indicates monolayers stable under ambient atmosphere. Pink indicates unstable monolayers but with the possibility of being stable in encapsulated state. Grey indicates materials that are proved to have 2D states but with little further published information. The cartoon picture on the right visualizes the concept of atomic-scale lego- or sandwich-like assemblies. The figure and the table are adopted from Ref.[30].

Fig. 1.1 represents a 2D library of the material that looks promising for the van-der-Waals heterostructures applications. When considering such applications, one must pay attention not only to the electronic and spin properties of the materials but also to the chemical, mechanical and thermal robustness. Nowadays, the champions are graphene – a zero-gap semiconductor that can provide ballistic electron transport at room temperature – and MoS_2 monolayer – a semiconductor with a direct band gap that can provide spin-valley selective optical and spin effects. One may also perform encapsulation of chemically unstable materials to preserve their qualities while allowing the use in more severe than refined high-vacuum and low temperatures conditions.

One can see a color coding in the table in Fig. 1.1. Blue shading highlights monolayers that are stable under room temperature and ambient atmosphere. The green

color indicates the ones that are probably stable under ambient atmosphere, while the pink color indicates unstable ones but with the possibility of being stable in an encapsulated state. The grey color indicates materials that can take a 2D form but with little published information about them.

1.2 MoS_2 monolayer: state of the art

Molybdenum disulfide (MoS_2) in 2H form is stable and can be found as a natural mineral – molybdenite[32]. On the other hand, MoS_2 bulk can have three polytypes of crystallographic structure: 1T (trigonal), 2H (hexagonal), and 3R (rhombohedral). The MoS_2 monolayer was firstly reported by Frindt[33] as crystal of several molecular layers. It was obtained by a cleavage procedure and measured via electron microscopy. One must note that for MoS_2 monolayer, there are only two polymorphs: octahedral (1T or D_{3d}) and trigonal prismatic (1H or D_{3h})[25]. We will be focusing on the 1H form, as this is the one we eventually synthesized.

MoS_2 monolayer is a direct band semiconductor. The bandgap is located in the regions of $\overline{\mathrm{K}}$ and $\overline{\mathrm{K}'}$ points, and its value is around 1.8 eV. Valence and conduction band states in the region of $\overline{\mathrm{K}}$ and $\overline{\mathrm{K}'}$ points are spin split. The top valence band and the bottom conduction band states at the $\overline{\mathrm{K}}$ point feature spin-up electronic states, while those at the $\overline{\mathrm{K}'}$ point feature spin-down. An electron excitation in the regions of $\overline{\mathrm{K}}$ and $\overline{\mathrm{K}'}$ points is associated with $\overline{\mathrm{K}}$ and $\overline{\mathrm{K}'}$ valleys. The most important difference between valleys is that electrons with a particular out-of-plane spin direction can be excited in one valley. In contrast, this direction is opposite in another valley.

A sizable fundamental band gap makes the MoS_2 monolayer suitable for fabricating field effect transistors (FET). The firstly reported MoS_2 monolayer mobility at room temperature was not that promising – it was only in a range of 0.5–3 $cm^2\ V^{-1}\ s^{-1}$[34]. Six years later, a room-temperature single-layer MoS_2 transistor was demonstrated: the mobility was already 200 $cm^2\ V^{-1}\ s^{-1}$, and the current on/off ratio was 10^8[35]. However, one must remember that the transistor was assembled via the scotch-tape cleavage technique[36], which does not seem industrially scalable yet.

Having only one working transistor and a fully functional electronic device are entirely different. Authors of the publication[37] demonstrated an inverter, a NAND gate, a static random access memory, and a five-stage ring oscillator based on a direct-coupled transistor logic technology[38]. The circuits comprise 2 to 12 transistors seamlessly integrated side-by-side on a single sheet of bilayer MoS_2. A MoS_2 monolayer was also shown to be a base for an integrated circuits that can operate as inverters and perform NOR logic operations at room temperature[39]. The publication[40] demonstrates a small-signal analog amplifier that consists of two MoS_2 monolayer-based field-effect transistors integrated on the same MoS_2 flake.

Besides logical operations, a direct band gap is a building block for optical devices, such as optoelectronic circuits[2] and light sensing. The first MoS_2 monolayer-based ultrasensitive phototransistor with a broad spectral range was demonstrated in 2013[41]. The maximum photoresponsivity of 880 A W^{-1} was observed at 561 nm, while photoresponse was present in the range of 400–680 nm. Due to the 2D MoS_2 monolayer nature, an outstanding electrostatic control allows to turn off the phototransistor resulting in extremely low dark current. Such phototransistors are competitive with state-of-the-art silicon ones.

Another implementation is a light radiation device. It looks promising when considering a direct integration of 2D electroluminescent devices to nano-antennas, plasmonic structures, and photonic crystals. MoS_2, $MoSe_2$, WSe_2, and WS_2 monolayers can all be the base for light-emitting semiconductor devices[42]. Interestingly, different monolayers correspond to a different photon energy: ≈1.55 eV for $MoSe_2$, ≈1.67 eV for WSe_2, ≈1.8 eV for MoS_2, and ≈2.00 eV for WS_2. The work[42] demonstrated the possibility of fabrication of a millimeter-scale transparent device with a peak power of 193 μ W cm^{-2}.

Valley properties of dichalcogenides suggest spin- and valley- related spintronics[6] and valleytronics[5] applications. Circularly polarized photoluminescence on a MoS_2 monolayer demonstrates up to 50% spin polarization[29], confirming valley-selective circular dichroism. In other words, using circularly polarised light, one can selectively inject electrons with a particular spin into the conduction band of a MoS_2 monolayer.

Authors of Ref.[43] successfully fabricated MoS_2 on a multi-graphene layer spin valve. Via Hanle spin precession measurements, they demonstrated optical spin injection and lateral spin transport at room temperature in this system. We explicitly included this item as the last one, as we are trying to contribute to this application direction.

1.2.1 Synthesis and production

Most experimental two-dimensional devices are assembled via the scotch-tape cleavage method, pioneered first for graphene-based Van-der-Waals heterostructures[36, 44]. The method essentially stands for a micromechanical exfoliation procedure that uses scotch tape to isolate monolayers from bulk material and then mechanically assemble these monolayers on top of each other using adhesion properties. The method is widely used and serves well for the scientific study, as it is not constrained by chemical, mechanical, and temperature stabilizes of compounds while the mechanical placement of new layers on the top. However, the method is far from being adopted by the industry as it is neither reproducible nor scalable. All the "devices" obtained via this technique should be considered prototypes or proof of concept. One may see it as an MVP (minimum viable product) in business terms. Essentially this means that before building a scalable

and profitable production pipeline, one must quickly create a semi-product with a similar outcome, test its performance and collect feedback.

The chemical deposition is a relatively cheap way to produce chalcogenide thin films[45]. The general idea of the method is to mix chemical precursors and let them react and self-organize on the substrate surface under particular pressure and temperature environment. One way to do it is to deep coat a substrate in a chemical solution and then anneal it. In Ref.[46] the authors proposed the following procedure: an insulating sapphire substrate was immersed into the solution of mixed $(NH_4)_2MoS_4$ and dimethylformamide, then the substrate was slowly pulled out at 0.5 mm/s rates and baked at 120°C. Growth of a highly crystalline MoS_2 thin layer with large-area was reported. The chemical deposition method is also capable of producing doped systems. The synthesis procedure of Fe doped MoS_2 monolayer on SiO_2/Si substrate is presented in Ref.[47].

Another branch of this method is chemical vapor deposition (CVD). The idea is similar, but chemical precursors come to the substrate surface from the gas phase. In[48], authors obtained a MoS_2 monolayer on a Al_2O_3 substrate by exposing an Al_2O_3 thin film deposited on silicon to a stream of the MoO_3 and sulfur under flowing argon atmosphere at a pressure of 150 Torr. The self-assembly reaction with the formation of MoS_2 takes place at 800°C substrate temperature. Relating to our scope, MoS_2 can be obtained using graphene as a substrate[49]. A great benefit of the CVD method is that it can be catalytically constrained, meaning that the reaction stops after the full coverage is reached. On the negative side, CVD-grown films are often polycrystalline and contain a high density of grain boundaries[50, 51], which are known to influence the mechanical and electrical performance negatively.

The molecular beam epitaxy (MBE) method is the deposition of atoms or molecules directly on the substrate under ultra-high vacuum conditions. The method is relatively straightforward and widely used in industrial manufacturing semiconductor devices. In the MoS_2 case, ultrapure beams of Mo atoms and sulfur molecules are used. In order to produce a highly crystalline MoS_2 monolayer on hexagonal h-BN, the following procedure was used: using e-beam evaporators Mo and sulfur atoms were deposited on a h-BN substrate annealed at 700-900°C[52].

With respect to the scope of our study, let us introduce two relatively different procedures that were used for producing MoS_2 monolayers on Au(111) and graphene/Ir substrates: For obtaining the MoS_2 monolayer on the Au(111) substrate, the following was done: first, Mo atoms were deposited on the Au(111) surface in 10^{-6} mbar of H_2S at room temperature. Then keeping the H_2S atmosphere, the sample was annealed at about 870 K for 15 min[53]. The procedure can be modified to reach higher MoS_2 coverage[54]. The CVD method can also be used to manufacture wafer-scale samples of a MoS_2 monolayer on a Au substrate[55].

For obtaining the epitaxial MoS_2 monolayer on the graphene/Ir(111) substrate, a two-step process was used: firstly, Mo and sulfur ware evaporated on graphene/Ir(111), keeping the substrate at room temperature, then the sample was annealed at 750°C in the remaining sulfur flux. This represented one cycle of the synthesis. To keep MoS_2 oriented, only 0.4 monolayers can be obtained in one cycle; if more coverage is needed - more than one cycle should be performed[20, 56]. As one can see, the used parameters for different systems are different. This suggests that the exact procedure must be carefully adjusted for each particular case.

1.2.2 Electronic and spin properties

Most of the dichalcogenides-related research is done by optical studies. On the other hand, we are interested in investigating the electronic and spin structure of these materials to bring those two scientific fields together. Here we will skip most of the historical part and move directly to the studies we chose as benchmarks.

Let us start with the electronic bulk properties of MoS_2. An angle-resolved photoemission spectroscopy (ARPES) study shows that the top valence band of bulk MoS_2 is located at the $\overline{\Gamma}$ point in the Brillouin zone, while the valence band states in the region of the $\overline{K}$ point feature 0.5 eV higher binding energy than at the $\overline{\Gamma}$ point[57]. When the sample is K-doped (electron-doped), the bottom conduction band states that appear in ARPES spectra at the $\overline{K}$ point[57]. This is clear evidence that a bulk MoS_2 is an indirect semiconductor.

Time-resolved ARPES measurements of a MoS_2 single layer that was epitaxially grown on HOPG show that the top valence band and the bottom conduction band states are located at the $\overline{K}$ point[58]. As a benefit of time-resolved measurements, one can perform direct measurements of the quasi-particle bandgap and its dynamics without doping the sample. ARPES measurements of a MoS_2 monolayer on graphene/Ir[56] and Au(111)[59, 60] substrates confirm that the top valence band of the MoS_2 monolayer is located in the region of the $\overline{K}$ point for the given different substrates.

Interestingly, the MoS_2 monolayer valence band states are out-of-plane spin-split in the region of the $\overline{K}$ point, which was experimentally shown in the MoS_2/Au(111) system[60]. The bulk MoS_2 crystal also shows a valence band splitting in the region of the $\overline{K}$ point; however, those states are not spin polarised[61]. On the other hand, one must be careful in accounting for final state effects, as they can also result in a spin polarization in spin-resolved ARPES spectra[61, 62]

1.2.3 Optical properties

The main tools for investigating atomically thin transition metal dichalcogenides are optical methods[63]. The photoluminescence method aims to pump the band gap of a material with light to excite electrons into the conduction band, creating excitons. Excitons have a limited lifetime, and when they recombine, an electron falls back to the valence band, emitting a photon whose energy and polarisation are determined by the properties of the optical band gap. This photon is captured and analyzed. The photoluminescence peak sharpness correlates with the lifetime of the exited excitons. To our knowledge, the narrowest photoluminescence achieved for exfoliated MoS_2 monolayer is 2-5 meV[64]

MoS_2 bulk crystals feature an indirect band gap, while MoS_2 monolayers have a direct one. Due to the momentum conservation law, the MoS_2 monolayer should feature a photoluminescence signal, while multi-layered or bulk MoS_2 should not. Such behavior was experimentally demonstrated[1]: the luminescence quantum yield is exponentially decreasing from 10^{-2} for the monolayer to 10^{-6} for six layers of MoS_2.

As the dichalcogenides family features a particular spin orientation of the top valence and the bottom conduction bands, which are opposite for $\overline{\mathrm{K}}$ and $\overline{\mathrm{K}'}$ points in the Brillouin zone ($\overline{\mathrm{K}}$ and $\overline{\mathrm{K}'}$ valleys), one should expect optical properties related to optical selection rules. Indeed, the MoS_2 monolayer demonstrates valley-selective circular dichroism, which means that a particular valley can be selectively pumped using circularly polarised light[29]. This may lead to induced magnetization and a Hall effect without an applied external magnetic field[65].

We must remember that radiative exciton recombination is not the only option for excitons to annihilate. Another way is to sink to the substrate, which does not have a band bap, and let their energy dissipate non-radioactively through interactions with phonons. Photoluminescence quenching in the MoS_2/Au system was demonstrated in Ref.[66]. For this reason, and as in the current study, we were aiming to investigate the photoluminescence properties of our system; we shielded the MoS_2 monolayer from the Co thin film with graphene in between. On the other hand, graphene also does not have a band gap and may lead to photoluminescence quenching. However, the photoluminescence signal in MoS_2 monolayer on graphene/Ir substrate is still present[56].

1.2.4 External magnetic field and magnetic proximity

Let us consider the dichalcogenides family and monolayers in an external magnetic field. An external magnetic field breaks time-reversal symmetry and spin degeneracy, enabling us to exploit spin and valley degrees of freedom. The electronic states of a material should respond to an external magnetic field with a Zeeman shift. As an optical transition happens inside an electronic band gap – the optical band gap must change, too.

1. TRANSITIONAL METAL DICHALCOGENIDES AND MOS_2 MONOLAYER: STATE OF THE ART

In the case of dichalcogenides, a giant external magnetic field in the direction perpendicular to the monolayer plane results in a valley Zeeman effect, and diamagnetic excitons shift[67]. This means that optical gaps in $\overline{\mathrm{K}}$ and $\overline{\mathrm{K}'}$ valleys stop having the same energy: their energies start to depend linearly on an applied magnetic field. The magneto-reflectance studies demonstrated the value of the valley splitting to be 230 μ eV T^{-1} for both MoS_2 and WS_2 monolayers, the valley g-factors of excitons were estimated to be $\approx$-4. Photoluminescence studies demonstrated the ability to control the valley pseudospin and Zeeman effect in optical excitations in WSe_2 monolayer[11, 68].

Mentioned above studies used giant magnetic fields (up to 65 T); however, can one reach similar-magnitude effects using more negligible or even zero external magnetic fields? One may think about a heterostructure of dichalcogenide monolayer and a magnetic material. The magnetic material may have its magnetization or enhance an external one due to high magnetic susceptibility (χ). Then due to the close spacial proximity, a penetration of spin polarization from the magnetic material to the dichalcogenide monolayer may occur. This process is called the magnetic proximity effect[12].

The study[13] demonstrates a Fe-Doped MoS_2 monolayer, where the effect of an external magnetic field was $\approx$5 times enhanced. Relatively similar results were achieved in the Co-Doped MoS_2 monolayer[69]. First principal calculation studies suggest using Cr_2O_3, CrI_3, and LiBeNi(111) substrates for MoS_2 monolayer to realize impressive magnetic proximity effects that would be equivalent to external magnetic fields of 100 T, 89 T, and 58 T correspondingly[70–72].

Let us move to the consideration of an applied or enhanced via proximity effect in-plane magnetic fields. The in-plane magnetic field is the one parallel plane of the studied two-dimensional monolayer. In the discussion about out-of-plane magnetic fields, we considered the response of out-of-plane spin-polarized electronic states to the magnetic field, which was parallel or antiparallel to their spins. In the in-plane magnetic field case, the electronic states' spin-polarization and magnetic field directions are perpendiculars. The theoretical work[73] demonstrates that an in-plane magnetic field allows a spin-flip mechanism. Essentially this means that spin directions of electronic states can be tilted. Changing electronic states' spin directions modifies established optical-selection rules that open up previously forbidden optical transition possibilities. These freed optical transitions manifest them-self in the appearance of so-called dark excitons (see more in section 1.4.1).

Using *ab initio* calculations, several works controversially predicted various values of the dark exciton energy in MoS_2 monolayer[74–76]. On the other hand, the photoluminescence measurements of MoS_2 monolayer under an applied 30 T in-plane magnetic field demonstrated that the dark exciton energy is 14 meV lower than that of bright

excitons[15]. Manipulation of the optical selection rules can greatly influence dichalcogenides' optical properties, such as excitons lifetime, inter-valley scattering, and recombination.

1.3 Magnetism in solids

Let us start with a particular electron in the atom. It features a combined magnetic moment that consists of a spin (s) and atomic orbital angular momentum (l). An electron is a fermion; for two similar electrons, it is forbidden to coexist. That is why electrons repel each other. Such property is called the Pauli exclusion principle.

An electron angular momentum is defined by the electron's atomic orbital (or a band structure in a solid). Therefore, we must consider electrons in the context of their occupancy. Here we need to remember Hund rules[77]:
(1) consistency with the Pauli principle, a maximum total atomic spin ($S = \sum m_s$) must be obtained;
(2) remaining consistent to (1), a maximum angular momentum ($L = \sum m_l$) must be obtained;
(3) A total atomic angular momentum is defined as
$J = |L - S|$, when a corresponding shell is less than half full, and
$J = |L + S|$, when a corresponding shell is more than half full.
One can notice that states will be occupied with electrons with parallel spins as much as possible. These unbalanced total atomic spins correspond to mentioned earlier elementary magnetic moments inside materials.

Let us now address how electrons located in different atoms interact with each other and form a long-range spin alignment. Let us construct a wave function of two electrons (1) and (2), which are located relatively close to each other at the coordinates (a) and (b) (for simplicity in the neighbors' atoms). (r_1) and (r_2) are the coordinates of the (1) and (2) electrons. The wave functions of the individual electrons are $\Psi(r_1)$ and $\Psi(r_2)$ and the total wave function is $\Psi(r_1, r_2)$. $\Psi(r_1, r_2)$ must be antisymmetric; otherwise, wave functions of single electrons are identical, which contradicts to Pauli principle, while a solution $\Psi * \Psi$ must be the same in case of exchange of electrons.

Given $\Psi_a(r_1)$ and $\Psi_b(r_2)$ are wave functions of electrons (1) and (2) on corresponding (a) and (b) atoms:
$\Psi(r_1, r_2) = \Psi_a(r_1)\Psi_b(r_2)$ and $\Psi(r_1, r_2) = \Psi_b(r_1)\Psi_a(r_2)$ both cannot be solutions as an inter replacement of electrons alters $\Psi * \Psi$.
$\Psi(r_1, r_2) = \Psi_a(r_1)\Psi_b(r_2) + \Psi_b(r_1)\Psi_a(r_2)$ also cannot be a solution, as it is symmetric. Therefore it must be

$$\Psi(r_1, r_2) = \Psi_a(r_1)\Psi_b(r_2) - \Psi_b(r_1)\Psi_a(r_2),$$

which is antisymmetric.

The Hamiltonian ($\langle H \rangle$) can be presented as a sum of separate Hamiltonians: ($\langle H_1 \rangle$) and ($\langle H_2 \rangle$) for electrons (1) and (2), and ($\langle H_{1,2} \rangle$) for interaction Hamiltonian.

Solving $E = \iint \Psi^* \langle H \rangle \Psi d\tau_1 d\tau_2$, one can obtain:

$$E_{tot} = E_1 + E_2 + E_{coulomb} + E_{exchange},$$

where E_1 and E_2 represent energies that only depend on the electron (1) on atom (a) and electron (2) on atom (b); $E_{coulomb}$ represent a classic Coulomb interaction; and $E_{exchange}$ is called the exchange energy (to symbol J can be used instead).

$$E_{coulomb} = \iint \{\Psi_a^*(r_1)\Psi_b^*(r_2)\} \langle H_{1,2} \rangle \{\Psi_a^*(r_2)\Psi_b^*(r_1)\} d\tau_1 d\tau_2$$

Let us now include spin. Given spin wave functions are $\varphi_1(s)$ and $\varphi_2(s)$, and $\varphi(s_1, s_2)$ is a linear combination.

$$\Psi_{tot} = \Psi(r_1, r_2)\varphi(s_1, s_2)$$

As Ψ_{tot} must be antisymmetric, if $\Psi(r_1, r_2)$ is antisymmetric, then $\varphi(s_1, s_2)$ must be symmetric and vice versa. Symmetric $\varphi(s)$ corresponds to parallel spins and a ferromagnetic ordering ($J/E_{exchange}$ is positive). Antisymmetric $\varphi(s)$ corresponds to antiparallel and antiferromagnetic ordering ($J/E_{exchange}$ is negative).

1.3.1 Exchange mechanisms

Heisenberg model of ferromagnetism Let us introduce a direct exchange interaction and answer the question of how the interaction between two neighboring electronic sites with overlapping wave functions can lead to a long-range magnetic order.

Heisenberg included electron spins into overlapping wave functions of two electrons and assumed a total wave function to be a linear combination of orbital wave functions[78]. The Heisenberg interaction energy is given in the form of

$$E_{Heis} = -2JS_1S_2,$$

where J>0 corresponds to ferromagnetism and J<0 to antiferromagnetism.

For a solid, we need to consider not just two electrons but all of them. We can boldly assume that all the single interaction energies are equal ($J_{i,j} = J$), and we should only count neighboring cites.

$$\langle H \rangle = -2 \sum \sum J_{i,j} \; s_i \cdot s_j = -2J \sum \sum_{nearest} s_i \cdot s_j$$

Heisenberg's model is simple and valuable but inaccurate for the number of cases. Slater and Bethe showed that this interaction vastly depends on the distance between

electronic and atomic cites and can even change from ferromagnetism to antiferromagnetism. Bethe-Slater curve demonstrates that. As the next step, Heusler demonstrated that alloys formed from elements that are not ferromagnetic could feature ferromagnetism (Heusler alloys). It suggested that magnetic properties are rather determined by electron structure than the properties of the atoms.

Localized and itinerant electronic theories When considering exchange interactions between electrons, we may think about two scenarios: electrons are localized in the atomic sites, and electrons are not localized (itinerant) but instead participate in a collective band structure. These approaches are mutually exclusive. However, none of the actual materials can be fully described by only one of them. As a rule of thumb, the localized approach works well with rather localized rare earth metals (magnetic moments are in localized f orbitals). In contrast, the itinerant approach works better with 3 d transition metals and alloys with similar band structure properties.

Superexchange Let us think about how a magnetic exchange mechanism can exist in case of wave functions of considered electrons do not overlap. It is called the superexchange mechanism$_3$. A simple Heisenberg model is irrelevant in this case, as magnetically relevant electrons can couple with each other through coupling with magnetically irrelevant electrons. The superexchange mechanism is relevant for the present study as in the MoS_2/graphene/Co system, a magnetization penetration from ferromagnetic Co film though diamagnetic graphene to paramagnetic (or extremely weakly ferromagnetic) MoS_2 monolayer.

Indirect exchange Another way to couple unpaired magnetic electrons is through conduction electrons (conduction band). **R**uderman and **K**ittel[79], **K**asuya[80], and **Y**osida[81] subsequently used it for explaining exchange interactions. Therefore, it is now known as **RKKY** theory. We should keep in mind this concept, as we believe that in the system MoS_2/graphene/Co, the magnetic exchange between Co and MoS_2 takes place through graphene electronic bands.

1.3.2 Magnetic proximity

We use an external magnetic field to enhance magnetization in paramagnetic materials and orient magnetic domains in ferromagnetic or antiferromagnetic materials. However, generating a strong external magnetic field is not only demanding but also not downscalable. On the other hand, one can bring magnetic material with an established long-term magnetic order in close proximity to the subject of interest. This may lead to penetration of spin polarization from the magnetic material to the subject of interest.

In the current study, we used Co thin film as a ferromagnetic material which induced spin polarization to MoS_2 monolayer.

Back in 1969, J. Hauser experimentally estimated the spin polarization penetration depth of magnetic metals (e.g., Fe, Ni, Cr) into nonmagnetic metallic Pd and $Ni_{0.58}Rh_{0.42}$ alloy[12]. The range of polarization penetration dept was around 20±10Å. Nowadays, magnetic proximity is considered a manipulation tool for spintronics[82], superconductors[83, 84], and topological materials[85]. Due to its spatial localization and efficiency, the magnetic proximity effect is interesting for two-dimensional heterostructures[86].

Considering the mentioned above Superexchange and indirect exchange concepts, one can imagine how magnetic proximity may occur on the interfaces with magnetic materials. Several first-principle calculations studies suggest giant valley splitting of dichalcogenides via magnetic proximity effect: defected WS_2 with adsorbed Mn atoms is expected to feature up to 210 meV valley splitting[87], while $MoTe_2$ monolayer on magnetic EuO substrate with 300 meV[88]. Experimental demonstrate slightly less impressive but still convincing results: Resonant optical reflection spectroscopy of $MoSe_2$ monolayer on ferromagnetic $CrBr_3$ demonstrates 2.9 meV valley splitting, which is claimed to be equivalent to 12 T of an external magnetic field[89] in the presence of a zero external magnetic field. On the other hand, the magnetic proximity effect can enhance an external magnetic field. Magneto-reflectance spectra of WS_2 on EuS substrate demonstrate 16 meV/T valley splitting as if an external magnetic field was enhanced by two orders of magnitude. Similarly, Fe atoms doped MoS_2 monolayer demonstrate approximately 5- fold enhancement of an external magnetic field via photoluminescence measurements[13].

Magnetic properties of MoS_2 monolayer A bulk MoS_2 is a paramagnetic material; however, when one reduces the number of layers and approaches a monolayer MoS_2 – it becomes a weak ferromagnetic[90, 91]. Recent publications suggest that mentioned ferromagnetism originated from linear domain boundaries.

1.4 Optical excitations in MoS_2

MoS_2 is a mainly exciting material in the framework of optical properties. In this part, we will connect the current spectroscopic study to the much more advanced and broad optical studies of dichalcogenides.

1.4.1 Excitons

From the photoemission spectroscopy point of view, we are mainly interested in solids' electronic state structure: it tells us about occupied electronic states, while DFT or tight-binding approximation calculations describe both occupied and unoccupied electronic states.

The spectroscopic language is based on electrons and electronic states, as direct experimental evidence represents electrons that were excited from a solid. On the contrary, optical studies language is based on solid properties and quasi-particles that somehow interact with light. The primary representative of such quasi-particles is exciton. Exciton is a combined state of an electron and a hole bonded by electrostatic force.

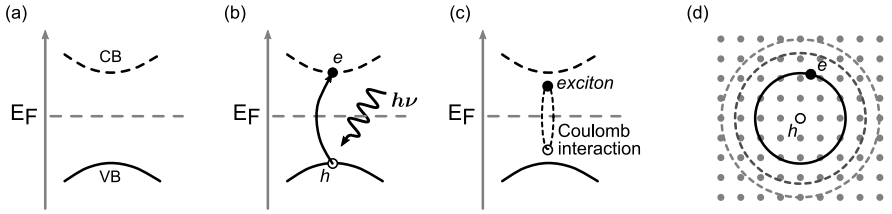

Figure 1.2: Schematic representation: (a) of two states in a semiconductor: valence and conduction band respectively; (b) excitation of an electron from the valence to conduction band leaving an electron hole in the valence band; (c) formed due to Coulomb interaction electron-hole pair – so-called exciton. The dotted line represents the state which is not occupied. (d) exciton in a real space.

Excitons inside electronic states band gap

One can see a schematic representation of two electronic states in Fig. 1.2(a): one state is above the Fermi level (E_F) in the conduction band, and another is below in the valence band. Let us consider that an electron absorbs a photon and gets excited from valence to a conduction band (see Fig. 1.2(b)). This process gives rise to an electron-free state in the valence band; this state is called an electron-hole or just a hole. A hole is a collective electron state that can be considered an electron-like positively charged particle with its effective mass. An electron and a hole can get attracted to each other due to the electrostatic force (Coulomb interaction) and form a combined state (electron-hole pair) called exciton that energetically exists inside an electronic state band gap (see Fig. 1.2(c)). Worth noticing that the optical band gap is determined by the light absorption followed by exciton formation and can be different from the electronic states band gap.

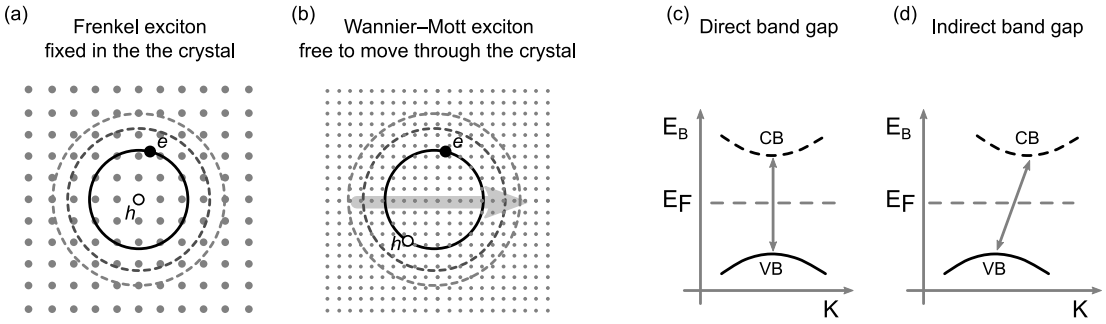

Figure 1.3: (a) and (b) a schematic representation of two types of excitons: fixed in the crystal and free to move through it. Dotted lines represent possible electron orbits given exciton n=2 and n=3. Small grey cycles represent a crystal structure. (c) and (d) schematic representations of direct and indirect band gaps.

Excitons in a real space

An electron-hole pair in a solid is somewhat similar to electron-proton pair in the hydrogen atom. Indeed, exciton features hydrogen atom-like states: there is a ground state with n=1 and exited states with n=2,3, and so on. In Fig. 1.2(d), one can see a schematic exciton representation in real space: the solid line represents a ground exciton state, and dotted lines - represent excited states.

Yakov Frenkel proposed the concept of exciton in 1931 [92]. Fig. 1.3(a) represents a Frenkel type of exciton, where the hole is localized at a particular position in the crystal. However, in general, an electron-hole pair (exciton) can feature some mobility and be free to move through the crystal – see Fig. 1.3(b) that represents the Wannier–Mott type of excitons.

Direct and indirect band gap

Electron-hole pair bonded by electrostatic force does not have to follow optical selection rules. Let us consider two types of band gaps: direct and indirect (see Fig. 1.3(c),(d)). The band gap in semiconductors is determined by the maximal-energy state in the valence band and the minimal-energy state in the conduction band. Each state is characterized by a certain k-vector in the Brillouin zone. If both states feature the same k-vector – the gap is direct(Fig. 1.3(c)); if not – the gap is indirect(Fig. 1.3(d)).

Let us consider a qualitative difference between direct and indirect band gaps in a semiconductor. Suppose we introduce a photon and try to excite an electron from the valence to the conduction band. In that case, we will succeed in the case of a direct band gap and not in the case of indirect due to the electron-photon momentum conservation principle. In this respect, some excitons can be created by a single photon act (and therefore can recombine, emitting a single photon), and some are not.

Bright and dark excitons

An exciton is bright if it can be created in a single-photon absorption process under normal incidence. The bright exciton can also recombine, generating a single photon. In the case of a dark exciton, the corresponding electron and hole are not coupled by optical selection rules. The angular momentum conservation is not the only constraint: one must consider an electron and a hole states symmetries and spins. It is worth noticing that dark excitons are still present in solids, as the not-single-photon act can create them, such as photon-induced electron excitation followed by phonon relaxation or any multiple-steps process.

1.4.2 Direct and indirect band gap in MoS_2

MoS_2 belongs to the group VI transition metal dichalcogenides (TMD) family that includes MoS_2, MoS_2, WS_2, and WSe_2. All bulk dichalcogenides are indirect semiconductors that are van der Waals materials constructed by three-atoms-think layers (e.g., S-Mo-S). Any multilayer van der Waals materials can be imagined as a stack of mono layers that are spatially separated and weakly interact with each other. Nevertheless, this weak interaction makes a huge difference: bulk materials can be indirect, while monolayers direct semiconductors.

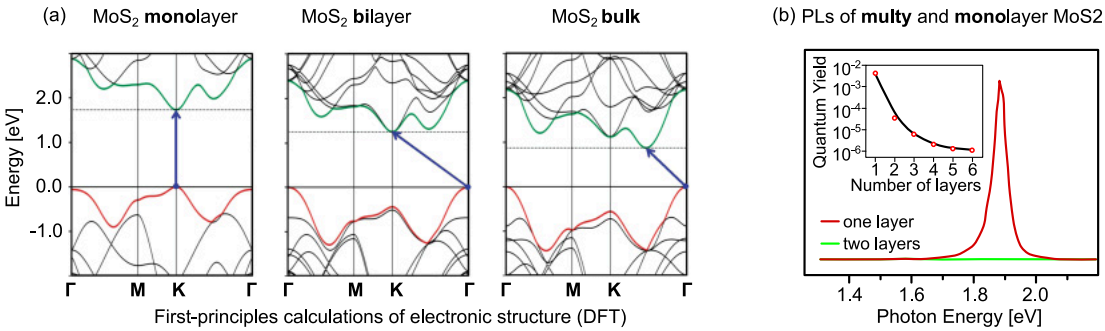

Figure 1.4: (a) DFT representations of monolayer, bilayer, and bulk MoS_2 electronic structures (obtained from [93]): MoS_2 is a direct band gap semiconductor for monolayer and indirect for multilayer. (c) PL intensity measurements of MoS_2 multi and monolayer (obtained from [1]).

In Fig. 1.4(a), one can see the optically related difference in MoS_2 electronic structure in monolayer, bilayer, and multilayer (bulk). In monolayer MoS_2 maximal-energy states in the valence and minimal-energy states in the conduction band are located in $\overline{\mathrm{K}}$ and in $\overline{\mathrm{K}'}$ points in the Brillouin zone. Starting from the bilayer systems, the maximal-energy states in the valence band are located at $\overline{\Gamma}$ point, and this can be easily identified via photoemission spectroscopy.

In order to illustrate the qualitative difference in optical properties that correspond to such a change in electronic structure, we refer to the PL experiment presented in

Fig. 1.4(c) (adopted from [1]). One can see that PL from MoS_2 bilayer is several orders of magnitude less intensive than from MoS_2 monolayer. PL from MoS_2 three layers is an order of magnitude less intensive than from MoS_2 bilayer, and so on. That happens due to the MoS_2 transformation from a direct to an indirect semiconductor.

Another schematic MoS_2 monolayer electronic states representation is shown in Fig. 1.5(a): it was obtained by tight binding approximation calculations. One can see that both valence and conduction bands consist of a mixture of p and d atomic orbitals; in particular, in the region of $\overline{\mathrm{K}}$ point, the spin-orbit interaction causes a significant splitting in valence band states. We can presume that the crystal symmetry properties, orbital character, and spin structure will play a crucial role in optical transition properties.

1.4.3 Optical selection rules in MoS_2 monolayer

Let us now consider optically active regions of $\overline{\mathrm{K}}$ and $\overline{\mathrm{K}'}$ points in valence and conduction bands. Using Fig. 1.5(b) as a mind map, let us consider the possibilities of exciting an electron from the valence to the conduction band.

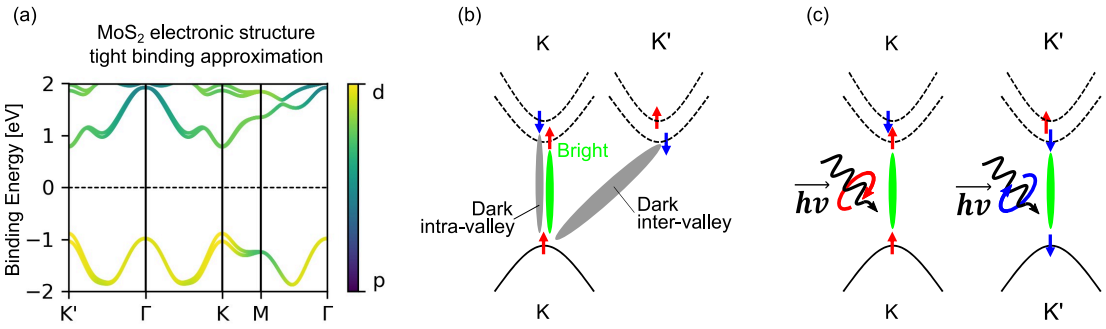

Figure 1.5: (a) Representation of tight binding approximation calculations of MoS_2 monolayer electronic states. A color scheme represents a mixture of p and d orbitals in MoS_2 valence and conduction bands. (b) A schematic representation of bright and dark excitons in MoS_2. For simplicity only $\overline{\mathrm{K}}$ to $\overline{\mathrm{K}}$ and $\overline{\mathrm{K}}$ to $\overline{\mathrm{K}'}$ points transitions are shown. (c) A schematic representation of chirality of interband transitions at $\overline{\mathrm{K}}$ or $\overline{\mathrm{K}'}$ points relater to σ^+ and σ^- circularly polarized light.

Conservation of energy, momentum, and spin

As a corresponding to such a band gap photon would have a little momentum compared to an electron in the region of $\overline{\mathrm{K}}$ point, the photoexcitation can only take place in the same $\overline{\mathrm{K}}$ or $\overline{\mathrm{K}'}$ valley. Exciton that do not follow this rule are so-called **dark inter-valley exciton** (see Fig. 1.5(b)).

Due to spin-orbit interaction in the regions of $\overline{\mathrm{K}}$ and $\overline{\mathrm{K}'}$ points, valence and conduction bands are spin-split. Both maximal-energy states in the valence band and

minimal-energy states in the conduction band are spin polarised; this polarisation is opposite in $\overline{\mathrm{K}}$ and $\overline{\mathrm{K}'}$ points (see Fig. 1.5(c)). The optical excitation can only take place in the state with a same spin, which is counter-intuitive, as the photon quantum number S=1. Important to mention that in structures like GaAs, optical transitions happen between states with opposite spins, which is more intuitive. The reason for such difference is that we must consider J quantum number that include both S and L quantum numbers, which is quite complex for electronic states that $\overline{\mathrm{K}}$ or $\overline{\mathrm{K}'}$ points that consist of mixture of p and d orbitals in C_{3h} point group symmetry.

Chirality

Due to similar symmetry reasons, interband transitions at $\overline{\mathrm{K}}$ or $\overline{\mathrm{K}'}$ points are chiral: the circularly polarized light σ^+ (σ^-) can only couple to the transition at $\overline{\mathrm{K}}$ ($\overline{\mathrm{K}'}$) points[29, 94], as it is shown in Fig. 1.5(c).

Spin-valley locking

Here it is important to emphasize that an excited electron cannot change the valley, as it would require electron to flip spin or undergo an energetically unfavorable transition. In this respect, excited electrons and holes maintain their spins and valleys, and such a feature is so-called spin-valley locking. This property is of particular interest, as by a light polarization, one can control which valley to pump and electrons with which spin to excite to the conduction band.

Given that recombination processes might take a while and electrons may maintain an excited state in the conduction band for a long time, one can use MoS_2 and its family in applications of valleytronics, spin-optics, and spin-filters.

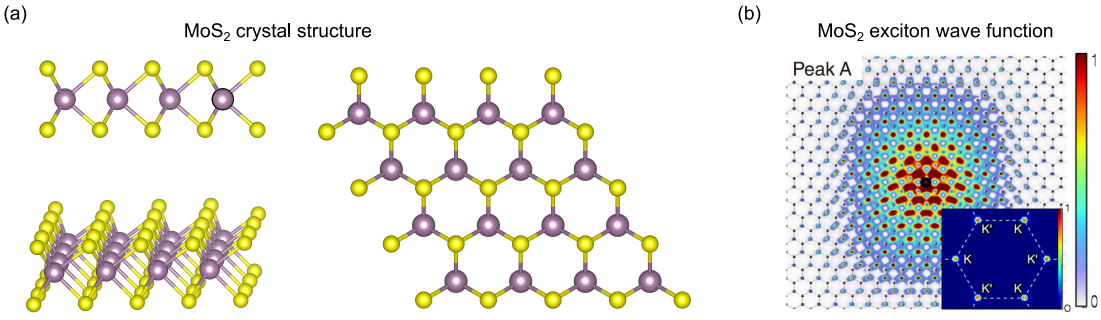

Figure 1.6: (a) MoS_2 monolayer 3D crystal structure presented under different angles (geometrical perspectives). (b) A typical wave function of exciton calculated for MoS_2 monolayer (obtained from [95]): A color scheme represents electron wave function modulus squared. The inset represents the same in momentum space.

Bright and dark excitons in MoS_2

In the MoS_2 monolayer, bright excitons consist of electrons and holes that share the same valley and spin direction. In contrast, dark ones consist of electrons and holes from different valleys and feature opposite spin directions (see Fig. 1.5(b)).

A time-reverse process of bright exciton formation brings us to the recombination process followed by a single photon-emitting act. The formation of dark excitons can be complex. One way to produce a dark exciton is for a bright exciton to experience various scattering events with electrons, holes, phonons, other excitons, or defects. Such scattering may induce considerable exciton momentum or energy changes or lead to spin flips. Another way would be a few-step generation process, such as electrical injection or non-resonant optical excitation followed by non-radiative relaxation processes. A dark exciton can also be formed when optically or electrically injected an electron and a hole merge. Dark excitons may feature completely different properties than the bright ones, such as total angular momentum may not be equal to one, or they can have a large center-of-mass momentum.

As bright excitons can annihilate in a single photon act, they are much easier observed in optical studies, such as photoluminescence or optical absorption. On the contrary, dark excitons interact with light in many-step processes and often cannot be directly observed in optical experiments. However, they still play an essential role in the dynamic properties of the system.

Excitons in real space

In order to imagine an exciton, one can take a look at Fig. 1.6(b): in the publication[95], the authors calculated and illustrated a typical MoS_2 monolayer exciton wave function in a real space. The Bohr radius of excitons in a MoS_2 monolayer is around a few nanometers, which means that electron and hole correlation extends for several lattice periods. These excitons can also move through the crystal. Therefore, these excitons have intermediate nature between the Wannier-Mott and large-radius-type [63].

Mathematical descriptions of excitons in MoS_2

Let us mathematically formulate electron and hole quasi-particle states that form an exciton inside a band gap[63]. An electron excitation from a valence band to an empty conduction band creates an empty electron state in the valence band. Such a many-body system can be described by the two-particle approach: the interaction of negatively charged conduction band electron and positively charged valence band hole

One can derive the hole Bloch function $|h\rangle = |s_h, \tau_h, \boldsymbol{k}_h\rangle$ from the empty valence band electron state Bloch function $|v\rangle = |s_v, \tau_v, \boldsymbol{k}_v\rangle$ applying the time-reversal operator

$|h\rangle = \hat{\mathcal{K}}|v\rangle$[96]. Where s_ν ($\nu = c, v$) is the spin index, $\tau_\nu = \pm 1$ is the valley index, and k_ν is the wave vector for valence (v) or conduction (c) bands.

The hole wave vector must be opposite to the one of the empty electron state: $\boldsymbol{k}_h = -\boldsymbol{k}_v$ because the time reversal operator flips the spin and changes the wave function orbital part to its complex conjugate. Moreover, the hole valley and spin quantum numbers must be opposite to the empty-electron-state: $s_h = -s_v$, $\tau_h = -\tau_v$. Such transformation can describe how a photon with a particular polarization excites and forms an electron-hole pair.

Now let us consider an optical transition in MoS_2 monolayer. σ^+ photon (that features an in-plane wavevector projection $\boldsymbol{q}_\parallel$) places an electron with a wavevector $\boldsymbol{k}_e$ into $\tau_e = +1$ ($\overline{\mathrm{K}}$) valley with the $s_e = +1/2$ state. Meanwhile, the valence band state with wavevector $\boldsymbol{k}_v = \boldsymbol{k}_e - \boldsymbol{q}_\parallel$ becomes unoccupied. Given the above, one can derive the corresponding hole wavevector to be $\boldsymbol{k}_h = -\boldsymbol{k}_v = \boldsymbol{q}_\parallel - \boldsymbol{k}_e$. As expected from the momentum conservation principle, an electron-hole center of mass wavevector is $\boldsymbol{K}_{\mathrm{exc}} = \boldsymbol{k}_e + \boldsymbol{k}_h = \boldsymbol{q}_\parallel$. In this respect, the hole spin $s_h = -1/2$ and valley index $\tau_h = -1$ formally are opposite to those of the conduction-band electron. Similar σ^- photon results in creating the electron-hole pair with $\tau_e = -\tau_h = -1$, $s_e = -s_h = -1/2$[23, 97].

As a result, excitonic states with $\tau_e = -\tau_h = +1$, $s_e = -s_h = +1/2$ are active (bright) in σ^+ polarization and the states with $\tau_e = -\tau_h = -1$, $s_e = -s_h = -1/2$ are active (bright) in σ^- polarization. The exciton states with $\tau_e = \tau_h$ (occupied electron states in the conduction band and unoccupied electron states in the valence band) or $s_e = s_h$ (electron and unoccupied electronic state have opposite spins) are dark (not optically active). The visual representation of mentioned transitions is shown in Fig. 1.5(b)(c).

1.5 Spin properties and spin-polarization related to experiments

1.5.1 Spin polarisation

This section aims to avoid confusions that can happen in the discussion about spin-related properties. In the manuscript we use such terms as "spin polarisation", "spin component", "in-plane", "out-of-plane", and so on. In order to avoid long repetitive words sequence, such as "The spin component of the state in the direction that is parallel to the 2D surface of MoS_2 monolayer and lies along Co easy axis of magnetization provided by the analysis of spin-polarised electron beam produced by photoemission process and propagating in a particular angular direction...", we use a simple "in-plane spin polarisation" term. This section is about terminology and understanding.

Spin is an intrinsic form of angular momentum in quantum mechanics carried by elementary particles.

Spin direction

Thinking about a spin of an electron, we imagine a small magnetic dipole. The magnetic dipole is a vector with a direction. Can we think about the spin direction in this respect? Thinking about the direction in mathematical terms, we need to imagine a coordinate system, and any system can be applied. To make it simple, let's consider the XYZ system of real space. A vector can be projected on any given axis. The scalar value of this projection is called a **scalar projection** or a vector component. A vector direction can be described by its vector components. Similarly, we can describe a spin direction by its **spin components** along particular directions.

In quantum mechanics, the spin direction can be described by spin components along relative excises. Unlike classical physics, quantum mechanics features discrete values. The spin projection quantum number (spin component) can only have discrete values: $S_i = \hbar s_i$, where $s_i \in \{-s, -s+1, ...s-1, s\}$. As an example that we need, the spin projection of an electron along the z-axis can be only $+1/2$ and -1/2.

Spin polarisation of the state

A statistical distribution of electrons with different spin directions (spin projections or components) is so-called spin polarisation. Spin polarization can be explained as a degree to which the spin of elementary particles is aligned with a given direction.

Imagine a peak of intensity in a particular region of energy-momentum space in photoemission measurements. Now let us check how this intensity will be distributed if we split it by spin in a given direction. [For ease of imagination, let us imagine a huge magnetic field at the end of the photoemission experiment like in Stern–Gerlach experiment]. Out of imaginary 10.000 electrons, 5.000 will go to one detector and 5.000 to another: it is 50% distribution. That would mean that the state is not spin polarised, or spin polarisation is 0%. If out of imaginary 10.000 electrons, all 10.000 will go to one detector and 0 to another: it is 100% distribution. That would mean that the state is fully or 100% spin polarised. Mixed scenarios are usually observed.

Spin polarisation of the state, electron beam, and spectra

In experiments, we don't deal with particular states but rather with electron beams that were excited from samples and propagated in a particular direction (angle) with a particular speed (energy). We can extract some spin polarisation quantitative properties of the electron beam. However, electrons of this beam do not have to be excited from a particular state. Different states can be excited to experimentally indistinguishable electron beams due to multiple reasons: states that don't spatially overlap, moire structures that produce ripple effects, and states that can coexist in the same energy-momentum space due to symmetry properties, a background of photoemission process

(see section 2.1), and so on. Therefore, spin polarisation of a spectrum is a spin polarisation of a beam and can include spin polarisation of multiple electronic states and a background.

1.5.2 Example of out-of-plane polarisation in MoS_2

Here we discuss how a 100% out-of-plane polarised state can appear completely unpolarized (0%) in spin-resolved photoemission spectra of MoS_2/graphene/Co system.

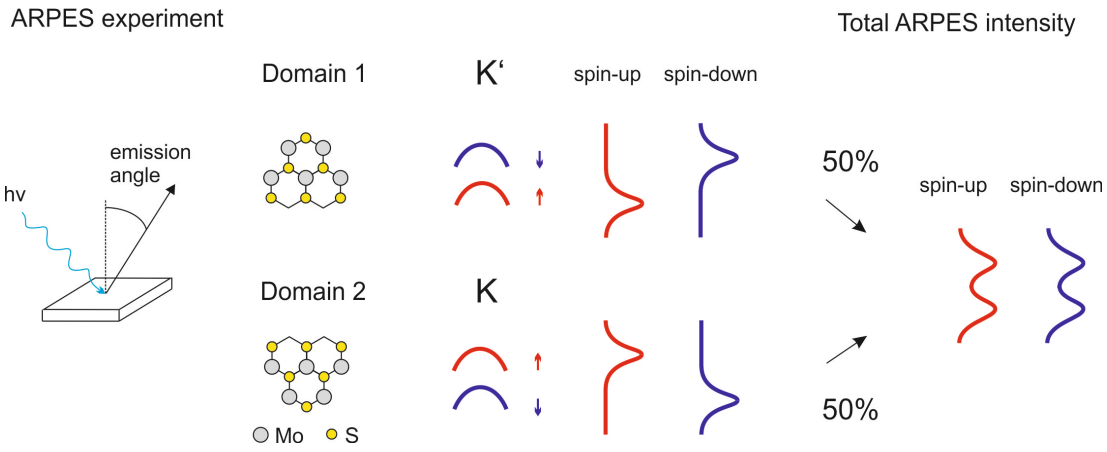

Figure 1.7: Illustration of the spin-resolved photoemission process from mirror MoS_2 domains and how it integrates to the measured spectra. In ARPES measurements, the same emission angle corresponds to the $\overline{\mathrm{K}}$ and the $\overline{\mathrm{K}'}$ points for mirror domains. Spin-up spectrum in the $\overline{\mathrm{K}}$ point is identical to the spin-down spectrum in the $\overline{\mathrm{K}'}$ point and vice versa.

As it was mentioned in section 3.4.2, MoS_2 coverage on graphene/Co substrate features coexisting mirror domains. PED data demonstrated that the amount of mirror domains of each kind is equal (see Fig. 3.13).

Let us consider a free-standing MoS_2 monolayer. At the $\overline{\mathrm{K}}$ point in the valence band, the states are spin-split and polarized in the out-of-plane direction. This implied that at the $\overline{\mathrm{K}}$ point in the valence band, a spin polarisation of MoS_2 states is 100% for each: the state with higher and lower binding energies. These spin polarizations are of an opposite sign.

To be more precise, at the $\overline{\mathrm{K}}$ point, let us define a state with higher binding energy, it is 100% spin-up out-of-plane spin polarised, and a state with lower binding energy is 100% spin-down out-of-plane spin polarised. At the $\overline{\mathrm{K}'}$ point, the situation is the opposite: a state with higher binding energy is spin-down spin polarised, and a state with lower binding energy is spin-up spin polarised.

How $\overline{\mathrm{K}}$ and $\overline{\mathrm{K}'}$ points can be distinguished in the experiment? In ARPES measurements $\overline{\mathrm{K}}$ and $\overline{\mathrm{K}'}$ points would mean excited electron beams moving with opposite

momentum. Now let us consider not a single MoS_2 monolayer but two coexisting mirror domains. In ARPES measurements, a particular emission angle for $\overline{\mathrm{K}}$ point of one domain would also be the one for $\overline{\mathrm{K}'}$ point of a mirror domain. Therefore, in the case of two mirror domains coexisting in the area of photoemission experiment space resolution, a signal from $\overline{\mathrm{K}}$ point of one domain would be a mixture with a signal from $\overline{\mathrm{K}'}$ point of a mirror domain. And we will not be able to distinguish those signals.

Now let us imagine a 100% spin polarised signal from $\overline{\mathrm{K}}$ point of one domain mixing with a 100% spin polarised signal from $\overline{\mathrm{K}'}$ point of a mirror domain. As those signals are oppositely spin polarised, the linear combination will result in 50% of each and lead to zero-polarisation of an end spectrum. We summarised this explanation of the spin-resolved photoemission process from mirror MoS_2 domains in cartoon Figure 1.7.

Summary: where we stand

MoS_2 monolayer is a chemically and mechanically robust direct band two-dimensional semiconductor. It can be combined with another two-dimensional material, such as another member of the dichalcogenides family that feature different values band gap, as well as with zero-gap semiconducting graphene and insulating h-BN. Comparing to silicon derivatives, MoS_2 benefits with a new dimension of complexity and possible application scenarios in terms of spin-valley physics.

In the following manuscript, we aim to add some knowledge in the direction of MoS_2 electronic- and spin- structure control. In particular, we are investigating the means of MoS_2 electronic and spin structure modifications via interaction with a substrate. We start with Au(111) substrate, which introduces Rashba spin-orbit interaction to MoS_2 monolayer due to high atomic number Au atoms and corresponding high potential gradient on the Au(111) surface. As a next step, we wish not only to modify but also to control the MoS_2 spin structure. The magnetic proximity effect may provide it, as by controlling the magnetization of the substrate, one can control the spin properties of MoS_2. We used graphene/Co substrate, where Co thin film shares its magnetization (electronic states spin polarisation) with a neighboring MoS_2 monolayer. Graphene is supposed to shield potential excitons from sinking into Co substrate and recombine in a non-radiative way (quenching). It is important for any following optical use.

External magnetic fields are able to greatly influence the optical properties of dichalcogenides. In the case of the out-of-plane magnetic field, it leads to spin-valley energy splitting, while in the case of the in-plane magnetic field, it leads to the brightening of a dark exciton. Replacing an external magnetic field with the magnetic proximity effect coming from graphene/Co substrate, we aimed to explore possibilities of modifying MoS_2 monolayer optical properties.

Chapter 2

Methods

This section introduces basic concepts and precise details of our measurements and computational methods. A general understanding of the physical process behind them is essential to avoid producing incomplete or corrupted data and the following data missinterpretation. Transparent demonstration of the crucial technical details makes experimental results trustworthy and reproducible. It also might help to catch the physics behind different effects from seemingly similar experiments.

2.1 Photoemission Spectroscopy

Photoemission Spectroscopy (PES) is the central method for the scientific exploration of the presented study. Therefore, we will describe it in much more detail than the other experimental and computational techniques.

2.1.1 Basic principles of Photoemission Spectroscopy

Photoemission spectroscopy is based on the photoelectric effect that was first experimentally observed by Hertz in 1887[98] and theoretically explained by Einstein in 1905[99]. A single electron can absorb a single photon and its energy. With this additional energy, the electron can escape an atom's potential well (barrier). In physical terms, a photon wavelength (λ) equals $2\pi c/\omega$, where is ω the angular frequency and c is the speed of light. The photon energy equals $\hbar\omega$ or $h\nu$, where ν is a frequency.

Einstein's theory of the photoelectric effect demonstrates how single photon can ionize an atom. The atom can be a part of any phase of matter; here, we focus solely on solid-state materials. Given the energy conservation law, let us write the equation:

$$\hbar\omega = |E_B| + \varphi + E_{kin}, \tag{2.1}$$

where $\hbar\omega$ is photon energy, E_B is an electron binding energy, E_{kin} is the kinetic energy of the electron after the escape, and φ is the work function of the material. φ is a

surface potential barrier that can be defined as the minimum energy required to remove an electron from the interior of the solid[100]. Using the equation, one can determine the electron binding energy by measuring the kinetic energy of the escaped electron and knowing the light wavelength. Indeed, for the experiment, one must use monochromatic light. The first experiment was performed in 1907 by Innes, who used an electromagnet to separate and measure electrons with different energies. He used an electromagnet and a photographic plate[101].

The photoemission process can be described by the three-step-model[102, 103]: First, an electron absorbs a photon and uses this energy to jump into a bulk final state; second, it travels to the surface of the solid; third, it overcomes a surface potential barrier and continues its path through a vacuum till an electron detector captures it.

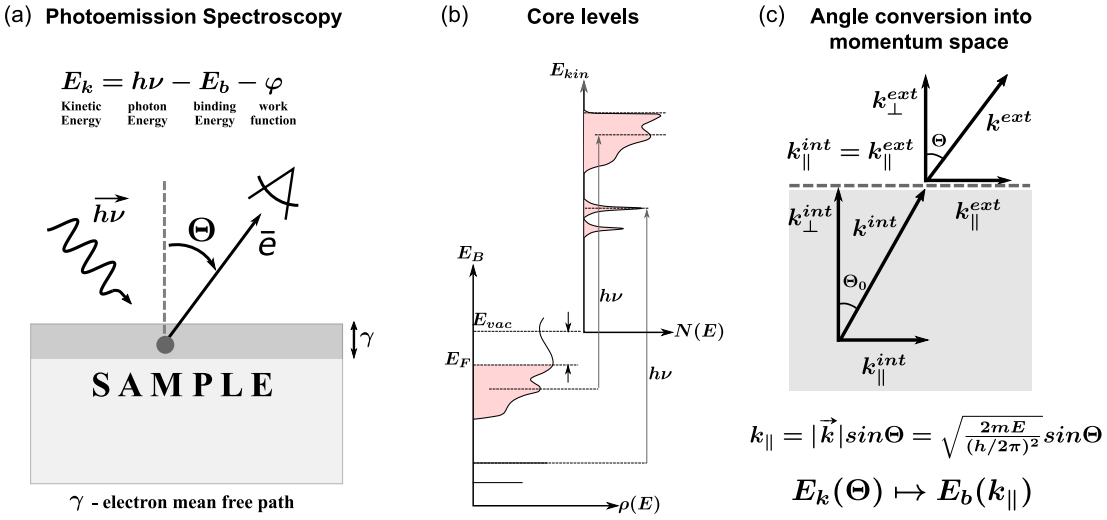

Figure 2.1: PES principals schematic representations of (a) a photoemission experiment; (b) the energy conservation low and a transfer of electrons from core levels to above vacuum level; (c) the momentum law for the electrons overcoming the surface potential barrier.

The first step is crucial as it explains the variety of final states effects in photoemission studies. The second step suggests that electrons can experience scattering while traveling: the more travel distance, the more scattering possibility. This possibility can be expressed as follows[102, 104]:

$$P(z) \propto e^{-\frac{z}{\lambda(E)}},$$

where z is the excitation depth and $\lambda(E)$ is an inelastic mean free path, which depends on the electron kinetic energy[105, 106]. The function of the mean free path (λ) relative to electron kinetic energy (E) represents a checkmark shape with a minimum of 50-100 eV electron kinetic energy. In order to use photoemission spectroscopy as a surface-sensitive technique, one should rely on the corresponding photon energies.

During the third step, the electron overcomes the surface potential barrier, which has its gradient perpendicular to the sample surface. Let us now consider the momentum conservation principle. Relative to the electron, the momentum of a photon is negligible. Therefore, the momentum of the electron is preserved. However, when the electron overcomes the surface potential barrier, it does not only lose some of the kinetic energy but also loses some perpendicular to the sample surface momentum. The parallel to the sample surface component of electron momentum is preserved. Let us define $\vec{K}$ as a photoelectron momentum, $\vec{k}$ as an electron momentum inside the solid, and ϑ as an emission angle. The photoelectron momentum can be determined through its kinetic energy and *vice versa*:

$$E_{kin} = \frac{\hbar^2 K^2}{2m}, \quad \left|\vec{K}_{\parallel}\right| = \left|\vec{K}\right| \sin\vartheta \tag{2.2}$$

$$\left|\vec{k}_{\parallel}\right| = \left|\vec{K}_{\parallel}\right| = \sqrt{\frac{2mE_{kin}}{\hbar^2}} \sin\vartheta \tag{2.3}$$

Using equations 2.1 and 2.3, one can determine electrons' binding energies and parallel momentum values from a photoemission experiment. The Fig. 2.1(a) schematically represent a photoemission experiment: photon in – electron out, Fig. 2.1(b) and (c) represent energy and momentum conservation laws implemented to photo electrons, respectively. As we are investigating two-dimensional structures, there is no need to further discuss $\vec{K}_{\perp}$ and $\vec{k}_{\perp}$ values in the scope of the presented manuscript.

X-ray photoemission spectroscopy (XPS) is used to investigate atomic core levels. Atomic core levels represent an atom's fingerprints and chemical state. For instance, if an atom is an electron donor (e.g., it is oxidized), its electronic shell has one less electron, making it harder to be ionized; therefore, its core levels shift to higher binding energies. We used this approach for the characterization of Mo atoms sulfurization.

Another helpful tool is mean free path consideration. A photoemission signal exponentially decreases with the path distance that an electron must cross to reach a sample surface. One can use this property to determine the locations of particular atoms or layers by measuring the same XPS spectrum under different electron exit angles. Different angles will lead to known *sin*-dependent electron path distances.

Angle-resolved photoemission spectroscopy (ARPES) is used to investigate an energy-momentum dispersion of occupied valence band electronic states of materials with an oriented crystal structure. The valence band structure can also be considered a fingerprint. For instance, the Dirac cone-like electronic structure confirmed that we obtained quasi-free-standing graphene. In contrast, the position of the top valence band electronic states and ≈150 meV states splitting in the region of $\overline{\mathrm{K}}$ point confirmed that we obtained MoS_2 monolayer.

The most crucial information on ARPES spectra can be extracted from the energy-momentum dispersion near the Fermi level. A solid band structure defines most of

its properties, such as electrical and thermal resistivity, optical absorption, magnetic properties, and the ways of manipulating them. ARPES is an indispensable tool for investigating 2D and quasi-2D materials, superconductive and charge density waves materials, topological insulators, and Weyl semimetals.

2.1.2 The principles behind ARPES spectrometers

Transition and angular electron lenses modes

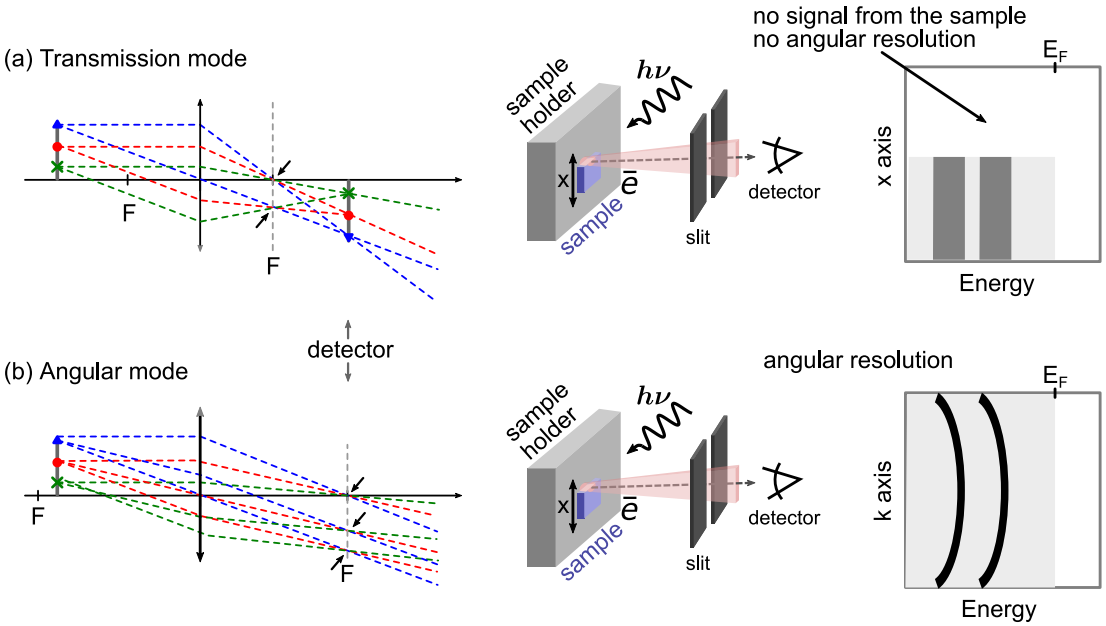

Figure 2.2: Schematic representation of work principals of transmission and angular electronic lens' modes.

We discussed how using monochromatic light, one can excite electrons to a vacuum, then analyze their energy (speed) and emission angle and make conclusions about the states they used to occupy. Now let us turn to a more technical question: How exactly can electrons be analyzed, and what happens when they leave a sample surface? The trajectory of freely propagating electrons can be influenced. Similar to photons, electrons that feature different energy (moving with a different speed) and different movement directions can be spatially separated using lenses. Unlike optical lenses, electron lenses are metallic apertures of a particular shape with an applied voltage potential.

Let us first discuss the angular resolution technique. Fig. 2.2 represents two different approaches realized in electron analyzers: transmission and angular. Let us imagine an electron source with a non-zero size and a converging lens nearby, as it is shown in Fig. 2.2(a). The lens's focus is located between the electron source and the lens. That makes it possible to produce an image of the electron source. However, more interesting

is what happens in the focal plane: all the trajectories with similar emission angles but from different spots of the electron source converge into the same spots! Using a simple lens, one can spatially separate electrons with different momentum.

The electronic lenses' advantage over optical lenses is that the focal distance of the electronic ones can be easily modified by changing an applied voltage. Therefore, given a fixed distance between the electronic source and the detector, one can change the location of the focal plane, as shown in Fig. 2.2(a,b). This allows one to choose the type of image focused on the detector. Thus, one can produce two types of images on the detector plate: the real image of the electron source and the distribution image of the electron angular directions. The first mode is called transmission, and the second is angular. ARPES images of valence band angular-momentum dispersions are obtained using the angular mode, while core levels studies can be performed using transmission one. Using transmission mode, one can also adjust the beam spot to be on the sample (see Fig. 2.2(a,b) right) and align the station. Aligning the station refers to the process of precise experimental station positioning related to the beam location and its focus.

Electron energy measurements: hemispherical electron analyzer

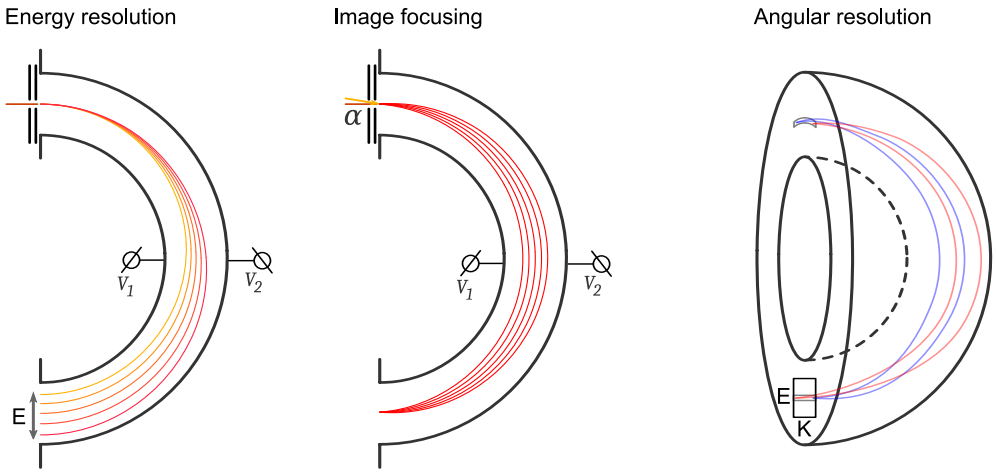

Figure 2.3: A schematic representation of electron trajectories in spherical electron analyzer: (a) related to energy resolution trajectories; (b) related to image focusing trajectories; (c) related to angular resolution trajectories.

Let us consider how electrons that propagate in the same direction but have a different speed can be spatially separated. There are two approaches: time-of-flight (ToF) and hemispherical deflection[107]. The time-of-flight detector separates electrons by the time it takes for them to fly a certain distance. In contrast, a hemispherical deflector separates the trajectories of electrons at different speeds. In our study, we use a hemispherical electron analyzer Scienta R4000, and will focus on its work principles.

The deflector consists of two R_1 and R_2 radii hemispheres. The central electrostatic field ($E(r)$) in between hemispheres is obtained by each hemisphere being kept at a different potential: V_1 and V_2, respectively.

$$E(r) = -\frac{V_2 - V_1}{R_2 - R_1}\frac{R_1 R_2}{r^2}$$

One can see that $E(r) \sim 1/r^2$ always points to the center of both hemispheres. To shortcut a math discussion, we can compare this central electrostatic field and electron orbits inside it with the Sun's gravity and planet's orbits. Planets orbits feature an elliptical shape, and the size of each ellipse is related to a speed of a planet: the higher speed, the bigger ellipse. The hemispherical deflector designates electrons with smaller kinetic energy to a smaller orbit and electrons with greater kinetic energy to a bigger orbit, as demonstrated in Fig. 2.3(left). In the first approximation, the distance between exiting hemispheres electrons will be linear to the energy difference ($\Delta x \sim \Delta E_{kin}$)[107].

Due to the hemisphere's geometrical constraints, electrons that can pass through the analyzer without hitting any of the hemispheres must have kinetic energies close to a specific value defined by the hemisphere's radius' and potentials. This value is defined as pass energy (E_p).

$$E_p = e(V_2 - V_1)/(\frac{R_1}{R_2} - \frac{R_2}{R_1})$$

Pass-energy (E_p) determines the energy resolution (ΔE):

$$\Delta E = E_p\left(\frac{w}{2R_0} + \frac{\alpha^2}{4}\right),$$

where $R_0 = (R_1 + R_2)/2$ is a mean radius, w is a slit width, and α is an angular acceptance. An angular resolution depends on the detector's channels' density and a beam spot's size. The size of a beam spot and the pass energy are trade-off parameters, as they are correlated with signal intensity and, therefore, the time required for acquiring the signal statistics.

Another practical implementation of the central electrostatic field with $E(r) \sim 1/r^2$ is a focusing role. It guarantees that electrons that enter the hemispherical deflector in the same spot but with different entering angles will be focused to the same spot on the way out (see Fig. 2.3(middle)). Using our comparison with the planet's orbits, we know that the trajectories in such potential must be closed and elliptical. Therefore, each half a period, they must cross.

Fig. 2.3(right) summarises the work principles of angular and energy resolution of the electron analyzer. Using electronic lenses, the angular distribution image (using angular mode) is projected along the hemispherical analyzer entrance slit. After passing the deflector, the angular resolved image is supplemented by an energy resolution in the direction perpendicular to the entrance slit.

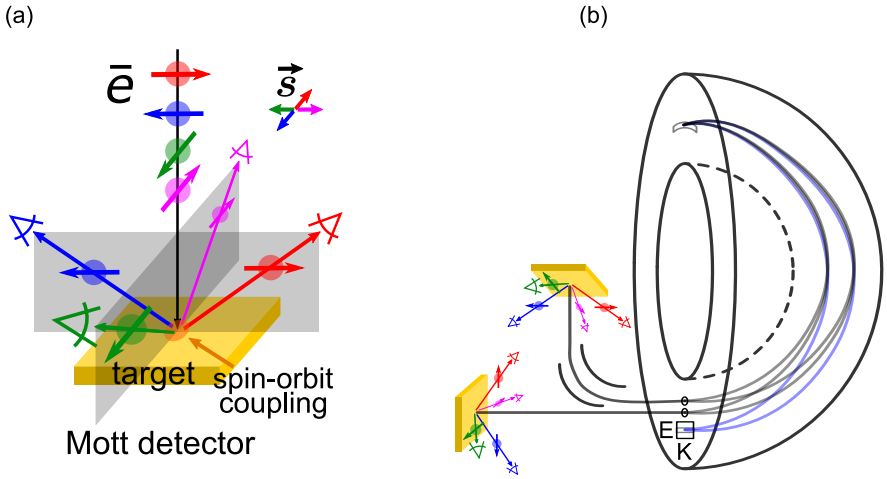

Figure 2.4: A schematic representation of electron trajectories for spin-resolved measurements: (a) represents spin-dependent electron scattering on gold film (the essence of the Mott detector); (b) demonstrates how two Mott detectors measure three components of the electron's spins.

Spin resolution

We must highlight that photo-emission spectroscopy can only determine the value of spin polarisation of an electron beam that enters the electron analyzer. This spin polarisation is correlated with the spin polarisation of the initial electronic states, but it is not the same. In order to spatially separate electrons with different spins, one can think about the Stern-Gerlach approach[108, 109]. However, for electrons, it is a practically impossible scenario. There are several other experimental approaches: spin-dependent scattering of electrons on heavy atoms due to spin-orbit interaction (Mott scattering)[110–112], exchange scattering on a magnetic surface [113, 114], and spin-polarised low-energy electron diffraction[115, 116]. We will focus on the Mott detector, as we used it in our study. Mott detector is far from demonstrating the top efficiency; however, it is the most reproducible and robust with respect to the spin-selective element[117].

The basic behind the Mott detector working principle is spin-dependent elastic scattering. Let us consider an electron with spin $\vec{s}$ that scatters on the radial potential ($V(r)$) of an atom with a Z-atomic number. It appears that while the incident electrons interact with the atomic radial potential, its spin $\vec{s}$ interacts with its temporary orbital angular momentum $\vec{\mathbf{L}}$. Mott has shown that this interaction has a sizeable effect on scattering in the case of electrons with rather relativistic velocities and heavy atoms with a high atomic number[110].

The mathematical result of the above mechanism leads to the different scattering cross-sections for electron beams with non-zero spin-polarization ($\vec{P}$)[109].

$$\sigma(\theta) = \sigma_0(\theta)[1 + S(\theta)\vec{P} \cdot \vec{n}],$$

where $\vec{n}$ is a unit vector that is perpendicular to the electron scattering plane; θ is an angle of electron scattering; $\sigma_0(\theta)$ is a differential scattering cross-section for a non-polarized electron beam; and $S(\theta)$ is the Sherman function[118] and must be calibrated experimentally. Schematically, the Mott scattering process is depicted in Fig. 2.4(a). One Mott detector can only resolve two spin components. In order to detect all three, one needs to use two Mott detectors that are located perpendicular to each other (see Fig. 2.4(b)). Mott detector is usually located just after a hemispherical analyzer near an angle-resolving MCP detector, as it is shown in Fig. 2.4(b).

Particular experimental details

For the presented study, ARPES and spin-resolved ARPES measurements were performed at room temperature. ARPES measurements were performed at the ARPES 1^2 end-station installed at UE-112 PGM-2 beamline, while spin-ARPES measurements at the spin-ARPES end-station installed at U125-2-PGM beamline at BESSY-II synchrotron radiation facility (Helmholtz Zentrum Berlin). At 1^2 ARPES end-station the energy-resolution was set to 10 meV and angular-resolution to 0.3°.

The spin-ARPES end-station is equipped with a combined Scienta detector with a 2D microchannel plate for ARPES measurements and a 3D Mott-type spin-detector that operates at 25 kV for electron acceleration. At the spin-ARPES end-station, the energy resolution was set to 45 meV and the angular resolution to 0.75°.

2.1.3 Behind the scene of spin-ARPES spectra

In this section, we will dive into the technical details of spin-ARPES measurements. These are the current manuscript's main results, and the spectra shown in the following chapters are the results of multiple and time-consuming measurements.

In this section, we will look behind the scene presented in papers and conference graphs and see how those representations are developed from the combination of the experimental design, raw data, and data analysis.

Mental models of spin-ARPES measurements In order to understand, design, and conduct an experiment, one needs to be able to imagine a simplified mental model of the experiment[119]. An experimental setup interacts with a physical system and then communicates this interaction to a scientist. To better understand this communication, a scientist should consider both probed physical properties and how these properties interact with an experimental setup.

According to the principle of parsimony, if a simplified understanding is enough, then one should hold on to that, e.g., electrons as particles, the whole experimental setup is just a means to filter down a particular signal, and a complicated electron lens system is only one lens.

What simplified assumptions do we consider when producing and quickly evaluating spin-ARPES data?
(1) Ground state electronic and spin properties of the investigated system are transferred directly to an experimental signal.
(2) Spin detector consists of two parts: a splitter of the electrons with opposite spin components in a given direction and an electron detector.
(3) Detected signal is proportional to the number of excited electrons, which is proportional to the density of states.

An experimental signal A mental model is the first step in understanding an experiment. After that, one should consider what elements of this model are too simplified to compensate for them by an experimental design.

What are the assumption's weak spots that one must consider when designing a spin-ARPES experiment and then analyzing the results?
(1) When we excite electrons from a system, it cannot be fully assumed as a ground state anymore: the final state effect must be considered.
(2a) The efficiency of the Mott detector is far from 100%. (2b) The efficiency of electron detectors is also not 100%. Moreover, as for different spin signals, different electron detectors are used – their efficiency could be different.
(3a) Detected signal is proportional to the number of excited electrons and the efficiency of a particular electron detector at a particular signal level. Moreover, this characteristic may even deviate in time.
(3b) The amount of excited electrons is proportional to the density of states and photoemission cross-section. Which is different for different exciting light energies and photoemission angles.
There are many other parameters, such as not 100% reproducible sample positioning, signal dependency from hardly reproducible sample focus parameters, and the existence of different sample regions that are similar enough to allow a shift from a previous sample position without notice. We must also mention experimental space and angular resolutions, which are diverse for different experimental settings.

One should consider mentioned above imperfections as practical challenges and deal with them using advanced experimental understanding and complementary experimental design and analysis.

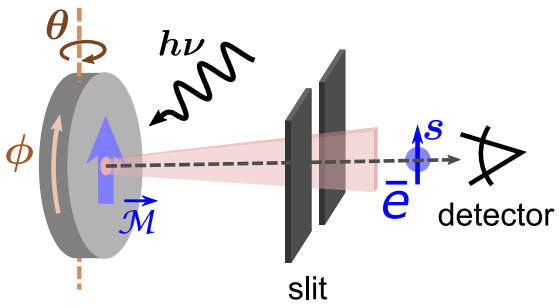

Figure 2.5: The mental model of ARPES measurements for normalization procedure.

Normalisation procedure: reverse magnetization Given all the uncertainties above, one can imagine an experiment attempting to solve one equation with multiple variables. To overcome this challenge, the normalization procedure is used: one needs to generate another equation with the same set of variables and then subtract one equation from another, keeping the only variables needed to be found.

Let us return to our particular experiment of modification of the spin electronic structure of MoS_2 on graphene on Co system. We investigate how a magnetic proximity effect influences MoS_2 valence band spin structure. From an experimental point of view, we are interested in a signal in electron detectors (that measure electrons with opposite spin components in an in-plane direction) for a particular sample geometry and magnetization.

A particular sample position and magnetization are constraints; however, we can use the system's symmetry to our advantage. Let us consider a spin detector. Its signal consists of two spin channels: spin channel 1 counts electrons with the spin component in the direction of sample magnetization, and spin channel 2 counts electrons with the opposite spin component. Let spin channels 1 count electrons with spin component co-directionally to sample magnetization, and spin channels 2 opposite.

In the assumption of ideal instrumentation and given a system symmetry (fundamentally physical property that can be proved), spin channels 1 and 2 must swap signals. Knowing this, we can normalize one signal to another and compensate for instrumental asymmetries. What if we magnetize a sample in the opposite direction to the initial one (keeping everything in experimental geometry the same)? Such approach is so-called **a remanent magnetization**.

normalisation procedure: sample rotation Looking at the picture Fig.2.5, one can think that rotation of the sample in the azimuth direction by 180°is similar to the remanent magnetization procedure. However, it will be a mistake in a general case of the C3 symmetry of the sample. In the case of MoS_2 monolayer (that feature C3 symmetry) and ARPES-measurements at $\overline{\mathrm{K}}$ point, rotation by 180°in azimuth direction will lead to measurements at $\overline{\mathrm{K}'}$ point.

However, in our case with the MoS_2/graphene/Co system, the symmetry is effectively C6, as graphene and Co have C6 symmetry and MoS_2 equally distributed in mirror domains. Therefore we can use 180°azimuth rotation for a normalization procedure.

2.2 Low energy electron diffraction

Using the low electron energy diffraction (LEED) technique, one focuses a beam of electrons with relatively low energy (from 20 to 200 eV) to a periodic crystal surface and then analyzes elastically scattered electrons. It is the method of surface investigation that can provide the periodicity of the surface structure.

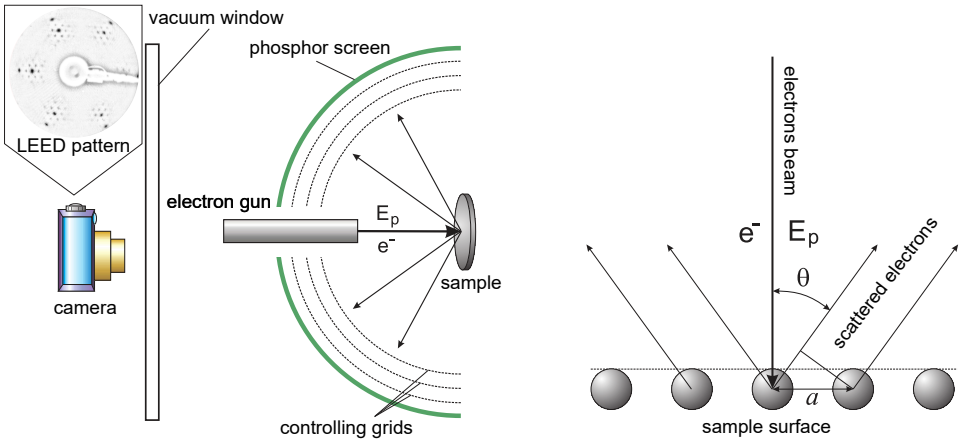

Figure 2.6: A schematic representation of low energy electron diffraction setup.

Let us consider incident and reflected electron beams as plane waves. Reflection assumes that electron's wavevector is conserved: $|\vec{k}_0| = |\vec{k}|$, where $\vec{k}_0$ and $\vec{k}$ are wavevectors the incident and reflected electrons respectively. On the other hand, constructive interference of reflected electrons on the surface can be described in the form of the Laue condition: $\vec{k} - \vec{k}_0 = \vec{G}_{hk}$, where $\vec{G}_{hk}$ is a reciprocal vector. The reciprocal vector is defined though the surface lattice vectors $\vec{a}$ and $\vec{b}$, and $\vec{G}_{hk} = h\vec{a} + k\vec{b}$. The wavevectors that satisfy the above conditions are described by Ewald's sphere method[120]. In other words, the diffracted pattern would represent a reciprocal lattice of the surface.

Due to the limited electron mean free path, the low electron energy diffraction is very surface sensitive. It only probes the first few layers of the solid. Aggregating the signals from different layers, one can determine the mismatch of adsorbates superstructures, surface reconstructions, and heterostructures layers. For instance, in the presented study, graphene and MoS_2 feature different lattice parameters, and it can be seen in LEED images. To describe such a structure, the following designation below is used.

Let us consider two lattices: lattice a and lattice b, that feature unit translation vectors ($\vec{a}_1$, $\vec{a}_2$) and ($\vec{b}_1$, $\vec{b}_2$). The designation would be $[(b_1/a_1)\times(b_2/a_2)]$, in case the lattices are rotated relative to each other the designation would be $[(b_1/a_1)\times(b_2/a_2)]R\alpha$, where α is the rotation angle.

Importantly, if a particular structure is not periodic or consists of many disoriented domains, one should not see any electron diffraction pattern. Thus, the only presence of an electron diffraction pattern already tells us about the high crystal quality of the sample surface. If a particular structure is presented in several rotational domains, one should observe an aggregation of rotated patterns. Such observations may be tricky to interpret. In the presented study, we demonstrated three aggregated 2×9 patterns rotated by 120°. If a vast amount of rotational domains is present, one should observe a circle of electron diffraction intensity, as we have for disoriented MoS_2 layers.

A typical low electron energy diffraction setup is schematically presented in Fig. 2.6. It consists of several distinct parts. An electron gun produces a monochromatic electron beam. A hemispherical fluorescent screen detects diffracted electrons. High-voltage grids accelerate electrons to amplify the signal on the screen (typically ≈6 kV). Filtration grids cut (suppress) elastically scattered electron backgrounds. A standard photo or video camera is used to record the data.

2.3 Scanning tunneling microscopy

The scanning tunneling microscopy (STM) method offers a tool to measure electron density in real space down to atomic resolution[121]. It analyses tunneling current values between a sample and a tip that can be precisely located in the proximity of different regions of the sample surface.

The fundamental physical principle behind scanning tunneling microscopy is the quantum tunneling effect. Let us consider a textbook example of an electron passing (tunneling) through a 1D rectangular potential barrier (U_0). The barrier has a width s and a height greater than the electron energy $U_0 > E$. It is a simplified model of the potential barrier between a probing tip and a particular sample surface area under an applied bias voltage.

The probability for an electron to pass the barrier can be described through the transmission coefficient T[122]:

$$T \propto e^{-2ks} \quad k = \frac{1}{\hbar}\sqrt{2m(U_0 - E)},$$

where k is the electron wave function inverse decay length. The exponential relation of the transmission coefficient to the barrier width can be generalized to the exponential relationship of the electron current between the sample and the tip to the distance between them. Thus a minor change in the distance leads to a significant change in

the current, which is implemented in scanning tunneling microscopy measurements as a tunneling current feedback loop.

The real current between the tip and the sample is defined by a slightly more complicated expression[123]:

$$I_t \approx G_0 \frac{4\pi^2}{e} \int_0^{eV} \rho_t(E_F - eV + \varepsilon)\rho_s(E_F + \varepsilon)|M|^2 d\varepsilon,$$

where I_t is a tunneling current; G_0 is a conductance quantum constant; $\rho_t(E)$ and $\rho_s(E)$ are the tip and the sample electron density of states respectively; V is a bias voltage; M is the tunneling matrix element that reflects transitions between the tip and the sample states[124]. $|M|^2$ represents tunneling probability and has an exponential relation to the distance between the sample and the tip. The integral is computed over energy (ε). The Fermi temperature distribution is assumed (simplified) to be a step function justified for low temperatures.

Taking into account the tip electron density ($\rho_t(E)$) in the equation, one should realize that should a change happen with the tip state – the tunneling current (I_t) will drastically change. For instance, the tip can pick up an atom from the surface. The tip's electronic structure is always present in scanning tunneling microscopy data. Another issue arises when one considers the non-atomic size of the tip. This issue is partially solved if the tip end is sharp and the states where the electron tunneling takes place are localized d or p orbitals with the controlled direction[125, 126]. This might be achieved in a tip made of d-band metals and semiconductors with p_z dangling bonds. It is crucial to control the orientation of the particular orbital. Thus, single crystalline tips are used. As the current primarily flows through the narrowest barrier, the natural atomic-size roughness of the tip plays to its benefit.

The final technique's realization is a precise x-y scanning of the sample with a tip under a bias voltage. This is realized through the implementation of peso motors. The tunneling current feedback loop provides resolution in z-dimension.

This page was intentionally left empty.

Chapter 3

Synthesis and characterisation of MoS_2 monolayer

In this section we modified a MoS_2 monolayer on Au(111) surface synthesis procedure[53, 54]: First, we prepared a clean Au(111) surface on a gold monocrystal to feature a "herringbone" pattern in the LEED image. Second, we deposited 1/3 monolayer of molybdenum atoms at room temperature. Third, we oxidized Mo atoms with sulfur flux by annealing the sample in a sulfur atmosphere. Finally, we produced ≈0.4 MoS_2 monolayer coverage of similarly oriented domains.

3.1 MoS_2 on Au synthesis

3.1.1 Preparation of a clean Au(111) surface

The Au(111) sample (MaTecK GmbH) was prepared by cycles of Ar+ sputtering and annealing to 600°C. The surface quality was checked by following LEED measurements. The clean Au(111) surface reconstructs into the characteristic $(22 \times \sqrt{3})$ "herringbone" pattern. Compression of the atoms in the surface layer by approximately 4.5% in the close-packed [110] direction induces this reconstruction. This surface compression produces a mismatch between the topmost layer of Au and the bulk crystal, which causes a shift in lattice packing and yields alternating bands of fcc- and hcp-registered surface atoms. Regions are termed "soliton walls," where atoms in the surface-most layer traverse bridge sites and separate fcc and hcp regions. These soliton walls exist in pairs that run in three equivalent directions to relieve stress isotropically and are referred to as herringbones.

3.1.2 Molybdenum atoms deposition

For Mo deposition, we applied the physical vapor deposition technique. We used a 1 mm Mo rod with 99.95% purity loaded into the Tectra e-beam evaporator. We chose the following parameters for deposition: 1.5 kV of high voltage on the Mo rod and 24 mA

emission current from the filament. For our experimental geometry, these parameters provided a comfortable Mo atoms flux rate of 1/10 monolayer in one minute. During the deposition, we kept the pressure in a vacuum chamber below 1×10^{-9}mbar.

We deposited 1/3 of the Mo monolayer on the room-temperature gold substrate. We have not investigated how to increase the amount of MoS_2 in the final system, as it was out of the focus of the present work, and ≈ 0.4 MoS_2 coverage was sufficient for spectroscopic study.

Another reason for us to stick to these parameters is that they provide almost 100% of MoS_2 domain orientation, which is crucial for spin-resolved spectroscopic study (see more in sections 3.2.2 and 4.1.4). We did not make a systematic investigation on how we reached such high quality, but it appeared to be an often discussed topic. Many studies [60] highlight their systems to feature a small number of mirror domains (domains rotated at 180° to each other).

3.1.3 Sulfur atoms deposition

After deposition of 1/3 of Mo monolayer, we oxidized it with sulfur: Firstly, we increased the sampled temperature to 600°C, then introduced a sulfur flux and annealed for 70 minutes. Then, we stopped the sulfur flux, maintaining the sample temperature, and lowered the sample temperature.

We found that a temperature of 600°C is optimal for MoS_2 synthesis: Lower temperatures are possible, but it would require more than 70 minutes for all Mo atoms to be oxidized (more details in 3.2.1 section). Using higher temperatures did not lead to the MoS_2 formation. We presume that sulfur atoms reflect from an overheated surface before they are involved in a chemical reaction.

In the case of using less than 70 minutes, the oxidation reaction is incomplete; however, already oxidized Mo atoms form perfectly oriented MoS_2 monolayer islands. Such long time required for the synthesis can be explained by a strong chemical bonding of Mo atoms to the Au substrate. In case of other substrates the synthesis can be complete in a few minutes (see for MoS_2/graphene/Ir [56] and 3.3.2 section).

For sulfur evaporation, we used a self-made sulfur source (see Fig. 3.1), where at the temperature of ≈400°C, FeS_2 decomposes to FeS and presumably atomic sulfur. FeS_2 crystals were loaded into the crucible and heated up using infrared radiation from the filament. We used a massive crucible to let it equilibrate: the temperature inside the crucible and outside, where we attached a thermocouple, had to be the same.

We chose to use FeS_2 crystals instead of bulk S compounds to have more control over the reaction in the high vacuum environment: the FeS_2 decomposition happens at 400°C. At the same time, pure sulfur at room temperature already features a vapor pressure of 3×10^{-4}. Another advantage of $FeS_2 \rightarrow FeS + S$ reaction is the possibility

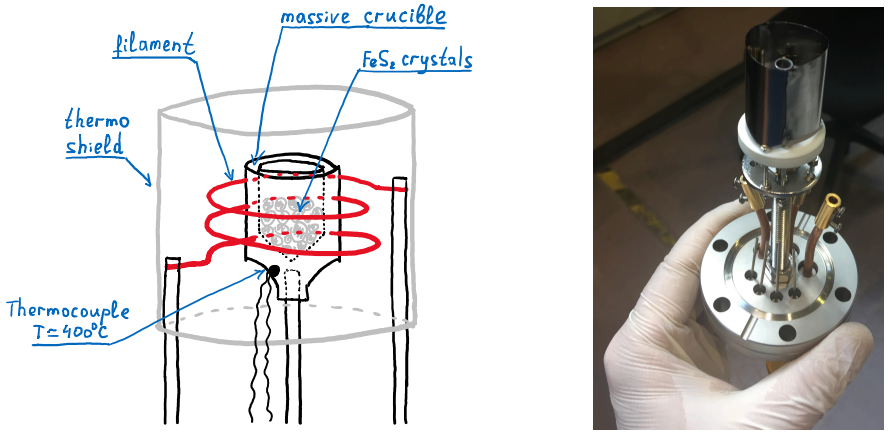

Figure 3.1: The schematic cartoon picture and the photo of the sulfur source: FeS_2 grains are loaded into the massive crucible to which the thermocouple is attached; a thick filament is placed around the crucible and heats it mostly with infrared radiation; the thermoshield around the crucible and the filament made from Ta foil raises the efficiency of heating and the vacuum chamber tube from heating up, therefore, improving the vacuum conditions.

of atomic sulfur formation. In contrast, the sulfur atmosphere of pure sulfur primarily consists of clusters (in particular S_8 and S_6), which should demonstrate less reactivity.

We did not specifically investigate what type of sulfur (atomic or cluster) oxidized Mo atoms in our experiment. However, mass spectrometry measurements show a dominant peak at 32 m/z (corresponds to S atoms).

In our experiment geometry, to measure the sample temperature while annealing in the sulfur flux, we had to turn away the sample surface from the direction of the sulfur flux. This geometrical variation did not influence the synthesis result. We tried to run the whole synthesis process without turning the sample surface to the original direction of the sulfur flux – the synthesis result remained the same (see Fig.3.2). Here we assume that for Mo oxidation, sulfur flux can be treated as any other gas partial pressure and measured using mass spectrometry. A mass spectroscope can be placed anywhere in the vacuum chamber. We presume that such behavior can be explained by a high room temperature sulfur vapor pressure: after a small amount of time, when sulfur atoms hit walls, they evaporate back.

3.1.4 Sulfur source working principles

FeS_2 crystals contain a lot of crystalline hydrates so that the water is not removed from the crystals after a standard vacuum source baking procedure (baking at 130 – 150°C for a few days). Before starting sulfur evaporation, one must slowly increase FeS_2 temperature from 200°C to 370°C keeping the vacuum pressure under 5×10^{-7}mbar. This would remove most of the water from FeS_2 crystals. If one should use higher

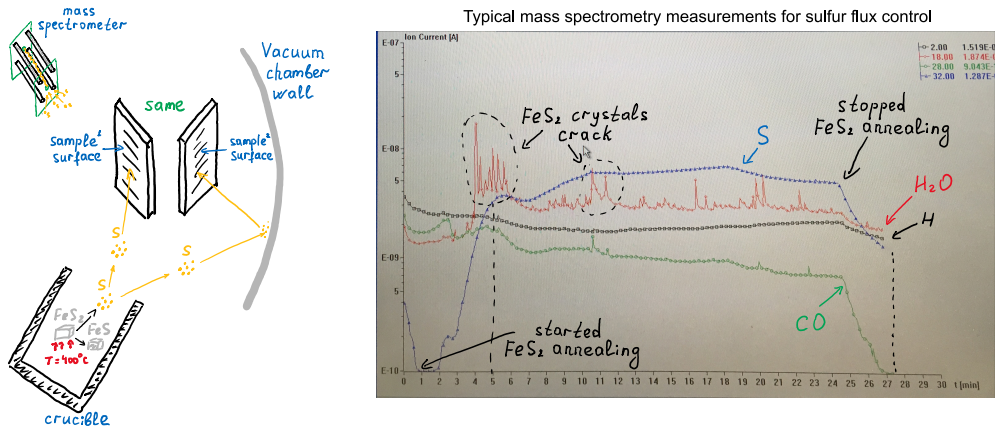

Figure 3.2: Left – a cartoon picture represents the mechanism of atomic sulfur flux production, its deposition on the sample surface, and controlling the sulfur flux. When annealed up to 400°C FeS_2 decomposes to FeS and atomic sulfur. The sulfur flux is either directly aimed at the sample surface or indirectly reflected from vacuum chamber walls – there is no experimental difference. As there is no difference, the spectroscope can be placed anywhere in the vacuum chamber to measure the sulfur flux as if it was a gas. Right – a typical mass spectrometry while sulfur flux production.

pressure, it might break (through oxidation) a sulfur source filament. Such a procedure might take a few days.

After the preliminary dehydration, one can start mass spectrometry measurements and slowly increase the FeS_2 temperature up to 400–420°C keeping the vacuum pressure under 5×10^{-7}mbar. The sulfur source will be ready when the sulfur ion current becomes larger than the water ion current. It is essential because significant oxygen pressure (comes from water) can also participate in Mo oxidation instead of sulfur. Such a procedure only takes a couple of hours.

We found that FeS_2 purity does not influence the final MoS_2 synthesis result: we tried a chemically obtained compound with 99.9% purity and a natural FeS_2 mineral.

After some time, the amount of FeS_2 decreases to the point where much less sulfur is produced during 400°C annealing. We tried to increase the temperature, restoring the sulfur flux, but the CO ion current became larger than for the sulfur. Such deviation does not influence the synthesis result but can be recognized as a signal to renew the FeS_2 source material.

In conclusion, we strongly suggest using mass spectrometry to control the sulfur flux, as at different life cycles, it can mainly produce H_2O, S, or CO flux.

On the right side of Fig. 3.2, one can see that a sulfur flux is allowed not to be very stable – it does not reflect on the synthesis results as long as sulfur flux is around 5×10^{-7}mbar. Sometimes the amount of water or hydrogen may significantly rise; it also does not lead to any significant changes in the resulting MoS_2 sample quality. We refer to those partial pressure perturbations as the mechanical crack of FeS_2 minerals.

As already mentioned, even a massive crucible inevitably leads to some temperature gradients and, therefore, sulfur flux inertia, which can be seen in the mass spectrometry data. (Author apologizes for having a photo instead of a proper data set: the software did not record the data set, and we did not fix this problem, as we only needed to control the sulfur flux value visually).

3.2 MoS_2 on Au: system characterization

3.2.1 Different stages of MoS_2 monolayer formation on Au(111) crystal: XPS measurements.

MoS_2 monolayer can be considered as a three-layer system: S-Mo-S. Fortunately, to synthesize MoS_2, one can limit efforts to place molybdenum and sulfur atoms in the same place and add some energy via annealing the system. In these conditions, Mo and S atoms self assemble into MoS_2 following Au(111) surface symmetry. In our experiment, we deposited molybdenum on the Au(111) substrate and then annealed the system in the presence of a sulfur flux.

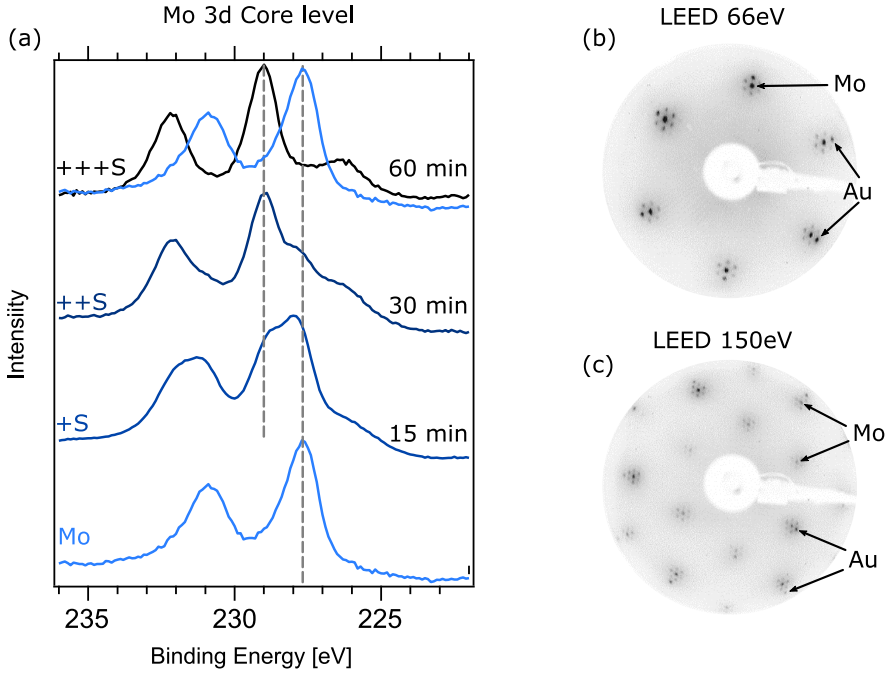

Figure 3.3: (a) Mo 3d XPS spectra evolution (from blue to black) of the system of deposited Mo atoms atop Au(111) monocrystal (the lowest and the black spectra) and its subsequent annealing in the sulfur flux 15, 30, and 60 minutes. When Mo is sulfurized, the Mo 3d peak shifts 1 eV to higher binding Energy. (b,c) LEED images of MoS_2 monolayer on Au(111) substrate taken at 66 and 150 eV of the electron beam. Both LEED images suggest a 10×10 superstructure.

Fig. 3.3(a) demonstrates different stages of MoS_2 coverage formation. Blue (right) and Black (left) spectra on the top represent the Mo 3d core level of deposited on Au(111) Mo atoms and MoS_2 monolayer, respectively. One can see that they look alike while being shifted by around 1 eV. This is expected due to chemical environment difference – sulfur drag electrons from Mo atoms reducing the electron screening effect. MoS_2 additionally features a small spike to the right of Mo 3d (at around 226 eV); this peak represents S 2s core level.

One can see Fig. 3.3(a) as an evolution of Mo 3d core level in time while Mo atoms are being sulfurized. After 15 and 30 minutes of annealing of the system in sulfur flux, spectra look more like a mix of pure molybdenum and MoS_2 Mo 3d core levels. In addition, LEED images of these intermediate stages look exactly as the ones of the final MoS_2/Au(111) system (see Fig. 3.3(b,c)) with less intensive reflexes. Here we conclude that Mo atoms atop Au(111) single crystal directly reconfigure into MoS_2 monolayer while being annealed in a sulfur flux.

3.2.2 MoS_2/Au(111) symmetry and geometry: LEED, PED, and STM studies.

Fig. 3.3(b) represents LEED image of MoS_2/Au(111) system. It consists of two groups of reflexes: larger and smaller hexagons that correspond to Au(111) and MoS_2 structures. Around a smaller hexagon (MoS_2 reflexes), one can see a moire pattern. A larger hexagon (Au(111) reflexes) shares the location with the moiré reflexes around a smaller hexagon. One can claim that from a double intensity of mentioned reflexes. Such configuration suggests the 10×10 superstructure. In order to confirm this observation, we present a similar LEED image but with a higher energy of electron beam: this allows us to see a second Brillouin zone in Fig. 3.3(c). In the second Brillouin zone, Au(111) reflexes are well separated from a moiré MoS_2 ones.

LEED measurements (see Fig. 3.3(b,c)) provide us with hexagonal patterns that can refer to both three-fold and six-fold symmetry. Both MoS_2 monolayer and Au(111) surface feature three-fold symmetry. Previously published results[59, 60]) suggest that MoS_2 monolayer can be aligned with Au(111) surface, and MoS_2/Au(111) will feature three-fold symmetry, or it can be aligned oppositely and MoS_2/Au(111) will feature six-fold symmetry. In the last case, mirror domains of MoS_2 islands are formed (domains that are rotated 180° relative to each other). The presence of mirror domains can be a problem when measuring an out-of-plane spin component in spin-resolved photoemission spectra, as signals from mirror domains from $\overline{\mathrm{K}}$ and $\overline{\mathrm{K}'}$ points meet in the same spin channel and "cancel" each other. Such problem is present in MoS_2/graphene/Co system and well explained in 4.2.5 and 1.5.2 sections.

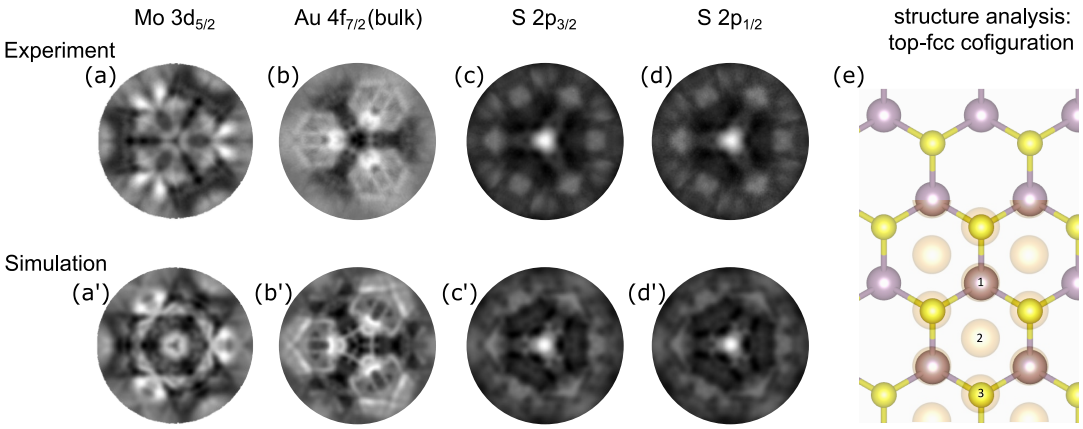

Figure 3.4: (a-d) Photoelectron diffraction: representation of the experimental data (first line) and simulations (second line). (a,a') - Mo $3d_{5/2}$ core level; (b,b') - Au $4f_{7/2}$ (bulk component) core level; (c,c') - S $2p_{3/2}$ core level; (c,c') - S $2p_{1/2}$ core level. (e) Schematic representation of the atomic structure of the simulated system. The top-fcc configuration agreed best with the experimental results. R-factors (R) and inner potentials (V_0) have the following values: R_{MoS_2}=0.23 and $V_{0\,MoS_2}$=11.8, R_{Au}=0.22, $V_{0\,Au}$=13.7

In order to check the presence of mirror domains, we conducted photoemission diffraction (PED) study of the system (see Fig. 3.4(a-d)). PED data are not intuitively straightforward; therefore, one needs to theoretically simulate the structure and compare it with data to confirm presumed structure correctness. Looking at the trigonal structure of Fig. 3.4(a-d) data sets, one can conclude that MoS_2 monolayer features C3 symmetry and may only contain an insignificant amount of mirror domains. Simulating different atomic structure configurations and comparing them to experimental data, we found the best fit for the top-fcc configuration of MoS_2 monolayer, as it is presented in Fig. 3.4(e). Simulated data sets for this configuration fit well with experimental results and are presented in Fig. 3.4(a'-d').

For further clarity, one is suggested to look at the figure Fig. 3.13 in section 3.4.2, where two mirror domains are equally present. For such a case, both PED measurements and simulations show six-fold symmetry, which is interpreted as a combination of the signals from two mirrored trigonal structures.

STM measurements presented in Fig. 3.5) provide us with an image of MoS_2 domains' appearance, their orientation, average size, and matching to Au(111) substrate. Fig. 3.5(a) shows that MoS_2 monolayer coverage consists of equally distributed and similarly sized domains of a triangular shape. Fig. 3.5(b) demonstrates that the average domain size is around 30 nm, and all of the triangular-shaped domains are turned in the same direction, which is consistent with PED data. Fig. 3.5(c) clarifies that domain' shape may variate from a triangular form. It also shows that not covered with MoS_2 Au(111) surface does not feature an atomic resolution. We refer to this point as the fact that the annealing of the sample up to 500K is not enough to clean the Au(111) surface.

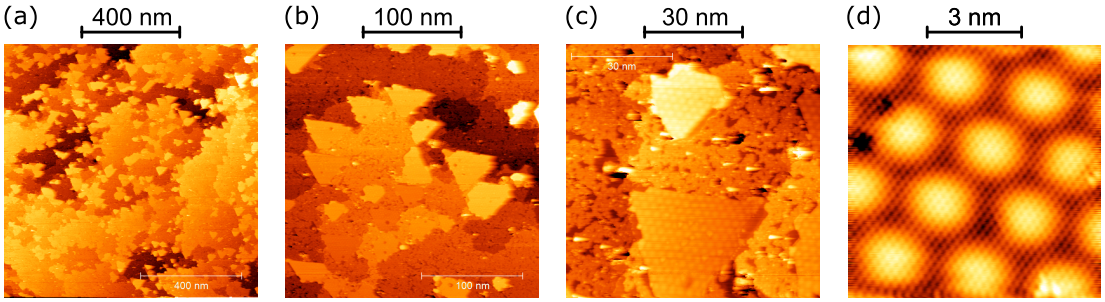

Figure 3.5: STM images of MoS_2 monolayer coverage on Au(111) crystal in different scales. Bias voltages and tunneling currents were 1 V, 0.1 nA.

Finally, Fig. 3.5(d) demonstrates an atomic resolution of MoS_2 monolayer on Au(111) surface and corresponding 10x10 moire structure which is consistent with LEED images in Fig. 3.3(b,c).

3.3 MoS_2/graphene/Co synthesis

3.3.1 Graphene/Co synthesis

We prepared a monolayer of graphene on Co thin film using a modification of the procedure reported in Ref. [14, 127]: First, we prepared a clean W(110) surface by a consecutive procedure of oxygen treatment followed by several flashing procedures. Oxygen treatment refers to the annealing of the sample at oxygen pressure while flashing refers to a quick sample anneal up to $\approx 2000°C$. Second, we deposited 10 – 12 nm of Co thin film using the physical vapor deposition method. Third, we produce a graphene monolayer using the chemical vapor deposition (CVD) method.

Preparation of a clean W(110) surface

We start with the preparation of the W(110) single crystal as a base substrate for our future system. The crystal was mounted on an Omicron-type sample holder with a hole drilled (cut) in the middle. The hole allows heating of the sample using the e-beam heating method efficiently.

In order to prepare the W(110) surface, we carried out a consecutive procedure of oxygen treatment followed by flashing (super high and fast annealing) in high vacuum conditions. We used the following parameters for the oxygen treatment procedure: oxygen pressure of 1×10^{-7}mbar and sample temperature of around 900°C. For the flashing procedure, the pressure in the chamber was kept below 5×10^{-8} mbar, while the sample temperature was quickly ramped up to $\approx 2000°C$ and kept at this level for 10 – 15 seconds and then lowered.

The meaning of the oxygen treatment is to remove the surface carbide. While annealing, the sample carbon atoms diffuse with increased thermal velocity. When

they reach the surface, they react with oxygen atoms and leave the sample as carbon monoxide or carbon dioxide. As a side-effect, tungsten also reacts with oxygen, forming the oxide. Such tungsten oxide does not dissolve in the crystal but stays only at the surface. Tungsten and tungsten oxide have different expansion coefficients; therefore, quick temperature increment leads tungsten oxide to go away (to peel off).

In summary, to prepare the clean W(110) surface, one shall check for the presence of tungsten carbide and tungsten oxide on the surface of the crystal. Both manifest themselves in LEED measurements. A complicated superstructure indicates the presence of tungsten carbide, while 2×2 indicates tungsten oxide.

Preparation of Co film

In order to prepare the Co film, we used the molecular beam epitaxy (MBE) method. On a freshly prepared W(001) surface, we introduced the beam of Co atoms generated in an e-beam Co source. The Tungsten surface must be freshly cleaned, as we count on the lattices match between W(001) and Co(111). A buffer of any kind may prevent the formation of an orientated Co film, as deposited Co atoms would not maintain the W(001) crystallographic orientation.

Using the term fresh, one may count the time during which W(001) surface would adsorb water atoms from the environment. For a pressure of 1×10^{-9}mbar, which we usually have in our preparation chamber, the process of adsorbing water or other residual gases may occur in dozens of minutes. In order to protect a clean W(001) surface for a longer period after performing the last oxygen treatment, one can postpone the flashing procedure until a little before Co deposition.

The thicknesses of Co thins film may differ. In most cases, we deposited 10 – 12 nm: Thinner films tend to crack during the subsequent graphene or MoS_2 synthesis; the thicker films do not bring any advantage for our goals (synthesis of graphene and MoS_2 and in-plane magnetization of Co film). We successfully tried obtaining the graphene/Co system on a Co film with a thickness of 50 – 60 nm. In principle, one can try to deposit even more.

In order to finally orient the Co film along W(100) after the deposition process, one should heat the sample to 400 – 500°C. We checked the crystal quality of the Co thin film using the LEED method. The obtained Co film is chemically quite robust and can be left in high vacuum conditions for days and then be used for graphene preparation.

Graphene synthesis

We used the chemical vapor deposition (CVD) method to obtain graphene on the Co(111) surface. The idea behind this approach is that carbon-containing gas catalytically cracks on the hot Co(111) surface, and carbon atoms diffuse in the near-surface region. At a particular surface temperature, the energetically favorable transition happens towards graphene formation. The Co(111) surface plays three key roles: First, being hot demonstrates catalytic properties that mediate carbon-containing gases' cracking. Second, the solubility of carbon in cobalt is low. Therefore, carbon does not dissolve into the bulk but instead stays on the surface. Third, the mismatch between the Co(111) surface and graphene is only 2%, which makes the most favorable for the carbon atoms to self-arrange into a graphene monolayer.

For the synthesis, we used the following procedure:
(1) We released 7×10^{-7}mbar of propene (C_3H_6) into the vacuum chamber. Some of it became adsorbed on the Co surface.
(2) We ramped the sample temperature up to 680°C and kept it in the region between 675 – 685°C for 12 minutes. A less than 12 minutes process led to smaller graphene coverage. A longer than 12 minutes process did not lead to a high graphene coverage. However, it led to more carbon atoms diffusing into the tungsten crystal, which is negative, as it complicates a tungsten crystal cleaning procedure.
(3) Keeping the sample temperature, we closed the valve to propene gas and waited until it pumped down (usually, it takes less than a minute). We found that this particular step can replace a recrystallization procedure[128].
(4) We slowly ramped down the sample temperature. In the case of fast cooling, the Co film often cracks, as expansion coefficients of tungsten crystal and cobalt film are different.

Simplified recrystallisation idea:

Graphene formation is a favorable outcome of a cracking process only in a particular temperature window. Both lower and higher temperatures result in cobalt carbide formation. There are different regions within the graphene formation window: at a lower temperature, graphene forms small domains, and those domains can feature a different orientation. At a higher temperature, graphene forms bigger domains with higher quality; moreover, a complete domain orientation may be reached.

The authors of the study [128] show that the structure can be finalized later after graphene synthesis. Small misoriented graphene domains can recrystallize and form a single domain. This means that the graphene coverage can still physically consist of several parts, but they are all oriented in the same direction. This process happens while annealing the sample in high-vacuum conditions after polycrystalline graphene

was already formed on the Co(111) surface. The trick allows one to use a recrystallization process at a bit higher temperature than the maximum temperature for graphene synthesis.

Why can't one use the ideal synthesis parameters from the beginning? The problem arises when experimental parameters inevitably differ from one sample to another and from one experimental station to another. The precise temperature values depend on the precise C_3H_6 partial pressure and Co thin film quality, for instance, roughness. Measurements of the precise temperature always depend on some (sometimes variable or unknown) sample parameters. For instance, the roughness of the particular sample spot defines emissivity, affecting the pyrometer's surface temperature measurements. The sample thickness, size, and the way it is mounted on the sample plate would effects temperature measurements made by the thermocouple attached to the manipulator.

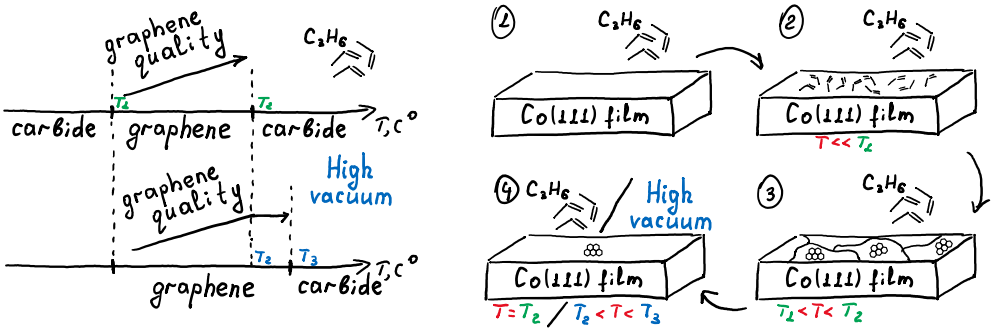

Figure 3.6: A cartoon image of the recrystallization process. The left graph demonstrates temperature regions where the propene cracking process leads to graphene or carbide formation. The right image demonstrates how (1-2) propene is adsorbed by the Co(111) surface; (2-3) how the propene cracking process results in polycrystalline graphene formation; and (3-4) how graphene recrystallizes under high vacuum conditions and slightly increased temperature.

It should be noted that after the formation of one monolayer of graphene on Co(111), the synthesis process stops. The formation of a second or third monolayer not possible as graphene covers the Co(111) surface and blocks the following cracking reaction. Such behaviour caused by the strong chemical bonding between graphene and Co substrate (see XPS section 3.3.3 and Fig. 3.10(a)).

Stability of graphene/Co system

The graphene protects the Co substrate from the influence of the environment. The graphene/Co system is quite robust: one may leave it for a long period in a vacuum chamber or even take it out to the ambient pressure – the system will remain. One may use the system for other purposes, such as direct mechanical transfer of MoS_2 via scotch tape.

Although the adhesion coefficient of graphene is low, after exposition to a significant residual gas, the graphene/Co surface still gets covered and must be cleaned before the following synthesis stages. Fortunately, in height vacuum conditions, the system remains stable up to the temperature of 600°C, where all the adsorbed residual gases eliminated.

3.3.2 MoS_2 synthesis

Four-step procedure of MoS_2 synthesis

We prepared a high-quality monolayer of MoS_2 using MBE. By tuning the synthesis conditions, we found an optimal four-step growth procedure:
(1) deposition of 1/3 of Mo monolayer;
(2) rising the sample temperature up to 600°C;
(3) annealing in a sulfur flux for 12 minutes (at sulfur pressure of $5 \cdot 10^{-9}$ Torr);
(4) termination of the sulfur flux followed by lowering of the sample temperature.
The procedure represents a modification of the one reported in Ref. [20]. We modified this procedure by varying synthesis parameters and preliminary checking the results via LEED and XPS.

Below we list some systematic observations based on many attempts with slightly different synthesis parameters. We frame it to answer the questions about why we use specific synthesis parameters and what will happen if we change them. The questions are the following:
- Why do we use only 1/3 of Mo monolayer?
- Why do we use 600°C? What is the temperature dependence?
- Why do we anneal in sulfur flux for 12 minutes?
- Why do we first raise the sample temperature and only then introduce sulfur flux?
- Why do we use sulfur pressure of $5 \cdot 10^{-9}$ Torr?
- Why do we terminate the sulfur flux and only then lower the sample temperature?

Molybdenum monolayer coverage dependence

In Ref. [20], the authors investigated the dependence of MoS_2 growth on the synthesis parameters in the MoS_2/graphene/Ir system. Via STM measurements, they determined that when more than 0.4 Mo monolayer is deposited, it results in Volmer-Weber type growth (the formation of a second layer). We tried depositing different amounts of Mo atoms on the graphene/Co system. We concluded that deposition of more than 1/3 of Mo monolayer significantly increases the amount of misoriented MoS_2 domains, which manifest themselves as a circle in the LEED image (see Fig. 3.7).

In Ref. [56] the authors propose to use subsequent growth cycles of the procedure to increase the MoS_2 coverage in the MoS_2/graphene/Ir system. We tried this approach for the MoS_2/graphene/Co system: it only increased the amount of misoriented MoS_2 domains, similarly to the case of more than 1/3 deposited Mo atoms.

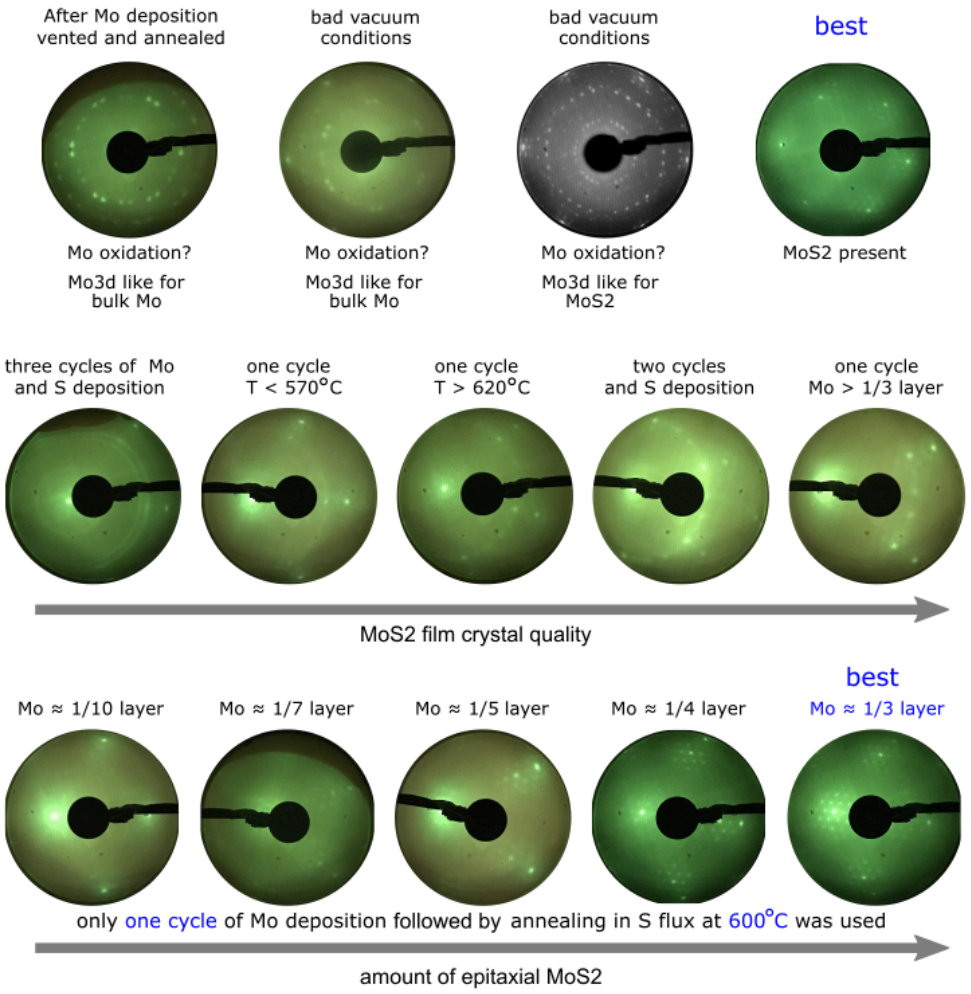

Figure 3.7: LEED images of unsuccessful and semi-successful attempts to synthesize MoS_2 on graphene/Co system. Arrows represent our conclusions on how the sample quality of MoS_2/graphene/Co depends on different synthesis parameters

Synthesis temperature dependence.

Unlike the case of MoS_2 on Au(111) described in section 3.1, the annealing temperature in sulfur flux strongly influences the MoS_2 quality. Unlike the strong chemical bonding between Mo and Au(111) mentioned in section 3.1.3, Mo atoms are somewhat free on the graphene substrate. Therefore, the mobility of Mo atoms is higher, making the oxidation process easier and faster. This leads to many possibilities of the formation of misoriented MoS_2 formation.

Fig. 3.7 second line, second and third LEED insets show that both lower and higher than 600°C temperatures result in circle of MoS_2 reflexes in LEED pictures, which is clear evidence of formation of misoriented MoS_2.

Following the explanation proposed in Ref. [20] for lower than we used temperatures, we explain this misorientation from insufficient mobility of Mo and S atoms or MoS_2 islands. Formed domains do not possess sufficient kinetic energy to line up along the graphene structure. We explain the misorientation from too-high islands' mobility for higher temperatures. Domains can be easily formed with different orientations, but they cannot easily line up along the graphene structure when cooling the system down, as the domains are already significantly big. The last statement, however, is pure speculation that is not supported by any systematic synthesis attempts at higher temperatures, STM studies, or molecular dynamics calculations.

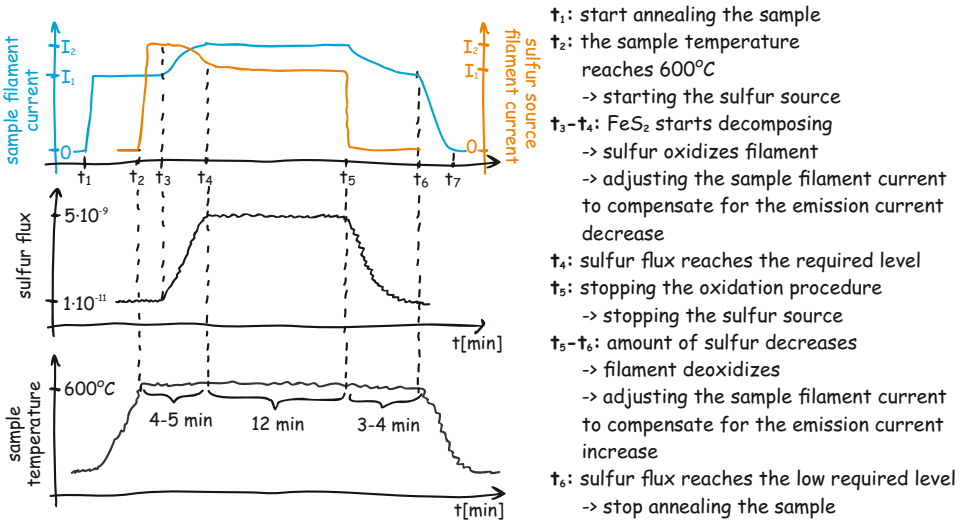

Figure 3.8: sketch of annealing in sulfur flux process

The dependence of crystal quality on the time of annealing in sulfur flux

The aim was to anneal the sample at 600°C at a sulfur pressure of $5 \cdot 10^{-9}$ Torr. In order to make the procedure reproducible, we used the following approach: first, reach the sample temperature; second, introduce sulfur flux. The sulfur source requires 4-5 minutes to reach the required parameters and 3-4 minutes to stop producing sulfur atoms (see Fig. 3.2 and Fig. 3.8). We used a measurable amount of time that would last longer than the sulfur source ramping up and ramping down times. This time was 12 minutes.

On the other hand, unlike for the case of MoS_2 on Au(111), we have never observed any unoxidized Mo via XPS measurements. Therefore, we believe one can decrease the annealing time in sulfur flux. The oxidation time was similar to the case of MoS_2 synthesis on graphene/Ir(111)[56].

However, unlike Ir in the graphene/Ir(111)[56] system, Co in our graphene/Co system can be oxidized by sulfur. This oxidation occurs during the sulfur intercalation

process underneath graphene (see more in 3.3.3). If one aims to decrease the amount of cobalt sulfide in the graphene/Co substrate, the annealing time in sulfur flux must be as little as possible.

Synthesis order: first raise the sample temperature then introduce sulfur flux

After we tried to synthesize MoS_2 at different annealing temperatures in sulfur, we observed many cases of misoriented MoS_2. We tried to carry out the recrystallization procedure, as we did for graphene (see 3.3.1); however, recrystallization did not take place. We concluded that if we vary the sample temperature in the presence of a sulfur flux, we will perform an unreproducible procedure: MoS_2 will be formed differently at different sample temperatures and it would not be possible to change it after. As we did not observe a significant difference in synthesis results when we varied the sulfur flux, we decided first to reach the precise sample temperature and only then adjust sulfur flux. Such approach was the easiest one to be experimentally reproducible.

The sulfur pressure dependence

We did not observe significant dependence of the synthesis result on sulfur flux: we tried varying the flux from $1 \cdot 10^{-9}$ to $1 \cdot 10^{-8}$ Torr, the vacuum conditions were from $1 \cdot 10^{-7}$ to $1 \cdot 10^{-6}$ Torr correspondingly. We presume that in our case, the limiting factor was the amount of H_2O rather than the amount of sulfur: we kept the pressure of H_2O below the pressure of sulfur.

Synthesis order: terminate the sulfur flux, then lower the sample temperature

As we did not observe a significant difference in synthesis results when we varied the sulfur flux, during the synthesis, we chose to adjust the sulfur flux parameter keeping precise sample temperature instead of adjusting the sample temperature keeping the precise sulfur flux. See more in 3.3.2.

3.3.3 Side-effect of MoS_2 synthesis: sulfur intercalation into graphene/Co

Oxygen intercalation into graphene/Co

Sulfur is located below oxygen in the periodic table and has similar chemical properties. Here we discover how oxygen oxidizes the graphene/Co system and how it may be similar in the case of sulfur.

A number of publications studies the effects of intercalation of different atoms under graphene in the graphene/Co system, such as gold[10], bismuth[130] and oxygen[129]. A study with oxygen intercalation[129] shows that when the graphene/Co is annealed

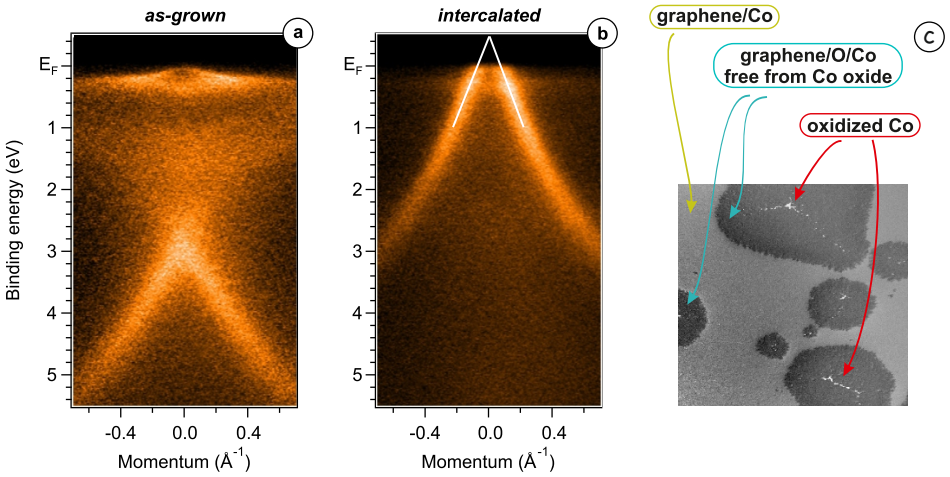

Figure 3.9: (a) ARPES dispersion of graphene/Co system as grown. (b) ARPES dispersion of oxygen intercalated graphene/Co system. Measurements were performed using the He II line of a He discharge lamp (40.8 eV). (c) SEM image of partially oxygen intercalated polycrystalline graphene/Co(0001). Images are adopted from [129]

in the presence of oxygen, oxygen atoms intercalate underneath graphene and make graphene quasi-free-standing. ARPES measurements show corresponding quasi-free-standing graphene features hole-doping. The study also demonstrates that oxygen intercalation does not lead to oxidation of the Co film: only the top layer of Co is affected, and oxygen atoms are not detected in the bulk of the Co film.

Fig. 3.9(a) demonstrates a classic ARPES dispersion of graphene/Co in the region of $\overline{\text{K}}$: Graphene is not quasi-free-standing but instead bonded to the Co film. One may see that graphene Dirac point is located at 3 eV binding energy. After annealing of the system in an oxygen atmosphere, graphene becomes quasi-free-standing and p-doped: graphene π-states now form a Dirac cone slightly above the Fermi level (see Fig. 3.9(b)). Fig. 3.9(c) shows the SEM image of a partially intercalated system, one can see that oxygen intercalates under graphene, but at the same time it does not oxidize the Co film.

Sulfur intercalation into the graphene/Co system

After considering the possibility of how oxygen intercalates underneath graphene in the graphene/Co system, we may expect sulfur to perform similarly.

First, let us take a look at the graphene/Co system: the C1 s core level has a binding energy of ≈285 eV (Fig. 3.10(a)) and a hexagonal LEED pattern(Fig. 3.10(b). After annealing the sample in sulfur flux, C1 *s* shifts ≈1 eV toward lower binding energy, and the LEED pattern shows the appearance of a 10×10 superstructure (see Fig. 3.10(c)).

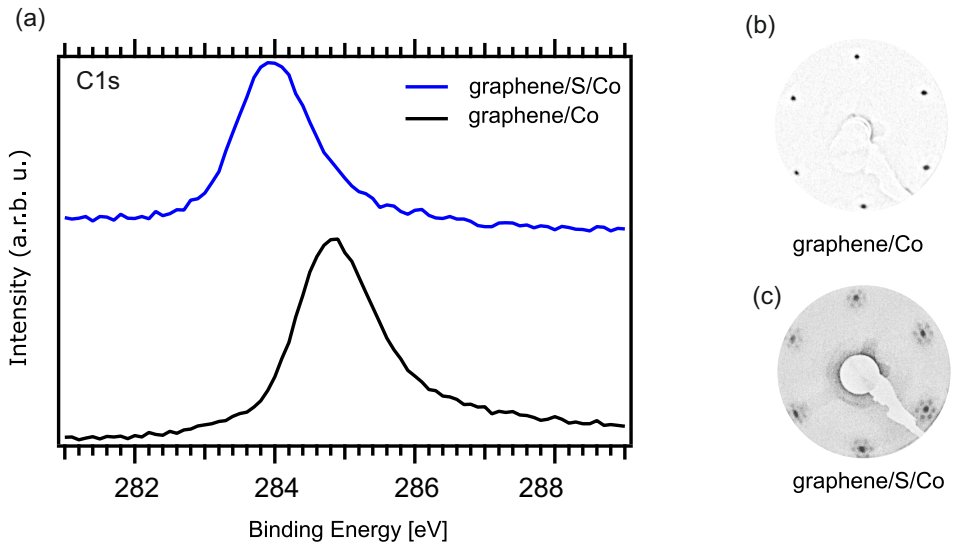

Figure 3.10: (a) XPS C1s spectra of graphene/Co (bottom) and graphene/Co annealed in sulfur flux. (b),(c) - LEED patterns of graphene/Co and graphene/Co annealed in sulfur flux, respectively. Both images were taken at 75 eV electron beam energy.

Such change may indicate that graphene was separated from the surface and became electronically quasi-free-standing, similar to the oxygen intercalation case.

Figure 3.11 demonstrates a high-resolution ARPES image of graphene/Co after annealing in sulfur flux. One can see that graphene indeed became quasi-free-standing and now features a linear dispersion of π-states near the Fermi level in the region of the $\overline{\mathrm{K}}$ point. Similar to the case of oxygen intercalation, graphene features p-doping. To draw a solid parallel between the sulfur and oxygen cases one can compare Fig. 3.11(c) and Fig. 3.9(b)

Was molybdenum intercalated into graphene/Co system?

We deposited Mo atop graphene/Co substrate for the process of MoS_2 monolayer formation on the graphene/Co substrate, then raised the sample temperature to 600°C and only then introduced the sulfur flux.

Knowing all the presented evidences, as well as those coming later in the text, we know by fact that MoS_2 monolayer was formed. However, there is an alternative to the formation of MoS_2 on the top of the graphene/Co system. One may assume that Mo atoms first intercalate underneath graphene during the process of annealing. Then while annealing the system in a sulfur flux, sulfur atoms also intercalate underneath graphene and react with Mo toms; and MoS_2 monolayer forms underneath graphene. Such concern was indeed raised by our collaborators and one of the scientists who read our paper[21] and sent us several e-mails concerning this possibility. Indeed, the

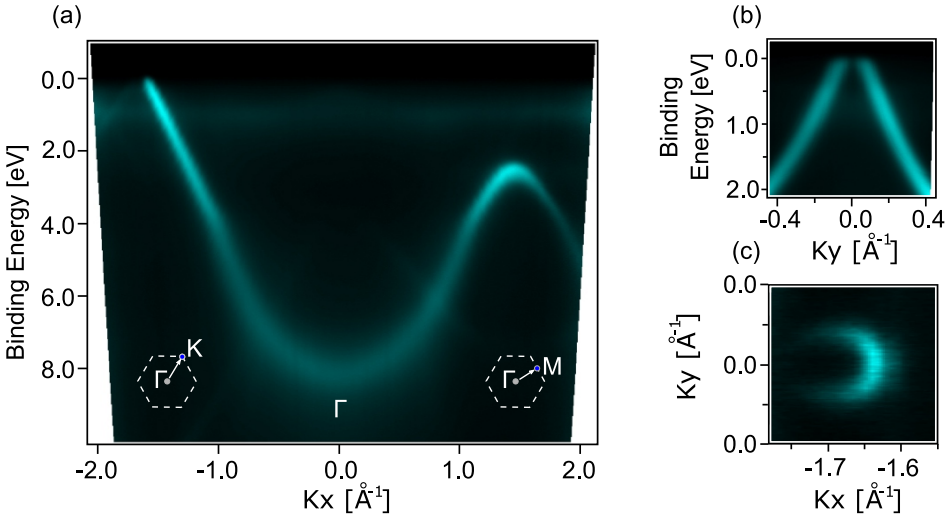

Figure 3.11: High-resolution ARPES of graphene/Co after annealing in sulfur flux along the $\overline{\text{K}}$-$\overline{\Gamma}$-$\overline{\text{M}}$ direction (a); in the region of graphene $\overline{\text{K}}$ point measured along the direction perpendicular to $\overline{\Gamma}$-$\overline{\text{K}}$(b); and Fermi surface in the region of graphene $\overline{\text{K}}$ point (c).

scientific community intercalated nearly all periodic table elements underneath graphene in graphene/substrate systems.

In order to address the above question, we may use the following techniques: measuring XPS spectra obtained under different emission angles and/or energy; using PED data as XPS data obtained under different angles; measuring STM spectra; comparing our spin and angle-resolved data with DFT simulations. However, all the mentioned techniques do not provide a 100% certainty, as we discuss below.

The basic idea of obtaining XPS measurements under different emission angles or excitation energies is to exploit the electron mean free path through the material. An increase of the emission angle leads to a longer electron path through the material. We only need to determine whether graphene is below MoS_2 or MoS_2 is below graphene. We may only pay attention to the ratio of the corresponding core level intensity distributions. If MoS_2 is below graphene, then with the increase of the off-normal emission angle, the Mo $3d$ intensity must decay, while the C $1s$ intensity must not, and vice versa.

We used this approach to determine graphene to be underneath the MoS_2 monolayer. However, such a method features a considerable margin of error, as our MoS_2 coverage is only 0.4 monolayer. Integrated PED spectra provided us with a similar result. As the mean free path depends on the electron energy, one can use an increase of the excitation energy similarly to an increase of the emission angle. Using this approach, we also determined graphene to be underneath the MoS_2 monolayer. The margin of error stays the same. Unfortunately, we could not obtain direct access to the MoS_2/graphene/Co

topography, as we could not use such methods as Transmission Electron Microscopy (TEM) due to a relatively thick W(100) substrate, which we did not want to destroy.

Our STM images (see more in 3.4.3) suggest the MoS_2 monolayer to be on the top of the system. On the other hand, we could not accurately measure the step between the region with MoS_2 and without it to prove that we are not measuring MoS_2 underneath graphene. Even though MoS_2 is highly improbably to be underneath graphene, given that the corrugation that can be seen in the MoS_2 layer, the relative location of graphene and MoS_2 remains questionable.

3.4 MoS_2/graphene/Co: system characterization

3.4.1 Evolution of the system core levels during synthesis.

Fig. 3.12(b) demonstrates C 1s, Mo 3d, and the appearing S 2s core levels before (bottom) and after (center and top) the MoS_2 growth procedure. The bottom of the C 1s spectrum represents a graphene monolayer strongly bonded to the Co substrate; we determine this bonding by observing an increased binding energy of the graphene C1 s core level (≈285 eV). The bottom of the Mo 3d spectrum represents non-structured Mo atoms deposited on the graphene/Co substrate or clusters.

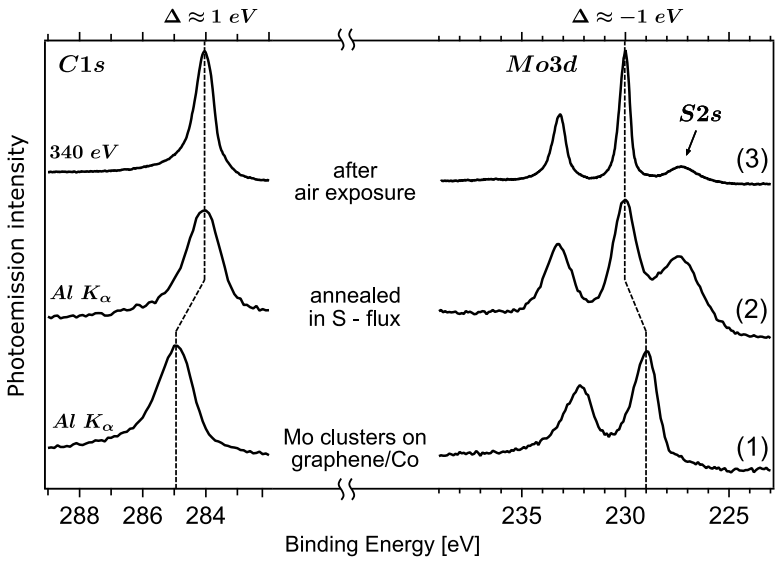

Figure 3.12: Comparison of XPS data of C 1s and Mo 3d core levels of the following systems: (1) graphene/Co system with Mo atoms deposited on the top (hν = 1486.6 eV); (2) MoS_2 monolayer formed on graphene/Co system after annealing the system in sulfur flux (hν = 1486.6 eV); (3) the same as (2) MoS_2/graphene/Co system after sample transfer to another setup and subsequent annealing at 500°C (hν = 340 eV).

After annealing the system in sulfur flux, two significant changes were observed: the C1 s core level shifted 1 eV to lower binding energy, and the Mo 3d core level shifted

1 eV to higher binding energy. We refer to the shift of the C1 s core level to graphene becoming quasi-free-standing, as sulfur intercalates underneath; and the shift of the Mo $3d$ core level to Mo being oxidized by sulfur with the formation of MoS_2. One can also observe an additional peak at around 227 eV in the center of the Mo $3d$ panel. We attribute this peak to the S $2s$ core level from the MoS_2 compound.

The measurements for the first two lines in Fig. 3.12 were obtained in the MBE (synthesis) station; while all the further measurements were obtained in other stations, in particular, we used the XPS station, the ARPES station, the spin-ARPES station, the PED station, and the STM station separately. We transferred the sample between corresponding high-vacuum chambers for each distinct measurement type. After each transfer to another chamber, we annealed the sample up to 500°C to remove adsorbates. The top in Fig.3.12 represents XPS measurements obtained in a separate chamber after sample transfer and the subsequent annealing. Both C1 s and Mo $3d$ core levels feature the same binding energy as in the center panel – the system remained the same after each transfer.

3.4.2 Symmetry of the system: LEED and PED measurements

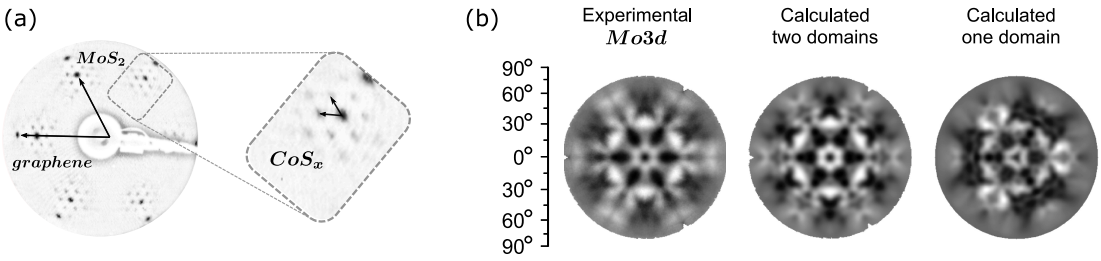

Figure 3.13: (a) LEED image of MoS_2 on graphene/Co with magnified region that represents a superstructure of CoS_x. Graphene to MoS_2 lattice parameters have a ratio $\sim$ 5:4. CoS_x seemingly features a 9×9 or 10×10 superstructure. 75 eV electron beam energy was used. (b) A comparison of experimental PED image of MoS_2/graphene/Co (left panel), simulated PED image of a single domain MoS_2/graphene (right panel), and corresponding image for two mirror domains (middle panel).

Fig. 3.13(a) demonstrates a LEED image of the MoS_2/graphene/Co system. We attribute the high sharpness of the reflexes as a high crystal quality. One can see two major structures: a bigger hexagonal pattern and a smaller one, which is surrounded by other moiré reflexes (zoomed-in). The ratio between the MoS_2 and graphene lattice parameters is around 5 to 4. The LEED image represents a picture of the reciprocal lattice; therefore, we interpret a bigger hexagon to represent graphene and a smaller hexagon to represent the MoS_2 structure. As expected, the ratio between big (graphene) and small (MoS_2) hexagon edges is $\sim$ 5:4. It is worth mentioning, that MoS_2 and graphene crystallographic axis are aligned (no rotation between the structures is detected) which suggests an epitaxial growth.

We assign the moiré pattern around a smaller hexagon to a CoS_x layer, which was formed under graphene while annealing the system in sulfur flux. We observed a similar superstructure in a LEED pattern in the sulfur intercalated graphene/Co (see Fig. 3.10(c)). One can confuse this pattern with a 9×9 or 10×10 superstructure, however, a better resolved LEED images compared with STM images suggest a sum of three types of 120° rotated domains with 2×7 or 2×8 superstructure (see more in 3.4.3 section and Figures 3.15 and 3.16).

In order to confirm that the MoS_2/graphene/Co system remained the same after each transfer and the subsequent annealing, we carried out LEED measurements and found out that the LEED images remained the same.

Fig. 3.13(a) shows that the crystallographic axis of MoS_2 are aligned along the graphene/Co system's ones. However, graphene features C_6 symmetry while the MoS_2 monolayer has only C_3 symmetry. This implies two possible orientation scenarios: the MoS_2 monolayer may be aligned with the A or B sub-lattice of graphene. In other words, two orientations of MoS_2 are possible and differ by the rotation of 180° from each other. Such domains are so-called mirror domains.

In free-standing graphene, A and B sub-lattices are equal; therefore, the MoS_2 monolayer may align with equal possibility along each sub-lattice. We can presume that we obtained not one but several domains of a MoS_2 monolayer; we can also presume that different orientations of MoS_2 crystallographic axis may coexist in different MoS_2 islands or even in one island if a domain border is formed. Thus, using graphene as a substrate for MoS_2 synthesis, one may expect an equal distribution of mirror domains formed.

In order to confirm the coexistence of two mirror domain types, we conducted PED measurements. In Fig. 3.13(b) the left image demonstrates an experimental angular PED map of the Mo $3d_{5/2}$ core level. One can see a six-fold symmetry. This suggests a coexistence of 50/50% of mirror domains.

To illustrate how the integration of PED signals from two types of MoS_2 mirror domains may result in the observed PED image, we simulated a PED pattern: Fig.3.13(b, right) demonstrates a simulated pattern from a single MoS_2 domain. In contrast, Fig. 3.13(b, middle) demonstrates a symmetrized MoS_2 pattern by applying a two-fold rotation. As a result Fig. 3.13(b, left) [the experimental PED map] and Fig. 3.13(b, middle) [the simulated PED map that is symmetrized by two-fold rotation] are in excellent agreement.

It is worth to mention, that this situation is different from the one with the MoS_2/Au(111) system, where both MoS_2 and Au(111) feature C_3 symmetry, no coexistence of mirror domains is present, and an angular PED map features three-fold symmetry. In order to correctly simulate the data, an additional two-fold rotation symmetry was not required (see section 3.2.2 and Fig.3.4).

3.4.3 Imaging the system surface: STM measurements

This section will discuss STM data that visually illustrate the micro structure of our sample.

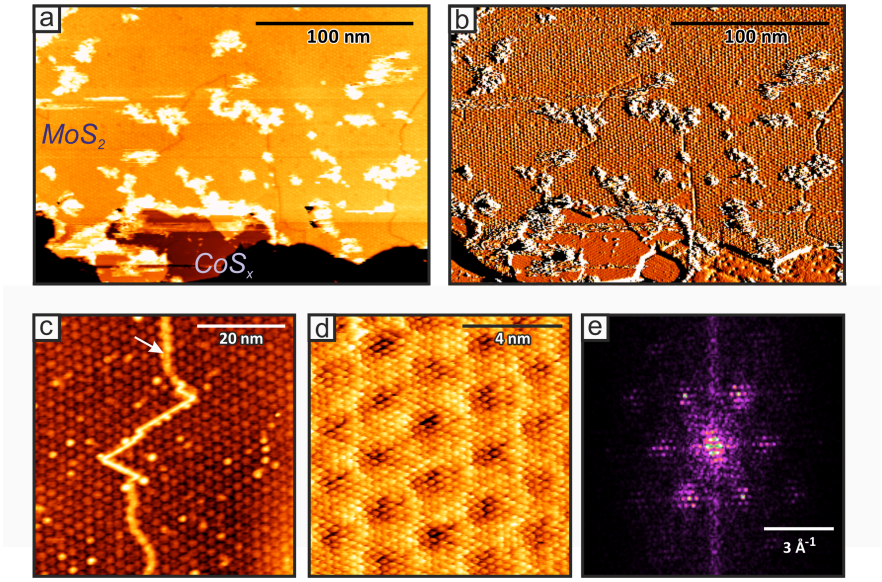

Figure 3.14: STM topography of sample areas covered with MoS_2. (a,b) Large-scale images (Z- and I- channels, respectively) show the MoS_2 domain structure and CoS_x areas covered only with graphene. (c) Large-scale image showing a characteristic moire pattern and a domain boundary (white arrow). (d,e) Atomically resolved close-up of the moiré pattern and its Fourier transform show periodicity between (7×7) and (8×8). Bias voltages and tunneling currents were: (a,b) 1V, 0.1 nA; (c) -3V, 0.5 nA; (d) -1.5 V, 0.8 nA.

Large area STM

In Fig. 3.14(a,b), one can see a large-scale STM image of the MoS_2/graphene/Co system in in I- and Z- channels respectively. We determine the topography of two types of structures: moiré structure (most of the image area) and striped superstructure (Fig. 3.14(b) bottom part). The moiré structure represents MoS_2 monolayer on the graphene, and the striped superstructure represents sulfur-intercalated graphene without MoS_2 on the top. We attribute non-periodic areas in Fig. 3.14(a,b) to some dirt, as the sample was transferred multiple times under ambient pressure.

MoS_2 domains

In Fig. 3.14(b), grain boundaries separate large-area crystalline islands of a MoS_2 monolayer with more than 200 nm size. These domains feature a moiré pattern with periodicity between 7×7 and 8×8 (relative to the MoS_2 unit cell). The MoS_2 - graphene moiré structure is formed due to a lattice mismatch between MoS_2 and graphene: four unit

cells of MoS_2 almost match with five unit cells of graphene. Fig. 3.14(d) provides an atomic resolution of this moiré structure. In Fig. 3.14(e), we show a Fourier transform of this structure, which agrees well with the LEED images discussed above.

One can see that MoS_2 forms different domains; presumably, some of them are mirror domains. The domain wall is well resolved in Fig. 3.14(c).

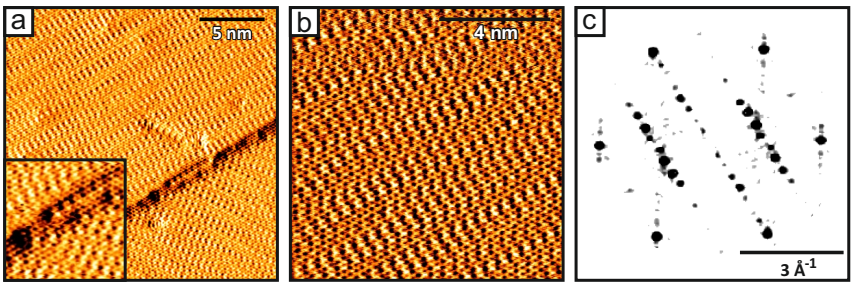

Figure 3.15: STM topography of sample areas without MoS_2 covered only with graphene (I- channel). (a) The border between two terraces with striped patterns aligned at 120° relative to each other. Inset: zoom-in of the border region with a hexagonal lattice covering both terraces. (b) High-resolution close-up of the superstructure pattern, and (c) its Fourier transform similar to a LEED pattern of Gr/CoS_x. Bias voltages and tunneling currents were: a) -1.5 V, 0.3 nA; b) -1.5 V; 0.2 nA.

CoS_x stripped superstructure

In Fig. 3.14(a,b), one can see the area of graphene on CoS_x without a MoS_2 monolayer on the top. The area features linear superstructure patterns. These linear patterns coexist in three orientations that are rotated by 120° to each other. In a closer look at the inset of Fig. 3.15(a), one can see that the top layer features a hexagonal lattice that continuously extends from one terrace to another despite different orientations of linear superstructures of the terraces. We attribute this continuous hexagonal structure to a graphene monolayer because of two reasons: First, graphene is well known to behave this way – to cover atomic terraces as a carpet [130]. Second, a Fourier analysis presented in Fig. 3.15(c) suggests a hexagonal structure corresponding to graphene parameters. In Fig. 3.15(c) one can also see something between (2×7) and (2×8) patterns, which we attribute to a CoS_x superstructure.

Let us compare a Fourier transform of an STM image of CoS_x areas to a LEED pattern of graphene/S/Co. In order to do so, we need to aggregate three patterns of 120° rotated CoS_x striped domains in one image: Fig. 3.16(a) demonstrates the CoS_x striped pattern, Fig. 3.16(b) demonstrates its Fourier transform, and Fig. 3.16(c) demonstrates three-fold symmetrization of Fig. 3.16(b). Now we can compare Fig. 3.16(c) and Fig. 3.16(d) – they look quite similar. Both feature moiré structures and star-like patterns.

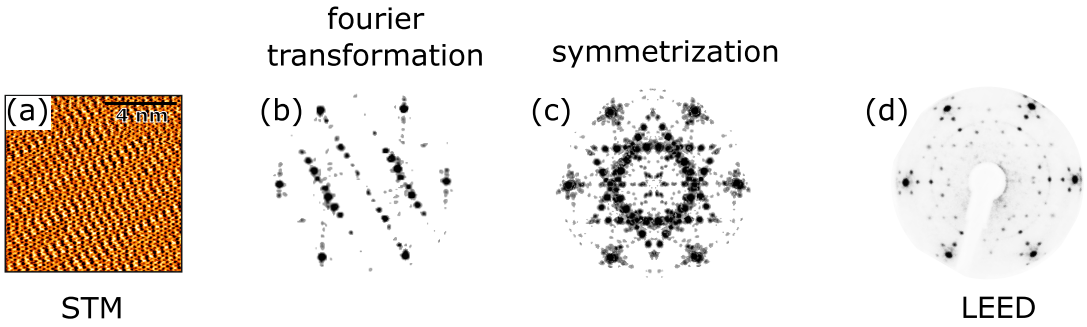

Figure 3.16: Correspondence of STM and LEED data of the graphene/S/Co system. (a) - STM image of graphene/S/Co: graphene atop CoS_x. (b) - a Fourier transformation of STM image (a). (c) - summarized (b). (d) - LEED image of graphene/S/Co system.

3.4.4 Defects and lattice mismatch

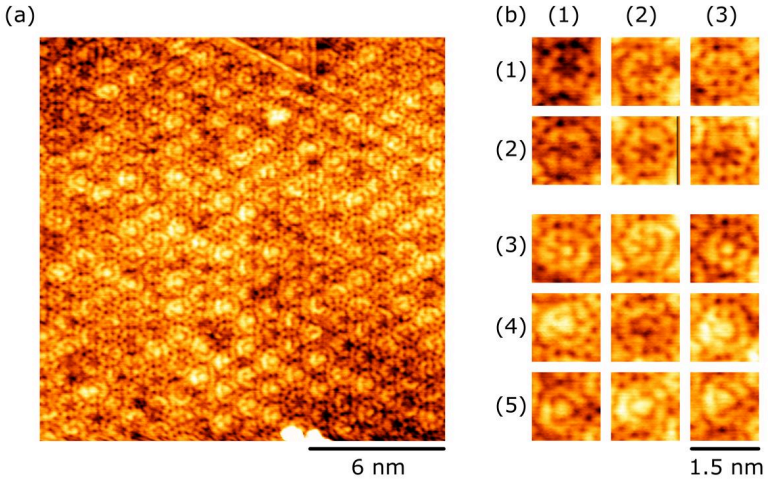

Figure 3.17: STM image of MoS_2/graphene/Co system: visualisation of moiré supercell in MoS_2 structure. (a) - STM image of moiré pattern in MoS_2. (b) - different types of moiré supercell. Bias voltages and tunneling currents were: -1 V, 0.1 nA.

In the Fig. 3.17(a) one can see a complex pattern of MoS_2 moiré supercell. Besides a small part of a domain wall on the top, the image represents a single domain of MoS_2. Interestingly, this single domain demonstrates several types of sub-units of quasi-periodic moiré pattern presented in the lines (1-5) in Fig. 3.17(b). To our knowledge, locations of different types of sub-units do not follow a pattern but rather appear randomly to compensate for MoS_2/graphene lattice strains. The coexistence of several types of sub-units suggests that the mismatch of MoS_2/graphene is not exactly 4 to 5 but non-periodic and requires additional relaxation mechanisms.

We have tried to simulate and explain different types of sub-units of the quasi-periodic moiré patterns. However, we have not yet succeeded – it seems to be a complex

and exciting separate research topic that would require more experimental STM studies and a series of STM simulations. We want to highlight the most surprising supercell type presented in lines (2) and (4) – a pentagonal supercell. For now, we cannot explain the appearance of such symmetry.

Summary of the chapter 3

First, we used the MBE technique to synthesize the MoS_2 monolayer on an Au(111) single crystal. We obtained ≈0.4 coverage without so-called mirror domains. The MoS_2 monolayer perfectly fits to the Au(111) surface forming a 10×10 superstructure. The MoS_2 islands are equally distributed on the Au(111) surface and have similar triangular shapes and orientations. The average domain size is 30 nm.

After finding the parameters for MoS_2/Au(111) synthesis, we applied and modified them for MoS_2 synthesis on the graphene/Co substrate. Similar to the case of the Au(111) substrate, we only formed ≈0.4 MoS_2 monolayer coverage. Unlike on the Au(111) substrate, the formation of the MoS_2 monolayer on graphene/Co takes place quickly and simultaneously without intermediate steps. We ascribe this difference to the stronger chemical bonding of molybdenum atoms to the gold substrate than to the graphene one. Graphene and MoS_2 feature a 4 to 5 ratio of unit cells which corresponds to the observed 5×5 superstructure.

Interestingly, an additional 9×9 or 10×10 superstructure is observed. We assign it to a CoS_x layer underneath graphene. During sample annealing in sulfur flux, the sulfur does not only oxidize molybdenum atoms to form MoS_2 but also intercalates underneath graphene and makes it quasi-free-standing. Atomic resolution imaging clarifies that the superstructure is a coexistence of three 120° rotated 2×7 or 2×8 domain superstructures.

Another difference between the MoS_2 coverage on graphene/Co from the one on Au(111) is that on graphene/Co mirror domains are equally present. We conclude that graphene features six-fold symmetry and epitaxial growth of MoS_2 monolayer can correspond to **A** or **B** graphene sublattices with equal probability.

We observed large area crystalline islands with an average size of more than 200 nm. These islands consist of several domains connected through domain walls. We believe that the domain wall connects mirror domains. An atomic resolution imaging of MoS_2 monolayer domains demonstrates a rather quasi-periodic structure with several types of sub-units of moiré patterns. It suggests an incommensurate lattice mismatch and the presence of structural defects to compensate for it.

This page was intentionally left empty.

Chapter 4

Electronic and spin structure

4.1 Analysis of the MoS_2/Au(111) system

Spin properties of a MoS_2 monolayer synthesized on Au(111) have already been investigated[55]. These studies were focused on the out-of-plane spin structure of the original MoS_2 monolayer. On the contrary, we are interested in the in-plane spin structure which is a result of the interaction between the MoS_2 band structure and the gold substrate.

In this section we aim to confirm that the MoS_2 band structure is able to develop certain in-plane spin properties due to the interaction with the substrate.

4.1.1 MoS_2/Au(111) band structure: ARPES measurements

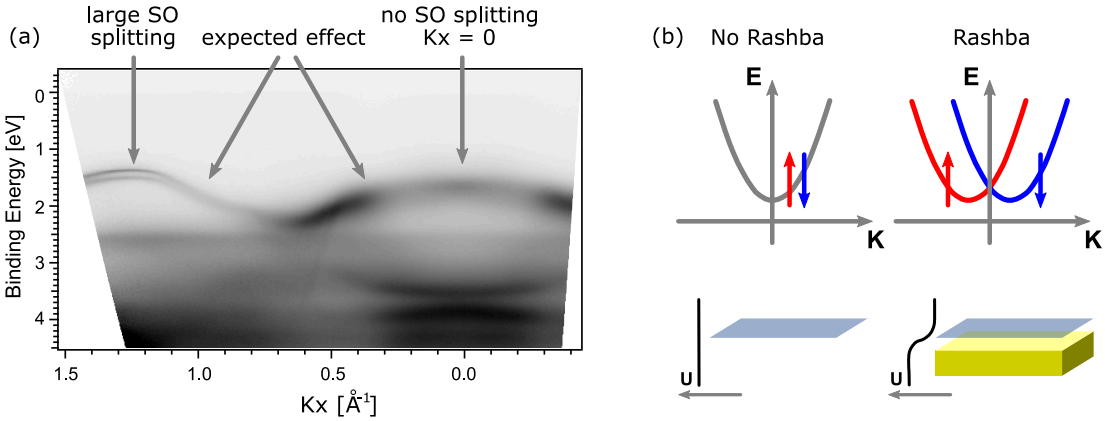

Figure 4.1: (a) - A high-resolution ARPES dispersion of MoS_2/Au(111). The data were acquired along the $\overline{\Gamma}$-$\overline{K}$ direction. The photon energy was 20 eV. (b) - a schematic representation of the Rashba effect in the presence of a surface potential gradient. The top-left inset represents the electronic state of 2D electron gas with parabolic dispersion, while the top-right inset represents a Rasba spin-split 2D electron gas state in the presence of potential gradient from the substrate.

Fig. 4.1(a) displays the MoS_2 experimental electronic band structure measured by ARPES. The MoS_2 valence band state is located in the binding energy range between

1.4 eV and 2.3 eV. One can see an outstanding resolution and image contrast that suggests a high quality of the synthesized sample.

Let us first confirm that we observe a monolayer MoS_2 which is not a bi-layer or bulk material. In a few-layer MoS_2 stack, the valence-band maximum is located at the $\overline{\Gamma}$ point[56, 131, 132], while in a single layer it is at $\overline{K}$. From the position of the valence band maximum of our system at the $\overline{K}$ point, we can determine that the obtained MoS_2/Au(111) system features a monolayer MoS_2 (the top band at $\overline{K}$ is at 1.38 eV, while the top band at $\overline{\Gamma}$ is at 1.62 eV).

The top valence band state at $\overline{K}$ of a free-standing MoS_2 monolayer is spin-split. The energy splitting is due to a spin splitting in the out-of-plane direction and originates from spin-orbit interaction. Our MoS_2/Au(111) system also features a similar splitting. We have resolved its value as 140 meV, which is consistent with previously reported experimentally obtained values for MoS_2 monolayers[56, 131].

Interestingly, in Fig. 4.1(a) we do not observe any gold surface states. We attribute this fact to a not completely clean Au(111) surface after its transfer to another high-vacuum chamber (one should remember that the MoS_2/Au(111) sample does not feature a complete MoS_2 coverage). We know that a higher annealing temperature would result in the reappearance of gold surface states, as we witnessed several times while conducting similar measurements (see e.g. Fig. 4.4(a)) We decided to keep this image, as it shows MoS_2 valence band electronic states with even a better contrast without intensity from gold surface states.

4.1.2 Dresselhaus and Rashba effects

The idea behind the manipulation of the MoS_2 spin structure via a gold substrate is to use symmetry breaking. The free standing MoS_2 monolayer features a spacial symmetry in the out-of-plane (z) direction, while the MoS_2 monolayer on a substrate does not. The MoS_2 on a substrate faces the substrate and interacts with it in one z-orientation and faces vacuum and has no interaction in another.

Spin-Orbit interaction

In the framework of classical physics, we know that a charged particle experiences the Lorentz force when moving in a magnetic field. On the other hand, we know that an accelerated charged particle generates a magnetic field. Let us consider an electron that moves in the central potential of the atomic nucleus: it moves in a curved orbit, in other words it moves with acceleration. Therefore, the electron has an internal magnetic moment (spin) and generates a magnetic moment as it moves in the central potential of the atomic nucleus. This allows us to imagine that the spins (magnetic moments) and orbits (moments of momentum) of electrons will interact with each other, and the

larger they are – the greater the interaction will be. The Hamilton of this interaction is written as follows:

$$\hat{H}_{SO} = \frac{Ze^2}{2m^2c^2r^3}(\hat{\boldsymbol{S}} \times \hat{\boldsymbol{L}}), \tag{4.1}$$

where $\hat{H}_{SO}$ – spin-orbit coupling operator, $\hat{\boldsymbol{S}}$ – spin momentum operator, and $\hat{\boldsymbol{L}}$ – angular momentum operator. The expression can be obtained both in the classical approximation as well as in the approach of relativistic quantum mechanics.

Bloch's theorem

Bloch's theorem determines the form of the wave function of a quantum particle, which propagates in a periodic potential $U(\vec{r})$.

$$\hat{H} = -\frac{\hbar^2}{2m}\nabla^2 + U(\vec{r})$$

$U(\vec{r})$ is periodic in all vectors $\vec{R}$ that belong to the Bravais lattice.

The eigenstates of such a Hamiltonian can be chosen to be in a form of a plane wave multiplied by the Bravais periodic function (with a similar periodicity as $U(\vec{r})$).

$$\Psi_{n\vec{k}} = e^{i\vec{k}\vec{r}}u_{n\vec{k}}(\vec{r}), \tag{4.2}$$

where $u_{n\vec{k}}(\vec{r} + \vec{R}) = u_{n\vec{k}}(\vec{r})$

Symmetry breaking

Let us consider how spin-orbit interaction can influence an electron band structure[133]. The spin-orbit interaction depends on $\vec{k}$ and together with crystal fields is able to split electronic states featuring different symmetries.

The Kramers (degeneracy) theorem states that in a system with half-integer spin (electronic states follow this condition) and a Hamiltonian that is invariant under reversal of the time direction, any state is at least doubly degenerate[134].

$$T : t \to -t \quad \Rightarrow \quad [\hat{H}, \hat{H}] = 0,$$

where $\hat{H}$ - time-reversal operator

In our case, time-reversal symmetry requires the absence of an external magnetic field or ferromagnetism. It is expressed as follows:

$$E(\vec{k}, \uparrow) = E(-\vec{k}, \downarrow) \tag{4.3}$$

In the case a crystal structure has a momentum inversion, then

$$u_{-\vec{k}}(\vec{r}) = u_{\vec{k}}(-\vec{r}) \tag{4.4}$$

In the case of the Bloch function, the spin structure is completely degenerate.

Dresselhaus effect

In the case of systems that lack some of the symmetries, states with different spins can be spin-split in energy. Such reasoning was firstly modeled by Gene Dresselhaus and discovered by his wife Mildred Dresselhaus[135, 136] They considered systems that lack momentum reversal symmetry for non-centrosymmetric crystals, such as Zinc Blende (ZnS) crystals. They proposed the following Hamiltonian:

$$H_D = D\Phi_D \cdot \vec{\sigma}, \tag{4.5}$$

where D is a constant, $\vec{\sigma}$ – a vector consisting of Pauli matrices σ_x, σ_y, σ_z, and

$$\Phi_D = (k_x(k_y^2 - k_z^2),\ k_y(k_z^2 - k_x^2),\ k_z(k_x^2 - k_y^2))$$

For the case in 2D, the Hamiltonian looks as follows:

$$H_D^{2D} = \beta(\sigma_x k_x - \sigma_y k_y) \tag{4.6}$$

For ease of understanding, we can imagine it as potential with a periodic system of gradients in the considered plane. The expression above leads to the quadrupole spin splitting (see Fig. 4.2(a))

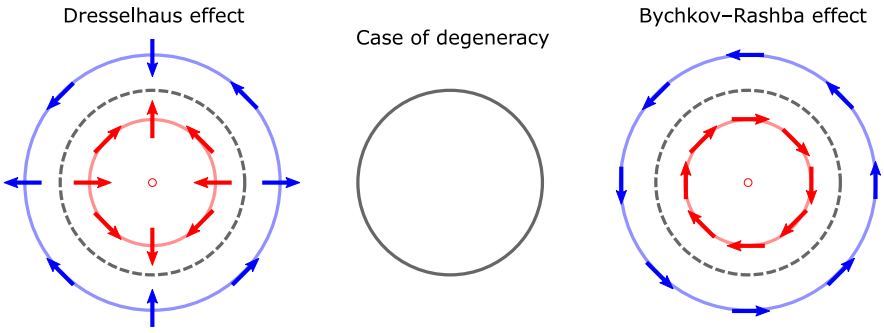

Figure 4.2: Schematic representation of Fermi surfaces and spin structure for the cases of Dresselhaus and Rashba effects

Rashba effect

Such a theoretical model was described by Emmanuel Rashba and Yuri Bychkov [9, 137, 138]. Some scientists, especially from Post-Soviet Space, prefer to call this effect the Bychkov-Rashba effect.

This effect is similar to the Dresselhaus effect but comes from different symmetry-breaking conditions. Here the symmetry breaking happens in a direction perpendicular to the plane of the 2D system. It is easy to imagine it as a potential gradient in the direction perpendicular to the plane of the system. Rashba effect is potentially easier

to observe than Dresselhaus effect, as the condition for Rashba effect is satisfied for any surface state: in one z-direction, the states experience potential gradients from the atoms, while in the other, there is vacuum.

One can formulate the following Hamiltonian related to such potential:

$$H_R = \alpha(\vec{\sigma} \times \vec{k}) \cdot \vec{v}, \tag{4.7}$$

where $\vec{v}$ – a unit vector that points to a high symmetry ax of the crystal. In the 2D case (e.g., surface states), $\vec{v}$ is an out-of-plane unit vector, and the Hamiltonian can be simplified to the following expression:

$$H_R^{2D} = \alpha(\sigma_x k_y - \sigma_y k_x) \tag{4.8}$$

When one plugs the Hamiltonian above into the Schrodinger equation, the eigenvalues for a two-dimensional free electron gas will be as follows:

$$E_{\pm}(\vec{k}) = \frac{\hbar^2 k^2}{2m^*} \pm \alpha k, \tag{4.9}$$

where $k = |\vec{k}|$, and m^* – an effective mass.

This corresponds to free-electron parabolic energy-momentum dispersions, which are split in the $\vec{k}$ direction. It is worth noting that in surface states, the magnitude of the splitting can be tuned by varying the nuclear potential gradient at a surface of a crystal. For instance, in crystals that consist of atoms with a high atomic number, the gradient is larger than in ones that consist of atoms with a relatively low atomic number. Gold atoms are the heavy ones, and the crystal potential gradient at Au(111) surface is large.

Rashba effect in MoS_2 band structure: expectations

Let us consider the MoS_2/Au(111) system. The above discussion about the influence of the potential gradient on 2D electronic states can be applied to MoS_2 monolayer electronic states that are located in the proximity of the potential gradient of the gold crystal.

In the Fig. 4.1(b) one can recognize energy-momentum dispersion of 2D electronic gas. On the left side, the states are degenerate, while on the right, the spin splitting in momentum space is illustrated. In contrast to the left side, 2D electron gas on the right side is placed close to the potential gradient, as it is shown in the lower illustration. The potential gradient is generated by the proximity of a crystal surface.

For ease of understanding, one can relate 2D electronic states of the MoS_2 monolayer to the electronic states of the 2D electron gas and the proximity to the Au(111) crystal surface to the potential gradient formed by the crystal surface.

Let us consider what we should expect from the influence of the Au(111) crystal surface on the MoS_2 monolayer band structure in Fig. 4.1(a). The Rashba effect is supposed to be linear in $\vec{k}$ (see equation 4.9)), and as illustrated in Fig. 4.1(b) the splitting at $\vec{k} = 0$ (in other words in the region of the $\overline{\Gamma}$ point) is expected to be zero.

Next, let us take a look at the $\overline{K}$ point. The Rashba effect is supposed to be maximum; however, there is another conflicting argument: symmetry. The symmetry suggests the reversal of the sign of the Rashba effect at $\overline{K}$. On the other hand, the intrinsic spin-orbit interaction lifts the spin degeneracy in the out-of-plane direction. The intrinsic spin-orbit interaction in the region of $\overline{K}$ causes the MoS_2 valence band state in the region of 1.5 eV binding energy to spin split. We observe this splitting in Fig. 4.1(a) in the region of $\overline{K}$.

As shown in Fig. 4.1(a), in the valence band structure of MoS_2 we expect zero manifestation of a Rashba effect in the regions of $\overline{\Gamma}$ and $\overline{K}$ points, while we expect some of it in other regions with $\vec{k} \neq 0$.

4.1.3 MoS_2/Au(111): DFT computations

In order to visualize and crosscheck our bold assumption about the possibility of a Rashba effect in the MoS_2/Au(111), we performed a simplified DFT calculation. The word "simplified" means that we have not simulated a 10×10 superstructure but used 1×1 and included only four layers of Au atoms.

In order to obtain a relatively complete picture of the MoS_2 monolayer spin structure in the MoS_2/Au(111) system, we simulated a spin-resolved ARPES-like map of the MoS_2 Brillouin zone for all three spin projections: S_x, S_y, and S_z (see Fig. 4.3). In the MoS_2 Brillouin zone the coordinates S_x corresponds to a spin projection along the in-plane $\overline{\Gamma}$-$\overline{M}$ direction, S_y along $\overline{\Gamma}$-$\overline{K}$, and S_z along the out-of-plane direction.

Let us first get grounded to a familiar MoS_2 out-of-plane spin structure in Fig. 4.3(e,f). In the region of $\overline{K}$, one can see spin-split states in the out-of-plane direction. In Fig. 4.3(f) it is easy to recognise how the top-valence band electronic states reverse its spin in neighbouring $\overline{K}$ points (one can determine them as $\overline{K}$ and $\overline{K'}$ points). Such a feature secures the absence of MoS_2 ferromagnetic behavior.

Let us turn to the in-plane spin structure of the MoS_2. In our previous considerations, we assumed that there would be no in-plane Rashba-related lifting of spin degeneracy in the regions of $\overline{\Gamma}$ and $\overline{K}$ points. Looking at both Fig. 4.3(a,b) and (c,d) one can observe zero in-plane spin polarisation in the region of $\overline{K}$. That satisfies the MoS_2 symmetry criteria at the high symmetry $\overline{K}$ point: the spin polarisation effect must be opposite for $\overline{K}$ and $\overline{K'}$, and what is a $\overline{K}$ point for the first Brillouin zone is the $\overline{K'}$ point for the second one. Thus, the effect must be zero at $\overline{K}$.

The $\overline{\Gamma}$ point seems more complex for the evaluation by the DFT computation, as it includes lots of gold surface states. We used 4 layers of Au atoms in the presented model,

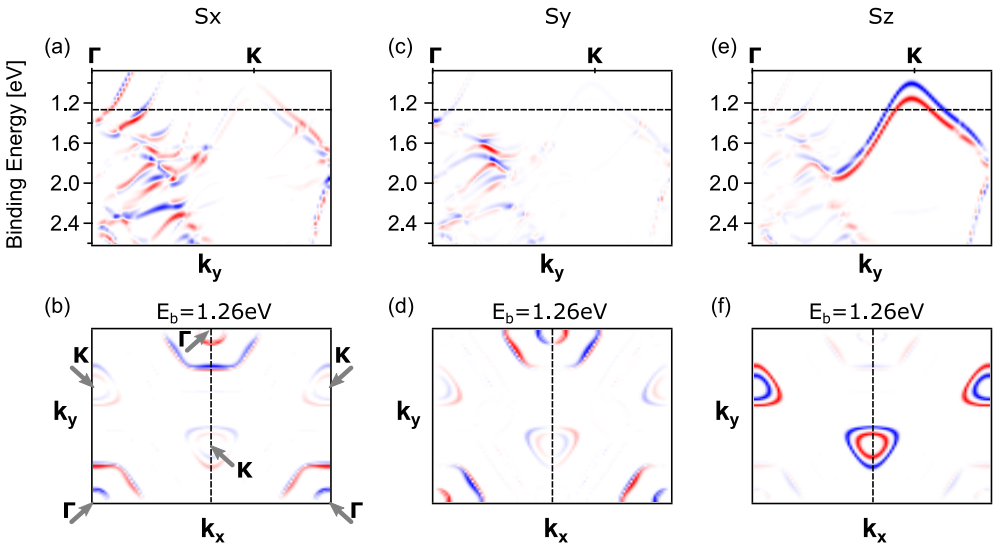

Figure 4.3: Simulated spin-resolved ARPES-like map of MoS_2/Au(111) in S_x (a,b), S_y (c,d), and S_z (e,f) spin projection directions. In MoS_2 Brillouin zone coordinates, S_x refers to the in-plane $\overline{\Gamma}$-$\overline{M}$ direction, S_y to $\overline{\Gamma}$-$\overline{K}$ and S_z to the out-of-plane direction. (a,c,e) images represent $\overline{\Gamma}$-$\overline{K}$ slice of MoS_2 Brillouin zone, while (b,d,f) represent constant energy slice (E_b=1.26 eV) of the map of electronic states of MoS_2, so one can recognise the regions near MoS_2 $\overline{\Gamma}$ and $\overline{K}$ points. Red–blue color coding represents opposite spin directions in each image.

which brings additional parabolic gold surface states (artifacts). In Fig. 4.3(a,c,e) one can see four parabolic states.

One can observe a hybridization between MoS_2 valence band states and each parabolic gold state. Here we conclude that the MoS_2 monolayer electronic structure is expected to hybridize with gold bulk states. This conclusion is consistent with our previous ARPES observations: in Fig. 4.1(a) in the region between $\overline{\Gamma}$ and k_x=0.65 MoS_2 valence band states seem to be more intense and energetically wide-spread as if they were hybridized with gold bulk states.

The comparison of Fig. 4.3(a,b) and (c,d) also provides us with a conclusion relevant for spin-measurements. As we are interested in an investigation of spin properties in a high symmetry direction such as presented in Fig. 4.3(a,c,e) $\overline{\Gamma}$-$\overline{K}$ direction, in Fig. 4.3(d) one can see that in S_y one must expect a negligible non-trivial in-plane spin signature. Note that we slightly shifted the $\overline{\Gamma}$-$\overline{K}$ cut from this direction to produce Fig. 4.3(c); otherwise, it would result in an empty graph. Therefore, we will later focus on spin-resolved measurements in the S_x spin projection.

Manifestation of Rashba effect To sum up, in Fig. 4.3, we can observe a non-trivial in-plane spin structure that is not present in the free-standing MoS_2 monolayer. In the region close to the $\overline{K}$ point, the in-plane Rashba effect is negligible, as it is overruled by

the intrinsic MoS_2 spin-orbit interaction. Let us, however, pay attention to the region around $\overline{K}$ of MoS_2 (see Fig. 4.3(b,d,f)). Most of the spin polarisation still lies in the out-of-plane direction (see Fig. 4.3(f)), while some part of it rotates in the in-plane direction. Aggregating Fig. 4.3(b) and (d), keeping in mind that red and blue colors represent opposite spin directions, one can see a Rashba-like precession around the $\overline{K}$ point, which looks exactly like the schematic representation in Fig. 4.2 on the right side.

4.1.4 Spin-resolved measurements of MoS_2/Au(111)

After making bold assumptions about the possibility of a Rashba effect for MoS_2/Au(111) and crosschecking them by DFT calculations, we performed time-consuming spin-resolved measurements for dots along the $\overline{\Gamma}$-$\overline{K}$ direction of the MoS_2 Brillouin zone. Following conclusions of DFT simulations we performed spin-resolved measurements for S_x (in-plane, along $\overline{\Gamma}$-$\overline{M}$) and S_z (out-of-plane) directions.

Before the spin-resolved study, we obtained an ARPES map of the MoS_2 monolayer Brillouin zone. Fig. 4.4(a) represents a slice of this map in the $\overline{\Gamma}$-$\overline{K}$ direction. Fig. 4.4(a) is supposed to be similar to Fig. 4.1(a), however in Fig. 4.4(a) besides the MoS_2 monolayer valence band, two gold states feature a significant intensity. One is a gold surface state in the region of $\overline{\Gamma}$, and another crosses the MoS_2 valence band at K_x=0.8Å^{-1}. We attribute this difference to proper annealing of the system before spin-resolved measurements, which has not happened prior to the ARPES measurements presented in Fig. 4.1(a).

Fig. 4.4(a) is a slice from a polar angle map, K_x values were calculated from polar angles and kinetic energies. Knowing the corresponding to MoS_2 band structure polar angles of the sample, we chose particular angles to measure time-consuming spin-resolved spectra.

Green-dashed lines in Fig. 4.4(a) correspond to spin-resolved spectra taken at the corresponding spots of the MoS_2 monolayer Brillouin zone. Spin-resolved spectra are taken at particular polar angle positions; therefore, they cannot precisely correspond to the particular K_x values but instead can be visualized as spin-resolved slices along $E(K_x)$ parabolas in Fig. 4.4(a).

Let us look at the experimentally obtained MoS_2/Au(111) spin structure. Fig. 4.4(b-g) and (b'-g') represent in-plane and out-of-plane spin-resolved measurements at different K_x. We refer spin-resolved spectra taken at a particular polar angle to a particular K_x by a corresponding K-position of the MoS_2 monolayer valence band states.

Looking at Fig. 4.4(b'-d') one can see that MoS_2 monolayer valence band states in the region of $\overline{K}$ are almost 100% out-of-plane spin polarised. At the exact position of the $\overline{K}$ point the in-plane polarisation is negligible (see Fig. 4.4(c)), while in the region of $\overline{K}$ the in-plane polarisation becomes somewhat pronounced (see Fig. 4.4(b,d)). In Fig. 4.4(e,f,g) one can observe how the Rashba effect manifests itself in the MoS_2 valence

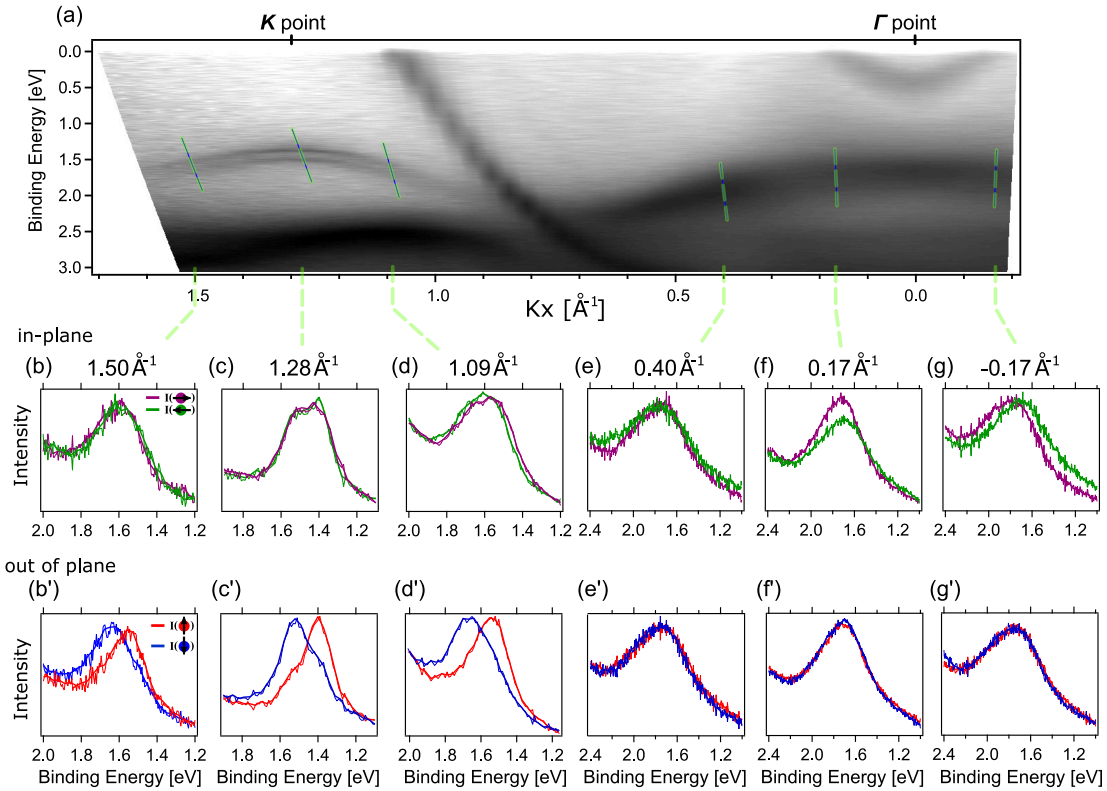

Figure 4.4: Spin-resolved photoemission measurements of MoS_2/Au(111) valence band electronic structure along $\overline{\Gamma}$-$\overline{K}$ direction of the MoS_2 monolayer Brillouin zone. (a) – the representation of the ARPES measurements performed for calibration and visualization of spin-resolved measurements. It is taken during the same experiment at the same photon energy as for spin-resolved measurements. (b-g) and (b'-g') are spin resolved PES spectra in in-plane S_x ($\overline{\Gamma}$-$\overline{M}$) and out-of-plane S_z directions performed at different K_x values. Green–purple color coding represents opposite spins in the in-plane direction, while red–blue represents opposite spins in the out-of-plane direction. The photon energy was 20 eV.

band spin structure: taken at positive K value Fig. 4.4(e) shows the spin-left in-plane spin spectrum to feature a higher binding energy than the spin-right one, while taken at the negative K value Fig. 4.4(g) shows it is opposite.

Appendix to 4.1.4: MoS_2/Au(111) spin-resolved data evaluation

Since, unlike in the MoS_2/graphene/Co system, we could not swap a magnetic field and make a proper normalization procedure for each spectrum, we used the following approach.

Let us only consider the out-of-plane spin direction (for the in-plane case, the consideration is the same.) Let us name two electron detectors that suppose to record electrons with opposite spin as "Left" and "Right," respecting their geometrical location inside the Mott detector. Therefore recorded intensities from those detectors are I_L and I_R.

The asymmetry is defined as:

$$A = \frac{I_L - I_R}{I_L + I_R}$$

As the Mott detector does not feature a 100% efficiency, we must introduce a Sherman function that would compensate for that. Each Mott detector features a particular Sherman function which must be measured in advance (we have S=0.16). Polarization is defined as:

$$P = \frac{A}{S}$$

By definition, polarization is:

$$P = \frac{N_\uparrow - N_\downarrow}{N_\uparrow + N_\downarrow} = \frac{I_\uparrow - I_\downarrow}{I_\uparrow + I_\downarrow},$$

where $N_\uparrow$ and $N_\downarrow$ are the numbers of electrons with spin-up and spin-down corresponding eigenstates. $I_\uparrow$ and $I_\downarrow$ are the corresponding intensities.

Finally, the intensities we demonstrate in Fig. 4.4 are defined as follows:

$$I_\uparrow = \frac{1+P}{2} I_{tot} \quad \text{and} \quad I_\downarrow = \frac{1-P}{2} I_{tot},$$

where $I_{tot} = I_\uparrow + I_\downarrow$.

4.2 MoS_2/graphene/Co: analysis of the system

We will present this section most straightforwardly, as the investigation of electronic and spin properties of MoS_2/graphene/Co system is the main focus of the present thesis.

4.2.1 MoS_2/graphene/Co band structure: ARPES measurements

Let us look at the valence band electronic structure of MoS_2 in the MoS_2/graphene/Co system. Figures 4.5 displays an energy-momentum dispersion measured by ARPES. We assembled the picture at the middle bottom by stitching the raw data at different tilt and azimuth angles. The stitching process from the raw data is represented in Fig. 4.5. In order to clarify the areas of the Brillouin Zone where the raw data were taken, we added partially transparent insets. To understand the particular methodology of how we measured those specific areas, one can take a look at Fig. 4.6.

In Fig. 4.5 the intense band with a minimum at a BE of ≈8eV at $\overline{\Gamma}$ and linear dispersion near the Fermi level corresponds to graphene π states, which evidence that graphene in the MoS_2/graphene/Co system is quasi-free-standing. In section 3.3.3, we demonstrated that annealing of the graphene/Co system leads to graphene becoming quasi-free-standing via S-intercalation. Given the above, it would be more appropriate to name our system MoS_2/graphene/CoS_x/Co. However, it would also be confusing,

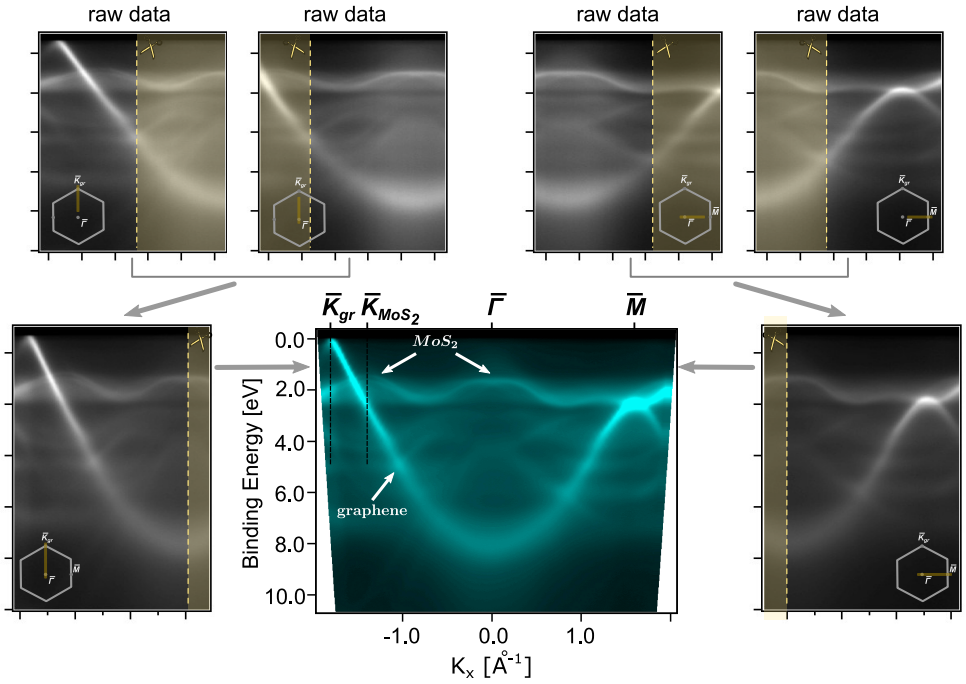

Figure 4.5: High-resolution ARPES dispersion of MoS_2/graphene/Co along the $\overline{K}$-$\overline{\Gamma}$-$\overline{M}$ direction. The main (middle-bottom) picture is stitched from four data sets acquired at different tilts and angles. Measured at 60 eV photon energy.

as in this manuscript, we mainly focus on electronic and spin properties of MoS_2 and how they may depend on the interaction with the magnetic Co layer. Later we will also consider a supercell model for DFT calculations, which ignores the intercalated sulfur due to limitations of computational resources (see more in section 4.2.4). Therefore here, before and later, we will use the name MoS_2/graphene/Co system meaning MoS_2 monolayer on quasi-free-standing graphene on thin layer Co intercalated by sulfur.

The band dispersing in the BE range of 1.5 to 2.5 eV in Fig. 4.5 belongs to the top of the MoS_2 valence-band states. The energy position of the MoS_2 valence band suggests that the MoS_2 monolayer is quasi-free-standing. Similar to the MoS_2/graphene/Ir(111) system [56], where the interaction between MoS_2 and the graphene/Ir substrate was reported to be weak, we do not observe any detectable avoided crossing effects (hybridization) between MoS_2 and graphene or Co states. Similar to free-standing MoS_2 monolayer, the valence-band maximum of MoS_2 on the graphene/Co substrate is located at ~ 1.46 eV BE.

So far we did not have solid evidence that the MoS_2 is a monolayer: XPS data only suggest that Mo atoms were oxidized by sulfur (see section 3.4.1 and Fig. 3.12); LEED and PED data provided C6 symmetry of the Mo and sulfur-containing structure. ARPES data, on the contrary, can tell the difference between MoS_2 monolayer, bilayer, multilayer, and bulk. The MoS_2 valence band structure depends on the number

of layers: in a few-layer stack, the valence-band maximum is located at $\overline{\Gamma}$ [56, 131, 132], while in a single layer at $\overline{\mathrm{K}}$. ARPES data presented in Fig. 4.5 show that the valence-band maximum is located at $\overline{\mathrm{K}}$, proving that the MoS_2 film has a monolayer thickness.

Interestingly, a few-layer stack manifests itself with quantum well states at the $\overline{\Gamma}$ point, where the number of states represents the number of layers [139]. If we had a two or three-layer stack, we would be able to resolve those states in ARPES measurements. A closer look at the MoS_2 band structure at $\overline{\Gamma}$ point reveals only one state proving only one monolayer is present, as we have already shown above. On the other hand, the presence of a low-intensity ARPES signal a bit above the MoS_2 valence-band maximum in the region of $\overline{\Gamma}$ suggests the presence of an insignificant amount of multilayer MoS_2.

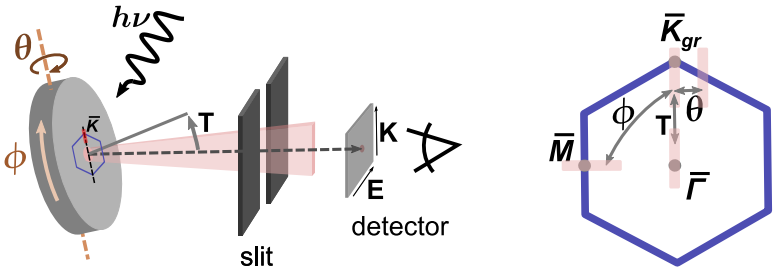

Figure 4.6: Scheme of measuring ARPES in different k-directions in our setup. The left part represents how the sample is oriented relative to the synchrotron beam ($h\nu$) and analyzer slit, followed by the channel plate. The right part represents how by manipulating the sample position, one can measure different areas of the Brillouin zone: pink areas represent regions in k-space, where ARPES measurements can be carried out at particular sample positions.

The MoS_2 monolayer is a promising material in the field of optics: it features a direct band gap at the $\overline{\mathrm{K}}$ point. In Fig. 4.7(a) we show the ARPES image of MoS_2 valence band states at the MoS_2 $\overline{\mathrm{K}}$ point measured along $\overline{\Gamma}$-$\overline{\mathrm{M}}$. The top MoS_2 valence band state at $\overline{\mathrm{K}}$ is originally the out-of-plane spin-split via spin-orbit interaction. The sample quality allowed us to resolve this spin-orbit splitting: we extracted the value to be $\sim$ 185 meV. Notably, it is larger than the value of about 145 meV, which is usually reported for a MoS_2 monolayer on other substrates[56, 131]. On the other hand, it matches the value usually observed for bulk MoS_2[131].

In Fig. 4.7(a) (in the region of the MoS_2 $\overline{\mathrm{K}}$ point) at a BE of 3 eV, one can see the π-state of graphene. As it was discussed in section 3.4.2, MoS_2 and graphene have different lattice parameters: four unit cells of the MoS_2 monolayer match with five unit cells of graphene. Therefore graphene and MoS_2 $\overline{\mathrm{K}}$ points are separated in k-space. We indicated this separation in Fig. 4.5 by dash-dotted lines labelled by $\overline{\mathrm{K}}_{MoS_2}$ and $\overline{\mathrm{K}}_{gr}$. One can also think about MoS_2-graphene Brillouin zones: graphene's Brillouin zone is slightly bigger than MoS_2's, as is shown in insets in Fig. 4.7(c,d).

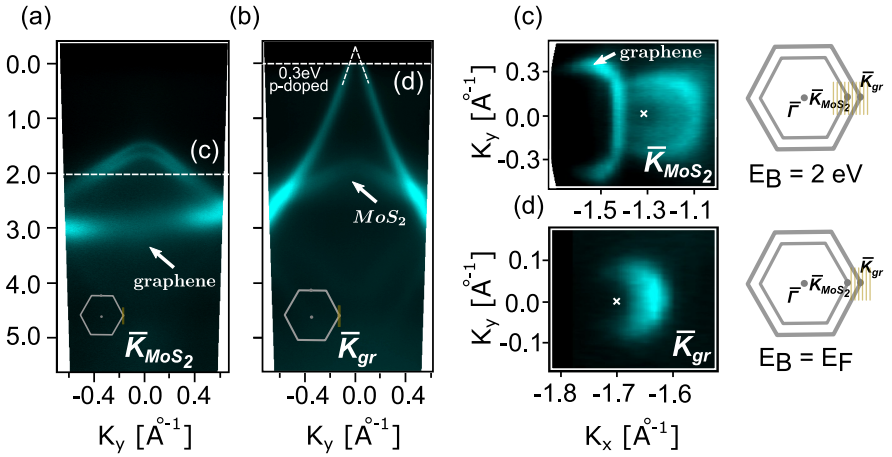

Figure 4.7: High-resolution ARPES dispersion of MoS_2/graphene/Co. (a) MoS_2 valence band in the region of MoS_2 $\overline{K}$ point measured along the direction perpendicular to $\overline{\Gamma}$-$\overline{K}$. (b) Graphene π-states in the region of graphene $\overline{K}$ point measured perpendicular to the $\overline{\Gamma}$-$\overline{K}$ direction. (c) Constant-energy contour at a binding energy of 2 eV obtained by ARPES mapping in the graphene region and MoS_2 $\overline{K}$ points. (d) Fermi surface in the region of graphene $\overline{K}$ point. All ARPES data were acquired at 60 eV photon energy.

Figure 4.7(c,d) shows energy slices of ARPES maps in the regions of MoS_2 and graphene $\overline{K}$ points correspondingly. In Fig. 4.7(c) one can see an energy slice at $E_b = 2\ eV$: two concentric circles represent MoS_2 spin split states in the region of $\overline{K}$ in different k-plane, as represented in Fig. 4.7(a).The MoS_2 $\overline{K}$ point can be easily determined as the center of above mentioned circles. On the left side of Fig. 4.7(c), one can see a semicircle shaped state - this is the graphene π-state.

In Fig. 4.7(d) one can see the Fermi surface (an energy slice at $E_b = 0\ eV$) in the region of the graphene $\overline{K}$ point. The shape represents a circle, and one can draw two conclusions: First, the circle is much brighter on the right side, which happens due to the photoionization cross-section, which indicates graphene sublattices symmetry is not broken. Second, graphene is doped; otherwise, the graphene Fermi surface would be represented by a dot. We extracted the doping value by linear interpolation of the graphene π-state in Fig 4.7(b). Graphene features 0.3 eV p-doping. We relate the doping to sulfur intercalation, as we saw a similar graphene p-doping in the case of sulfur intercalated graphene/Co in section 3.3.3. Interestingly, in Fig 4.7(b) one can also see the MoS_2 state from the second MoS_2 Brillouin zone.

4.2.2 Free MoS_2 monolayer: Tight binding model

Performing ARPES, we proved that the MoS_2 monolayer could be obtained on the graphene/Co substrate. The Co film is a ferromagnetic substrate, and we expect to

witness a magnetic proximity effect. Using the tight-binding approximation, we theoretically consider a MoS_2 monolayer in an external in-plane magnetic field and try to quantitatively investigate effects related to magnetism in the MoS_2 band structure.

We use the Tight Binding model described in Ref. [56]. Figure 4.8 represents a free-standing MoS_2 band structure calculated in the framework of the Tight-Binding approximation. When the magnetic field is applied, the state at the $\overline{\Gamma}$ point in the valence band splits. It is easy to assume that such a feature corresponds to the Zeeman effect. Similarly, one can recognize the splitting in the region of the $\overline{K}$ point conduction band states.

It is worth noticing that the Tight Binding calculation representation is highly exaggerated; the external magnetic field was chosen to be around B_x=1000 T to make the effect visible on the full scale of MoS_2 states. The value of the splitting is determined by the Zeeman effect, which the following formula can estimate.

$$\Delta E = -\vec{\mu} \cdot \vec{B},$$

where $\vec{\mu}$ is magnetic moment of the state. It is worth mentioning that the Tight Binding model does not give a realistic k-dependence and only qualitatively shows the effect.

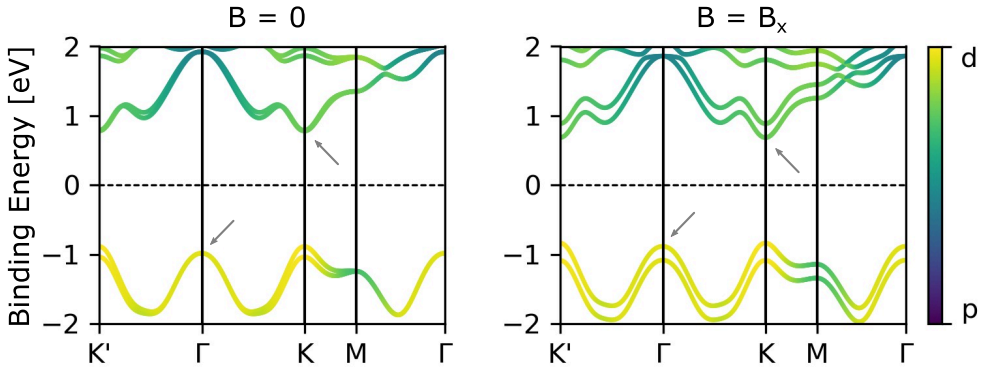

Figure 4.8: Tight-Binding calculation of free-standing MoS_2 monolayer. Left - in presence of no magnetic field; right - in presence of in-plane along $\overline{\Gamma}$- $\overline{M}$.

4.2.3 Free MoS_2 monolayer: DFT computations

Using Tight Binding approximation, we estimated how the band structure of the free-standing MoS_2 monolayer could be modified in the presence of an external in-plane magnetic field. Now we use the DFT approach to do the same in more detail.

Figure 4.9(b) represents the electronic band structure of free-standing MoS_2 monolayer under the conditions of a zero magnetic field. The band structure is presented in the $\overline{K}$-$\overline{\Gamma}$-$\overline{K'}$ direction of the Brillouin zone. The color is chosen to be gray when representing a zero in-plane spin polarisation of the states. Figures 4.9(a) and (c) compare

free-standing MoS_2 monolayer band structures in the regions of $\overline{\Gamma}$ (Fig. 4.9(a)) and $\overline{K}$ (Fig. 4.9(c)) under zero and $B_x = 100\ T$ external in-plane magnetic field.

In Fig. 4.9(a) one can see that in the case of zero magnetic field (left) the state at $\overline{\Gamma}$ is spin degenerate (we colored it grey). In the case of the in-plane magnetic field, the state is spin split by 23 meV – we colored spins with opposite in-plane directions as purple and green. The purple direction lies along the applied magnetic field while the green is opposite to it. We described S_x values as $S_x/S{\cdot}100\%$.

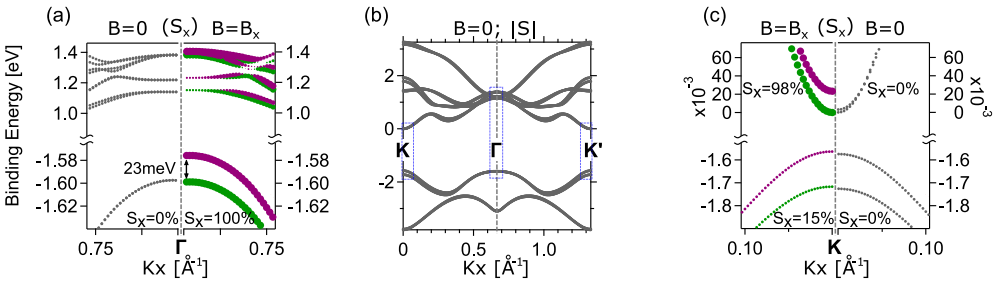

Figure 4.9: DFT representation of free-standing spin-dependent MoS_2 electronic states under different external conditions: zero magnetic field and in-plane magnetic field. (b) Calculation along the full $\overline{K}$-$\overline{\Gamma}$-$\overline{K'}$ direction at zero magnetic field. (a) Comparison between the in-plane spin structure at zero (left) and 100 T in-plane magnetic field near $\overline{\Gamma}$(right). (c) Comparison between the in-plane spin structure at zero (right) and 100 T in-plane magnetic field (left) near $\overline{K}$.

In the region of $\overline{K}$ (Fig. 4.9(c)) the situation is qualitatively different to the one at $\overline{\Gamma}$. In the case of zero magnetic field (right), the states in the valence and the conduction band states are already spin split in the out-of-plane direction (we colored them grey, as we only color the in-plane spin direction with $S_x \neq 0$). Under the applied external in-plane magnetic field, the S_x component of the valence band becomes 15%, and the S_x component of the conduction band becomes 98% polarized! (purple direction lies along an applied magnetic field, and green is opposite to it.) This observation means that under an external in-plane magnetic field, the MoS_2 electronic states in the region of the $\overline{K}$ point turn from out-of-plane spin direction to the in-plane spin direction in the conduction band and cant to the in-plane spin direction in the valence band.

The MoS_2 monolayer is a direct-band gap semiconductor. This band gap is determined by the top valence band states and the bottom conduction band states, that are located at $\overline{K}$ and $\overline{K'}$ points (see Fig. 4.9(b)). Therefore, the properties of the electronic states at $\overline{K}$ and $\overline{K'}$ points determine the electronic and optical properties of MoS_2.

4.2.4 MoS_2/graphene/Co: DFT computations

In section 4.2.3 we have shown that an external in-plane magnetic field of 100 T introduces significant changes into the MoS_2 electronic structure. In particular, the state at the $\overline{\Gamma}$ point becomes a 23 meV in-plane spin split. At the $\overline{K}$ point, the modifications

of the electron spin structure is more complex: the valence band states gain 15% of S_x polarization (while at B_x=0 S_x=0), and the conduction band states gain 98% (while at B_x=0 S_x=0).

We started this consideration from a simple free-standing MoS_2 in an external magnetic field because such calculation requires less than a minute of computational time of the standard PC and only a few dozen MB of RAM. The tight-binding models also requires a similar amount of computational resources. One must remember, the magnetic proximity effect is not exactly similar to the external magnetic field; it depends on the interaction mechanisms.

In order to understand how a magnetized Co layer can influence the MoS_2 monolayer, we constructed the following supercell: the 4×4 extension of the hexagonal MoS_2 unit cell on the 5×5 extension of the graphene unit cell on a 4-atom-thick cobalt slab (see Fig. 4.10). It is worth noticing that such a model requires a few orders of magnitude more computational resources than a simple free-standing MoS_2 monolayer in an external magnetic field. Importantly, graphene spatially separates MoS_2 from the the Co layer and can decrease the magnetic proximity effect as the distance between the lower S layer from MoS_2 and the top Co layer in this model is 5.44 Å.

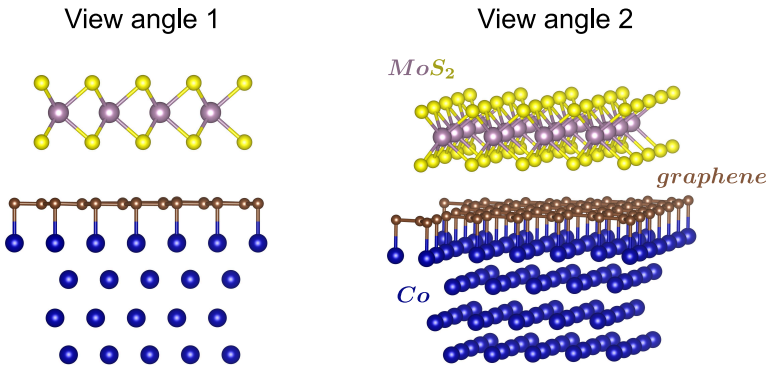

Figure 4.10: Supercell for DFT calculations of MoS_2/graphene/Co: 4×4 extension of hexagonal MoS_2 unit cell on the 5×5 extension of graphene unit cell on 4-atom-thick cobalt slab.

Figure 4.11(b) presents the calculated MoS_2 band structure along $\overline{\Gamma}$-$\overline{K}$ for the supercell presented in Fig. 4.10. Figure 4.11(a) and (c) compare the electronic band structure of zoomed regions near $\overline{\Gamma}$ (a) and $\overline{K}$ (b) points for the cases of a supercell with Co atoms magnetised along the MoS_2 x axis.

At the $\overline{\Gamma}$ point (Fig. 4.11(a)) one can see a spin splitting of 17.6 meV, which is similar to the case of free MoS_2 in the external magnetic field (section 4.2.3 and Fig. 4.9). We consider this as a sufficient evidence of the presence of the magnetic proximity effect.

One can easily calculate the effective magnetic field value of the magnetic proximity effect at the $\overline{\Gamma}$ point using the Zeeman formula:

$$\Delta E = -\vec{\mu} \cdot \vec{B},$$

where ΔE=17.6 meV. We estimated μ from the values in section 4.2.3 for free-standing MoS_2: for 100 T the splitting value was 23 meV, therefore magnetic moment μ was 0.23 meV/T. Now we can estimate an effective magnetic field: $B_x = \Delta E / \mu = 17.6 / 0.23$ T ≈ 76 T.

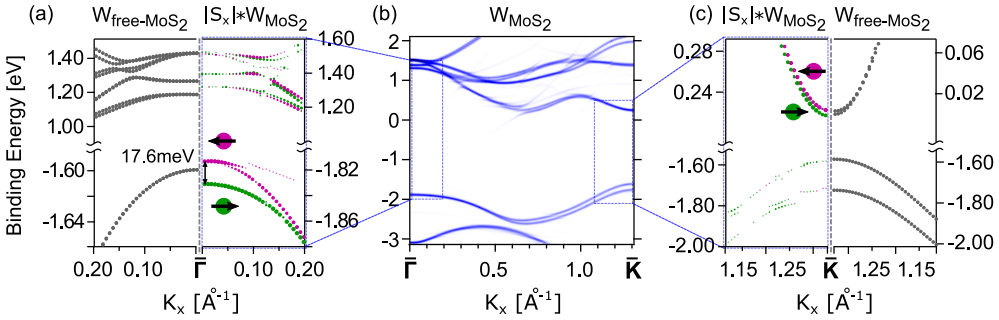

Figure 4.11: DFT representation of MoS_2 electronic and spin states of the model system 4×4 MoS_2 / 5×5 graphene / 4 layers of 5×5 Co, and its comparison to freestanding MoS_2. (b) Calculation of the model system along the full $\overline{\Gamma}$-$\overline{K}$ direction. The circle size represents the states' relative weight in the MoS_2 layer. (a),(c) Comparison between the in-plane spin structure of the model system and the one of free-standing MoS_2 near $\overline{\Gamma}$ (a) and $\overline{K}$ (c). The size of the colored circles represents the in-plane spin projections ($\pm$ S_x) multiplied by the MoS_2 states weight in DFT computation (W_{MoS_2})[140].

Let us take a look at the region of $\overline{K}$ in Fig. 4.11(c). In the conduction band, one can see a spin splitting, which is similar to the free-standing MoS_2 case in the external magnetic field. On the other hand, in the valence band, the situation is qualitatively different from the free-standing MoS_2 case: both spin up and down states have the same small S_x component (canting of the spin direction). Here (in $\overline{K}$ point), we conclude that this is also due to the magnetic proximity effect; however, an estimation of an effective magnetic field cannot be done easily.

The problem with computation of a complete MoS_2/graphene/CoS_x/Co system

In section 3.3.3, we have shown that during annealing of the graphene/Co system in sulfur flux, sulfur intercalates under graphene and makes it quasi-free-standing. Therefore, in the model in Fig. 4.10, one should have put sulfur between Co slab and graphene. We did not do that because of two reasons:
(1) We do not have a solid structural model for the CoS_x layer (see more in section 3.4.3 and Fig. 3.15).

(2) The computation time of a single core process of the FPLO package [141] was estimated to be more than one year for not even completely proper 10×10 graphene/CoS_x model supercell. Moreover, this not legitimate structure may not represent correctly the present CoS_x magnetic properties.

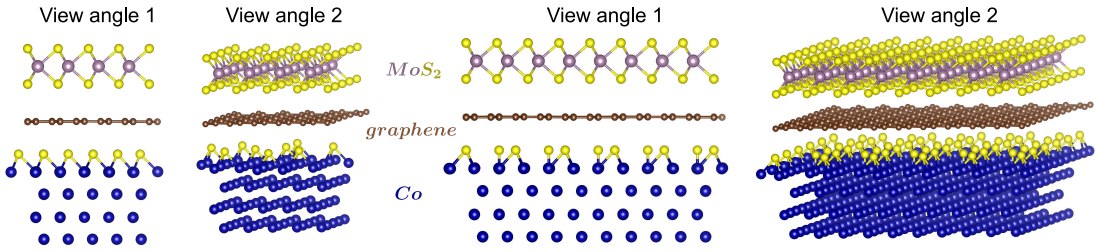

Figure 4.12: Two possible supercells for DFT calculations of MoS_2/graphene/CoS_x/Co system: left – 4×4 extension of hexagonal MoS_2 unit cell on 5×5 graphene on 5×5 Co-S on 4-atom-thick cobalt slab; right – 8×8 extension of hexagonal MoS_2 unit cell on 10×10 graphene on 8×8 Co-S on 4-atom-thick cobalt slab

Prior to not computing the complete MoS_2/graphene/CoS_x/Co system computations, we constructed two different super cells (see Fig. 4.12). The left one is the most straightforward solution of placing sulfur between graphene and Co: a 1×1 structure to Co; however, it does not correspond to either XPS or LEED data of CoS_x. The right one corresponds to XPS and LEED data; however, it is too big to apply the DFT method at present, and it is only one of a few possible options for sulfur atoms interacting with Co. It also does not correspond to STM measurements (see section 3.4.3)

If we were to determine the structure of CoS_x, we would make detailed XPS measurements of graphene/CoS_x/Co under different angles and, together with an STM study (see section 3.4.3), construct different CoS_x supercells. Afterwards, we would choose the one with the lowest free energy.

4.2.5 MoS_2/graphene/Co: spin-ARPES measurements and analysis

In-plane and out-of-plane spin projections for the sample and the detector

One may get confused when measuring spin directions (spin projections) of electronic states in a solid. The in-plane spin projections in the free MoS_2 monolayer are oriented in the MoS_2 2D plane. In contrast, experimental in-plane spin projections are oriented along a particular direction of the spin detector fixed in space. Similar, the out-of-plane spin projection in the MoS_2 monolayer is oriented perpendicular to a MoS_2 2D plane, while the out-of-plane spin projection in the spin analyzer is fixed. Confusion may arise when we rotate the sample position when we measure different areas of k-space via ARPES measurements. MoS_2 monolayer determines in-plane and out-of-plane spin-axis relatively to ones in the spin polarimeter in the spin detector.

The trick is based on the fact that we do not need to investigate all three spin projections (one out-of-plane and two in-plane). We need to analyze only two: out-of-plane and one in-plane direction, which is oriented along the magnetization of the Co film.

With this one-axis freedom, we can choose the experimental geometry to compensate for the rotation of the sample so that one in-plane axis of the sample and spin detector are the same. This convenient experimental geometry is the following: The sample polar rotation axis (Θ) and Co-magnetisation ($\vec{M}$) ax aligned along the analyzer slit (see the experimental geometry in Fig 4.13). Therefore, the sample in-plane axis that is aligned along the Co-magnetisation remains at the same position during polar angle rotation. Fortunately, the Co-magnetisation easy axis is $\overline{\Gamma}$-$\overline{\mathrm{M}}$ [142, 143]. Rotating the polar angle (Θ), we can adjust an experimental geometry to probe the sample in the $\overline{\mathrm{K}}$-$\overline{\Gamma}$-$\overline{\mathrm{K}'}$direction.

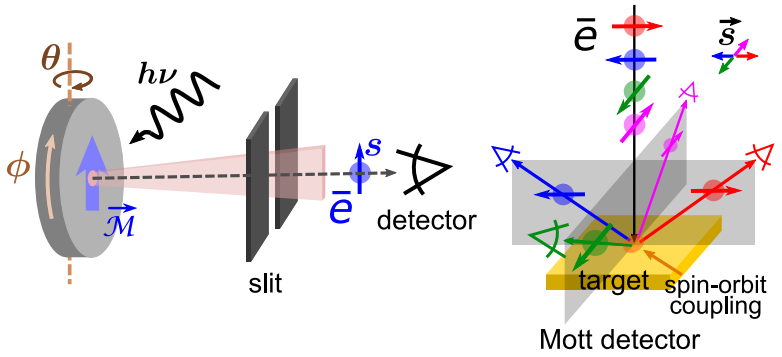

Figure 4.13: The scheme of how we used magnetization for spin-dependent measurements.

It is interesting to note that if we were to reach the $\overline{\mathrm{K}}$ point via tilt rotation, as shown in Fig. 4.6, such compensation would not work, as the in-plane axis of the sample and the spin detector could be misaligned.

In-plane spin projections at the MoS_2 $\overline{\Gamma}$ point

DFT calculations predict a spin splitting at the MoS_2 $\overline{\Gamma}$ point in the in-plane direction (see section 4.2.4). We performed two sets of independent measurements with the opposite magnetizations of a Co film to confirm this.

Measurements at the $\overline{\Gamma}$ point correspond to a normal emission angle photoemission process. The efficiency of the employed Mott detector is low (see more in the methods section), and an instrumental asymmetry mainly determines the difference of the signal from different spin channels. In the ideal scenario, Fig. 4.14b and Fig. 4.14e for opposite magnetization should look exactly reversed, which means that the colors should be swapped. However, this is not the case for the raw data before the normalization procedure is implemented.

The final result of spin-ARPES measurements is presented in Fig. 4.14c. It is obtained using the normalization procedure that takes into account the efficiency of spin detectors in the form of the Sherman function and both measurement sets with opposite magnetization (Fig. 4.14b and Fig. 4.14e).

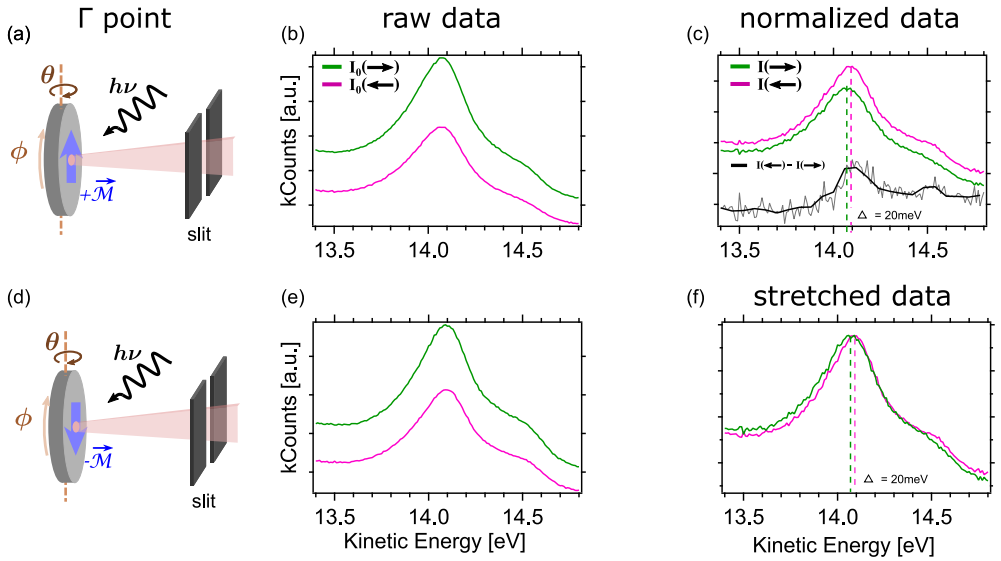

Figure 4.14: Presentation of spin-resolved ARPES experiment with opposite sample magnetizations. (a,d) The geometry of the sample, its magnetization, the light beam, and the analyzer slit. The representation of the raw data after spin-resolved measurements for two opposite sample magnetizations (b) and (d) before the normalization procedure. (c) The data representation after the normalization procedure. (d) The data representation shows the spin splitting in a more reader-friendly way. $I_0(\rightarrow)$ and $I_0(\leftarrow$ are raw intensities of spin spectra in opposite in-plane directions before the normalization procedure; $I(\rightarrow)$ and $I(\leftarrow$ are intensities after the normalization procedure.

One can argue that the difference between two spectra representing measurements of opposite spin components can be due to a spin-polarised Co background. Indeed, the Co background plays a significant role in the presented data (see Fig. 4.14c). One can see that one spectrum features higher intensity than the other, while DFT calculations predict a spin splitting of the MoS_2 state at the $\overline{\Gamma}$ point. In order to illustrate such phenomena, we plotted the difference of the spectra as a curve of black color and placed it under spin-resolved spectra. If the only difference between spectra of different spin were due to a Co background, the difference spectrum would feature background shape. However, the different spectra have an extremum in the region of Mo states. To illustrate the actual and predicted spin splitting, we starched the represented data in the intensity direction in Fig. 4.14f.

Energy resolution and 20 meV spin splitting Looking at the spin-resolved spectra in Figs. 4.14c,f, one can argue that the energy resolution is less than the value of

spin splitting (20 meV). All spectra were obtained at room temperature; therefore, already the temperature should restrict the resolution to ∼50 meV. How can we resolve the 20 meV spin split given that our total spectral resolution of ARPES is limited to ∼100 meV for the spin-resolved settings? The answer is that spin-resolved measurements require two independent electron detectors. Independent measurements allow us to overcome the limit.

Another reasonable question would be: What if one of two independent detectors has a slight kinetic energy miscalibration? Indeed, the case that an electron with the same kinetic energy can be resolved with slightly different measured kinetic energy in different electron detectors is possible. And such measurement will produce an artificial spin splitting. However, this artificial spin splitting will appear only in the raw data, as the normalization procedure relies on swapping the signals between those two detectors, and this error will be removed by the subtraction.

Normalization via sample rotation Looking at Fig. 4.14a and Fig. 4.14d, one can notice that a sample rotation by 180° of the azimuth angle is equivalent to an opposite magnetization given the C6 symmetry of the sample. We have performed such measurements and the corresponding normalization procedures. The result was the same as presented in Fig. 4.14c.

This result supports the fact that reverse of the remanent magnetization takes place. Before these additional measurements, we were concerned that something else (not the sample) could have been magnetized and, therefore, could influence the measurements.

Out-of-plane spin projection at MoS_2 $\overline{\Gamma}$ point

In the case of the in-plane Co film magnetization, DFT calculations predict a spin splitting in the in-plane direction. Can we check the out-of-plane spin structure experimentally? There is not much purpose in these results, but we get them simultaneously with the in-plane data for free.

The meaning of the reverse in-plane magnetization and sample rotation for the out-of-plane spin direction measurements At the $\overline{\Gamma}$ point, magnetization to the opposite in-plane direction and rotation of the azimuth angle do not swap signals in different spin detectors in the out-of-plane direction. In other words, both can only impact the in-plane system's spin structure and in-plane-related measurements correspondingly. Therefore, spectra in out-of-plane spin detectors must be identical under the abovementioned changes. Spin-resolved spectra after the normalization procedure must feature zero spin-polarisation even if the polarisation of the states is present.

Remark: for $\overline{\mathrm{K}}$ and $\overline{\mathrm{K}'}$ points, the re-magnetization should also change nothing, but azimuth rotation can be used for the normalization.

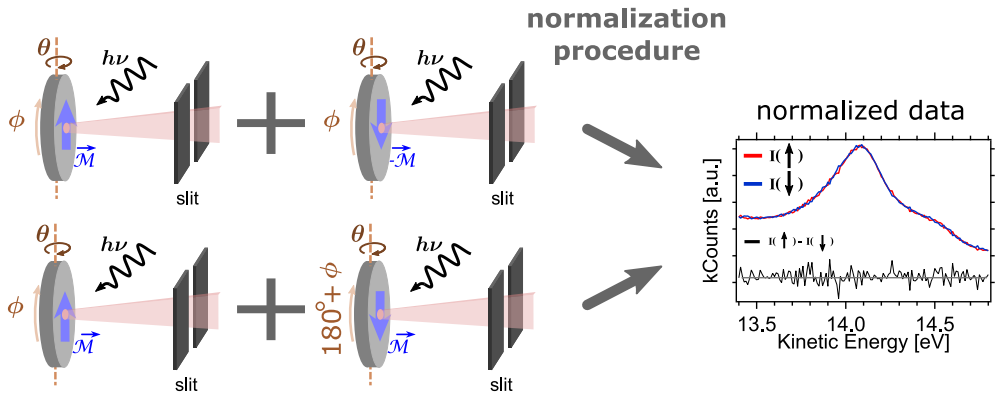

Figure 4.15: The scheme and the result of the out-of-plane spin-resolved photoemission spectra at the $\overline{\Gamma}$ point after the normalization procedure in two cases: the reverse magnetization of the sample (top-left) and the sample rotation (bottom-left). Both approaches provide a similar result.

If we detect any out-of-plane spin polarisation or splitting after the normalization procedure, that would indicate an error in the experiment, such as instrumental problems or sample positioning problems. Problems in the sample position reproducibility may lead to an inability to perform the normalization procedure.

We performed the normalization procedure on out-of-plane measurements for opposite sample magnetization and sample rotation and summarised it in Fig. 4.15. The negative result of the absence of spin polarisation supports the non artificial nature of our not negative result in the in-plane direction.

In-plane spin projection at the MoS_2 $\overline{K}$ point

DFT calculations predict a slight spin-canting of electronic states in the region of the MoS_2 $\overline{K}$ point in the in-plane direction (see section 4.2.4). We performed four independent measurements with the opposite magnetization of a Co film and azimuth rotation by 180°.

These four sets can be paired for the normalization procedure in 6 ways. Let's think first about four possible states of azimuth rotation and Co magnetization: $(\phi,\vec{M})$, $(180+\phi,\vec{M})$, $(\phi,-\vec{M})$, and $(180+\phi,-\vec{M})$. The possible pairs are:
(1) – $\{(\phi,\vec{M});(\phi,-\vec{M})\}$; (2) – $\{(180+\phi,\vec{M});(180+\phi,-\vec{M})\}$;
(3) – $\{(\phi,\vec{M});(180+\phi,\vec{M})\}$; (4) – $\{(\phi,-\vec{M});(180+\phi,-\vec{M})\}$;
(5) – $\{(\phi,\vec{M});(180+\phi,-\vec{M})\}$; (6) – $\{(\phi,-\vec{M});(180+\phi,\vec{M})\}$.

(5) and (6) are useless for constructive results after the normalization procedure, as re-magnetization and 180° azimuth rotation compensate for each other. An expected negative result can support the assumption that the experiment does not contain any error. We have verified this.

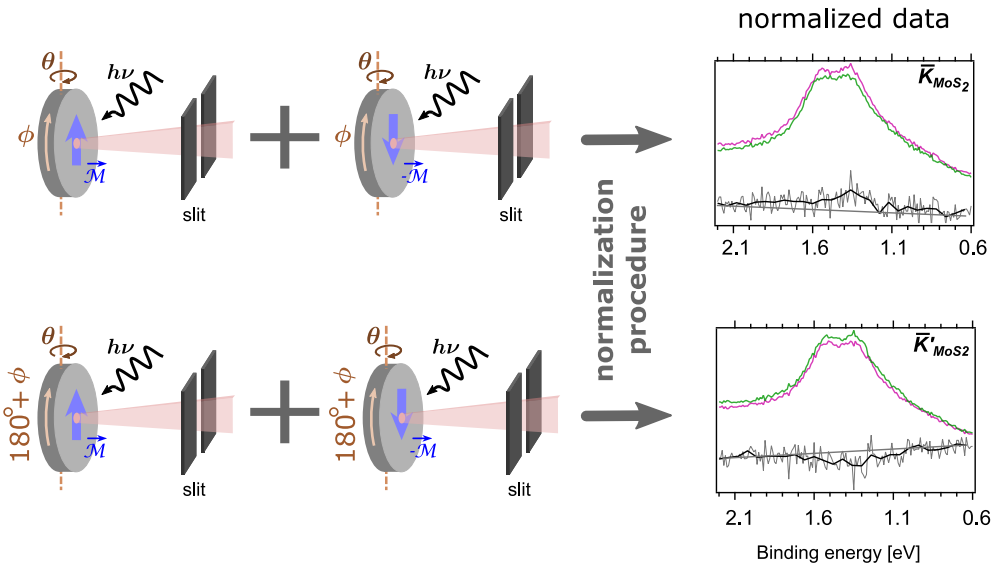

Figure 4.16: The scheme and the result of the in-plane spin-resolved photoemission spectra after the normalization procedure at $\overline{\mathrm{K}}$ (top-right) and $\overline{\mathrm{K}}'$ (bottom-right) in two cases: the reverse magnetization of the sample (top-left) and the sample rotation (bottom-left).

(3) and (4) are expected to provide similar results as (1) and (2). We have verified this. However, the sample rotation may lead to measurements of slightly diffident spots on the sample. We also leave those data from the following discussion not to get confused with terms.

(1) and (2) are summarised in Fig. 4.16. The data confirm the DFT predictions. One can notice that normalized data on the right panels seem to be inverted. This is the result of the data set order in the normalization procedure. It does not carry any physical meaning, but we chose this way of representation to be more illustrative for the terms we introduce.

To ease the following discussion we will call (1) – $\{(\phi,\vec{M});(\phi,-\vec{M})\}$ set as MoS_2 $\overline{\mathrm{K}}$ point and (2) – $\{(180{+}\phi,\vec{M});(180{+}\phi,-\vec{M})\}$ as MoS_2 $\overline{\mathrm{K}}'$ point. If MoS_2 were a single domain system, these definitions would be fully correct. But the system consists of multiple mirror domains, and we do not specify which group of domains we mean. However, we propose these driven by the experimental geometry definitions.

Out-of-plane spin projection at MoS_2 $\overline{\mathrm{K}}$ point

DFT calculations predict a slight spin-canting of electronic states in the region of the MoS_2 $\overline{\mathrm{K}}$ point in the in-plane direction (see section 4.2.4). What does this mean for the out-of-plane polarisation of these states?

The free-standing MoS_2 monolayer features out-of-plane spin splitting of the valence band states in the region of the $\overline{\mathrm{K}}$ point. According to the DFT calculations, the out-of-plane spin-polarization should still be observed.

On the other hand, our MoS_2/graphene/Co system contains multiple mirror domains. As shown in section 1.5.2, the aggregation of spin-resolved signals of mirror domains may lead to the absence of spin polarisation in the measured spectrum (see Fig. 1.7). The photoemission diffraction (PED) study suggests the equal distribution of mirror domains in the sample. One should expect to get zero out-of-plane polarization of MoS_2 valence band states in the region of the $\overline{\mathrm{K}}$ point. But this must be checked.

We performed four independent spin-resolved measurements to obtain the in-plane spin polarisation. As a free compliment, we automatically got another four data sets for out-of-plane polarization.

Similar to the in-place case, there are six possible pairs to implement the normalization procedure:
(1) – $\{(\phi,\vec{M});(\phi,-\vec{M})\}$; (2) – $\{(180{+}\phi,\vec{M});(180{+}\phi,-\vec{M})\}$;
(3) – $\{(\phi,\vec{M});(180{+}\phi,\vec{M})\}$; (4) – $\{(\phi,-\vec{M});(180{+}\phi,-\vec{M})\}$;
(5) – $\{(\phi,\vec{M});(180{+}\phi,-\vec{M})\}$; (6) – $\{(\phi,-\vec{M});(180{+}\phi,\vec{M})\}$.

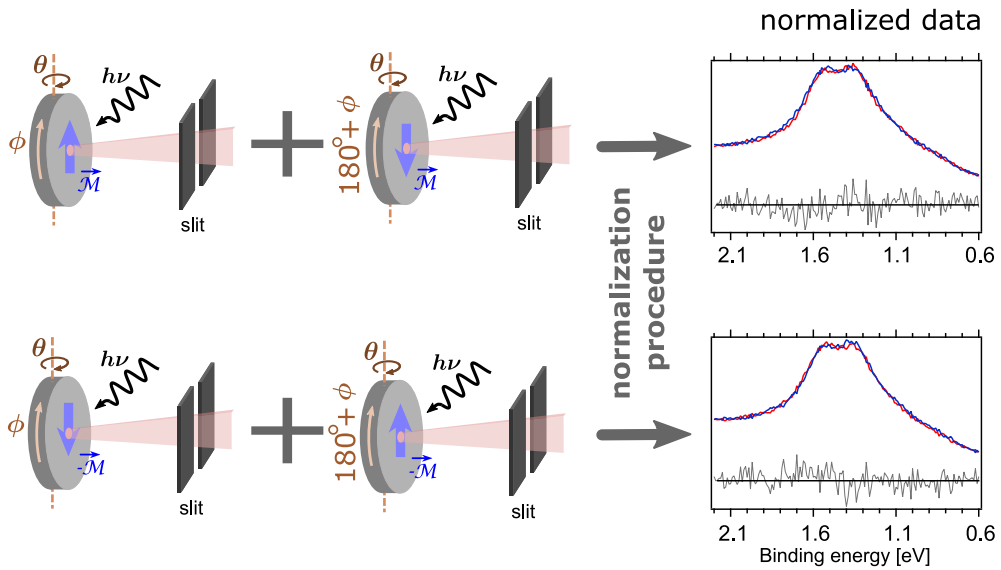

Figure 4.17: The scheme and the result of the out-of-plane spin-resolved photoemission spectra after the normalization procedure in two cases of the sample rotation (bottom-left).

(1) and (2) differ in the direction of in-plane magnetization. As we are trying to confirm out-of-plane properties, both pairs provide similar data, and we cannot use them for out-of-plane related normalization.

Both (3) and (4) would represent geometrically opposite $\overline{\mathrm{K}}$ and $\overline{\mathrm{K}'}$ points for a single domain system. One may use this property to swap the intensities in spin channels

and use this to perform normalization. However, our system is represented by an equal amount of mirror domains, where $\overline{\mathrm{K}}$ and $\overline{\mathrm{K}'}$ points are similar. The data are summarised in Fig. 4.17. The negative result confirms both an equal amount of mirror domains and the absence of mistakes in the experimental geometry.

(5) and (6) are similar to (3) and (4), given the meaninglessness of in-plane opposite magnetization for out-of-plane measurements (similar to cases (1) and (2))

Normalisation procedure: equations

Above, we discussed how we could vary experimental parameters to use a normalization procedure correctly (compensate for an instrumental asymmetry). In this subsection, we will look at particular formulas used. In our case, we applied a modification of a procedure proposed in publication[144].

To represent spin-resolved spectra, we used the following formulas. In our study, we are interested in in-plane and out-of-plane spin directions. We first consider an imaginary α-spin direction:

$$\begin{aligned} I(\vec{\alpha}) &= \langle I \rangle \cdot (1+P), \\ I(\overrightarrow{-\alpha}) &= \langle I \rangle \cdot (1-P), \end{aligned} \tag{4.10}$$

where $I(\vec{\alpha})$ and $I(\overrightarrow{-\alpha})$ are values usually presented in final data representations.

$$\langle I \rangle = (I_L^+ + I_L^- + I_R^+ + I_R^-)/4, \tag{4.11}$$

$$P = \frac{1}{S} \frac{\left(\sqrt{I_L^+ I_R^-} - \sqrt{I_L^- I_R^+}\right)}{\left(\sqrt{I_L^+ I_R^-} + \sqrt{I_L^- I_R^+}\right)}, \tag{4.12}$$

where P is the polarization; S is the Sherman function;
I^+ and I^- are the recorded intensities in spin channels of the Mott detector for opposite magnetizations along the $\vec{\alpha}$ direction;
I_R and I_L are the recorded intensities in geometrically opposite spin channels; for simplicity of notation, let us call them the right (R) and the left (L) detectors.

In-plane In our particular case for in-plane spin properties of the MoS_2 monolayer at $\overline{\Gamma}$ $\overline{\mathrm{K}}$ and $\overline{\mathrm{K}'}$ points, we used the following equations:

$$\begin{aligned} I(\rightarrow) &= \langle I \rangle \cdot (1+P), \\ I(\leftarrow) &= \langle I \rangle \cdot (1-P), \end{aligned} \tag{4.13}$$

where $(\rightarrow)$ and $(\leftarrow)$ are the opposite in-plane spin directions along the magnetisation axis of the Co film.

and

$$\langle I \rangle = (I_{ch1}^{\vec{M}} + I_{ch1}^{\overrightarrow{-M}} + I_{ch3}^{\vec{M}} + I_{ch3}^{\overrightarrow{-M}})/4, \tag{4.14}$$

$$P = \frac{1}{S} \frac{(\sqrt{I_{ch1}^{\vec{M}} I_{ch3}^{\overrightarrow{-M}}} - \sqrt{I_{ch1}^{\overrightarrow{-M}} I_{ch3}^{\vec{M}}})}{(\sqrt{I_{ch1}^{\vec{M}} I_{ch3}^{\overrightarrow{-M}}} + \sqrt{I_{ch1}^{\overrightarrow{-M}} I_{ch3}^{\vec{M}}})}, \tag{4.15}$$

where $\vec{M}$ and $\overrightarrow{-M}$ are opposite sample magnetizations along the magnetization axis of the Co film;
$I^{\vec{M}}$ and $I^{\overrightarrow{-M}}$ are the recorded intensities in spin channels of the Mott detector for opposite magnetizations along the magnetization axis of the Co film;
I_{ch1} and I_{ch3} are the recorded intensities in geometrically opposite first and third spin channels.

Out-of-plane In our particular case for out-of-plane spin properties of MoS_2 monolayer at $\overline{\Gamma}$ and $\overline{\mathrm{K}}$ points, we used the following equations:

$$\begin{aligned} I(\uparrow) &= \langle I \rangle \cdot (1 + P), \\ I(\downarrow) &= \langle I \rangle \cdot (1 - P), \end{aligned} \tag{4.16}$$

where ($\rightarrow$) and ($\leftarrow$) are the opposite spin directions along the magnetisation axis of the Co film.

and

$$\langle I \rangle = (I_{ch2}^{\phi} + I_{ch2}^{180+\phi} + I_{ch4}^{\phi} + I_{ch4}^{180+\phi})/4, \tag{4.17}$$

$$P = \frac{1}{S} \frac{(\sqrt{I_{ch2}^{\phi} I_{ch4}^{180+\phi}} - \sqrt{I_{ch2}^{180+\phi} I_{ch4}^{\phi}})}{(\sqrt{I_{ch2}^{\phi} I_{ch4}^{180+\phi}} + \sqrt{I_{ch2}^{180+\phi} I_{ch4}^{\phi}})}, \tag{4.18}$$

where ϕ and 180°+ϕ correspond to azimuth sample rotation by π;
I_{ch2} and I_{ch4} are the recorded intensities in geometrically opposite second and fourth spin channels.

4.3 Control over MoS_2 optical properties

4.3.1 MoS_2 optical properties: short recap

The MoS_2 monolayer already features peculiar properties such as an optically active band gap in regions near $\overline{\mathrm{K}}$ and $\overline{\mathrm{K}'}$ points in the Brillouin zone. MoS_2 electronic states near $\overline{\mathrm{K}}$ and $\overline{\mathrm{K}'}$ points in the Brillouin zone correspond to $\overline{\mathrm{K}}$ and $\overline{\mathrm{K}'}$ optical valleys (sometimes called K^+ and K^- valleys). For our following discussion, the most interesting property of MoS_2 monolayer is valley-spin locking. For this, we need to keep in mind three essential facts.
(1) In each valley electrons with only a particular out-of-plane direction can be excited

(see Fig. 4.18(a)).
(2) Both electrons, excited to the conduction band, and holes, left in the valence band, remain in the same valley and cannot change it without a considerable energy change or a spin flip (see Fig. 4.18(b)).
(3) Each valley features a particular chirality: it can be selectively pumped via circularly polarised light. Consequently, exciton recombination in this valley happens via the emission of a photon with a particular circular polarisation (see Fig. 4.18(c)).

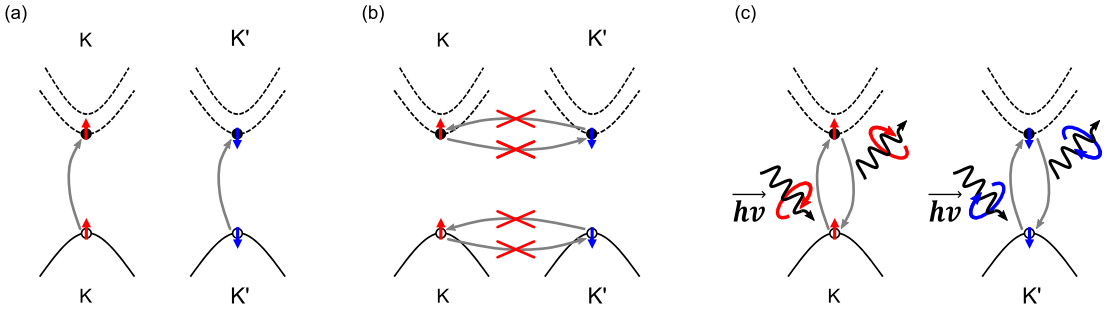

Figure 4.18: Schematic representations. (a) In a particular valley only electrons with a particular out-of-plane spin can be excited. (b) Electrons and holes cannot scatter to another valley without significant energy loss or a spin flip. (c) Each valley can be selectively pumped with σ^+ or σ^- circular polarized light. Consequently, a recombination process in each valley happens by emitting a particular circular polarized photon.

There are a few more things to keep in mind that determine the exciton properties in MoS_2 monolayer:
(1) Electronic states are the skeleton of the exciton structure: changing their symmetry or spin may significantly influence the exciton states.
(2) Optical experiments mainly provide information about bright excitons, both bright and dark excitons are present, and both types determine the dynamic properties of the system.
(3) Excitons in MoS_2 monolayer can move freely through the material. Moreover, excitons may even tunnel to another material, such as the substrate or a second MoS_2 layer.
(4) Excitons are excited states, and for any possible application, one should pay attention to their lifetime. The exciton lifetime depends on possible relaxation mechanisms and dielectric screening. Different substrates may influence both of these factors.

4.3.2 MoS_2 monolayer in a magnetic field

At the $\overline{\Gamma}$ point in the MoS_2 valence band the state is spin degenerate, and we observe a Zeeman-like (see Fig. **??**(a)) spin splitting of this state in the spin-resolved spectra for in-plane Co magnetization (see more in Section 4.2.5). For the out-of-plane scenario, a similar behavior is expected, which was confirmed by our DFT calculations.

The situation is different at the $\overline{\mathrm{K}}$ and $\overline{\mathrm{K}'}$ points: the states are already out-of-plane spin split due to spin-orbit interaction. Moreover, to consider optical transitions, we will look at both valence and conduction band electronic states.

MoS_2 in out-of-plane magnetic field

In Fig. 4.19(a) one can see a schematic representation of electronic states and their optical coupling. The extreme left and right pictures represent the situation with zero magnetic fields, corresponding to excitons with the same energy in $\overline{\mathrm{K}}$ and $\overline{\mathrm{K}'}$ valleys. The external magnetic field in the out-of-plane direction moves spin-up states to lower binding energy and spin-down states to higher ones (see Fig. 4.19(a)). Consequently, band gaps at $\overline{\mathrm{K}}$ and $\overline{\mathrm{K}'}$ points become different.

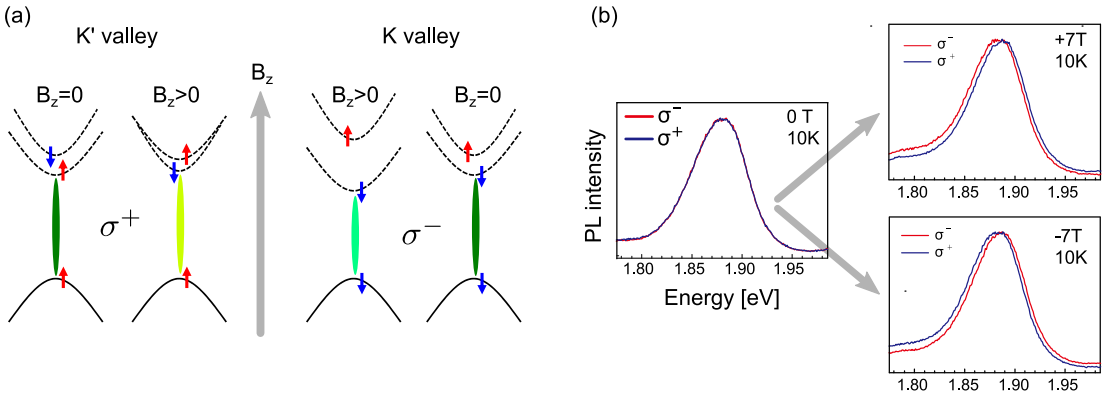

Figure 4.19: (a) Schematic representations of the shift of electronic states at $\overline{\mathrm{K}}$ and $\overline{\mathrm{K}'}$ points under external out-of-plane magnetic field compared to the zero-magnetic-field scenario. (b) The experimental photo luminescence demonstrates the exciton energy shift under an external out-of-plane magnetic field in a MoS_2 monolayer[13]

Such phenomenon can be observed in photoluminescence experiment (see Fig. 4.19(b)). At zero external magnetic field, photoluminescence peaks corresponding to excitons in $\overline{\mathrm{K}}$ and $\overline{\mathrm{K}'}$ valleys look similar (we can resolve them separately using circularly polarised light in opposite orientations). On the other hand, one can see that an external magnetic field results in opposite orientation shifts of excitons in $\overline{\mathrm{K}}$ and $\overline{\mathrm{K}'}$ valleys.

It is worth noticing that if the states in the valence and conduction bands moved by the same energy (had the same g-factor), then there would be zero shift of the exciton energy.

Given that the optical band gap is different in different valleys, most of the described properties of the MoS_2 monolayer remain. It is still a direct band gap semiconductor, and $\overline{\mathrm{K}}$ and $\overline{\mathrm{K}'}$ valleys still feature a particular chirality; the spin-valley locking is still in place.

MoS_2 monolayer in in-plane magnetic field

In zero magnetic field and in an external out-of-plane magnetic field scenario, all states feature spins in the direction perpendicular to the MoS_2 monolayer. When we consider an in-plane magnetic field, we add a new in-plane dimension to the consideration of spins.

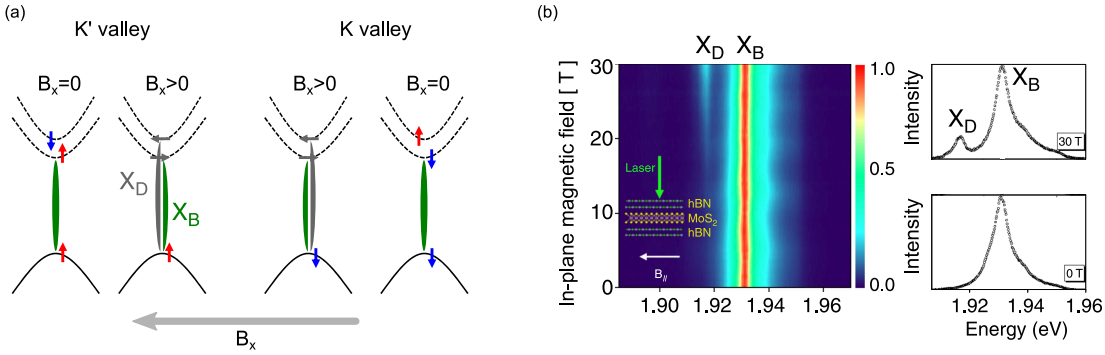

Figure 4.20: (a) Schematic representations of the effect of an in-plane magnetic field on the spin direction in the regions of $\overline{\mathrm{K}}$ and $\overline{\mathrm{K}'}$ points of MoS_2 monolayer. The spin direction of the states in the valence band remains similar, while the spin direction in the conduction band tilts to the in-plane direction. Such an effect leads to the brightening of a dark exciton which is shown in (b) panel[15]

In Fig. 4.20(a) one can see a schematic representation of electronic states and their optical coupling. An in-plane magnetic field affects valence and conduction band states in regions of $\overline{\mathrm{K}}$ and $\overline{\mathrm{K}'}$ points differently. In the valence band states, the spin-orbit coupling splits the state in the out-of-plane direction. This splitting is about 200 meV. In the conduction band, the splitting is much less.

In the valence band, the magnitude of the out-of-plane spin splitting is so large that even extreme magnetic fields cannot overcome the out-of-plane spin polarization of these states. In the most extreme scenarios, the spin direction can only be slightly canted.

Oppositely, in the conduction band, the spin splitting magnitude is small, and the spin direction can be easily tilted. In Fig. 4.20(a), one can see that while the spin direction of valence band states remains the same under an external in-plane magnetic field, the states in the conduction band are pointed in the in-plane direction.

Such perpendicular spin directions in valence and conduction band states are expected to change the optical properties drastically. An optical transition is now possible to both conduction band states, as the projection of out-of-plane spin direction is similar to both spin-"left" and spin-"right" directions.

The excitons that couple states with opposite spin directions in $\overline{\mathrm{K}}$ and $\overline{\mathrm{K}'}$ points are so-called dark excitons, as they cannot recombine in the framework of optical selection rules. However, in the case of an in-plane magnetic field, the spin directions are now

tilted, and previously dark excitons gain the possibility to recombine in the framework selection rules and couple with a single photon. Such effect is so-called brightening[15] of a dark excitons[73]. Strictly speaking, dark excitons are no longer dark, but we would still name them this way in photoluminescence spectra.

In Fig. 4.20(b), one can see from a photo luminescence experiment [15] how the dark excitons can be brightened by introducing an external magnetic field: X_B refers to the peak of a bright exciton and X_D to the dark one. X_B and X_D peaks do not show equal intensity, as a 30 T magnetic field is not enough to tilt the spin direction of conduction band states completely to the in-plane direction.

In contrast to an out-of-plane one, an in-plane magnetic field drastically influenced the optical properties of the system: tilting the spin opens up new optical channels which were previously forbidden (dark excitons) and destroys spin-valley locking, which opens up new scattering channels for excitons and must greatly influence electronic and optical dynamic properties of the MoS_2 monolayer.

4.4 ARPES, DFT and optical discussion

4.4.1 The evidence of the in-plane magnetic proximity effect

Instead of placing a MoS_2 monolayer into an extremely strong magnetic field, we attempted to reach similar magnetic properties using the magnetic proximity effect[12]. We synthesized the MoS_2 monolayer atop graphene on a Co thin film system. The Co (0001) thin film consists of around 30 to 40 cobalt monolayers. It features in-plane ferromagnetic properties. We were able to magnetize the Co (0001) thin film along the in-plane easy axis ($\overline{\Gamma}$-$\overline{\mathrm{M}}$) and then check for any spin structure modifications using the spin-resolved photoemission.

In the region of $\overline{\Gamma}$ in the valence band where the state is supposed to be spin-degenerate for a free-standing MoS_2 monolayer, we observed a Zeeman spin splitting of about 20 meV (see Fig. 4.21(top-left)). Such splitting confirms that the magnetic proximity effect is present. We can use the MoS_2/graphene/Co system for a spin-resolved photoemission study of in-plane magnetic effects for the quasi-free-standing MoS_2 monolayer.

It is worth noting that such an approach is crucial for the method of spin-resolved photoemission, as photoemission cannot be performed in any magnetic field. It would work as a magnetic lens for photoexcited electrons disturbing their focusing and detection.

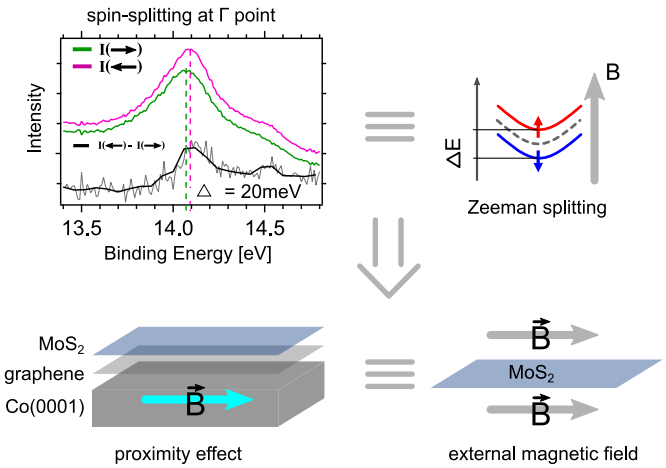

Figure 4.21: Evidence of the in-plane magnetic proximity effect in MoS_2 monolayer: MoS_2 valence band state spin-splits at $\overline{\Gamma}$ point similar to a Zeeman splitting.

4.4.2 Use of DFT simulation to predict electron and in-plane spin structure of MoS_2 monolayer in the conduction band

We have performed a spin-resolved photoemission of MoS_2/graphene/Co in the regions near $\overline{\Gamma}$ and $\overline{K}$ points. We have also performed DFT calculations of the model system 4×4 MoS_2 / 5×5 graphene / 4 layers of 5×5 Co. DFT simulations match spin-resolved photoemission data at both $\overline{\Gamma}$ and $\overline{K}$ points: in-plane Zeeman spin splitting of about 20 meV at the $\overline{\Gamma}$ point, and about 15% in-plane spin polarisation at the $\overline{K}$ point.

Taking these facts as evidence for the DFT predictions to be correct, we assume that the DFT predictions for MoS_2 conduction band states is also correct. The DFT calculation suggests two crucial conclusions:
(1) In the region of the $\overline{K}$ point in the MoS_2 conduction band the spin of the states tilts from the out-of-plane to the in-plane direction and becomes almost fully in-plane spin-polarized (98%) (see Fig. 4.22(bottom-right)).
(2) In the region of the $\overline{K}$ point in the MoS_2 valence band, the states are 15% in-plane spin-polarized. However, an additional DFT study shows that this polarization is localized on Co atoms, while the in-plane polarization in the conduction band is localized on Mo atoms (at the MoS_2 monolayer).
In this respect, when describing optical transitions in the MoS_2 monolayer, one can consider the out-of-plane spin polarisation in valence band states and the in-plane spin polarisation in conduction band states.

4.4.3 Relation of in-plane spin structure obtained from DFT to optical properties

In Fig. 4.23(middle), one can see the comparison of DFT simulations of electronic and spin structure of MoS_2/graphene/Co with magnetised Co film (left) and as free-standing

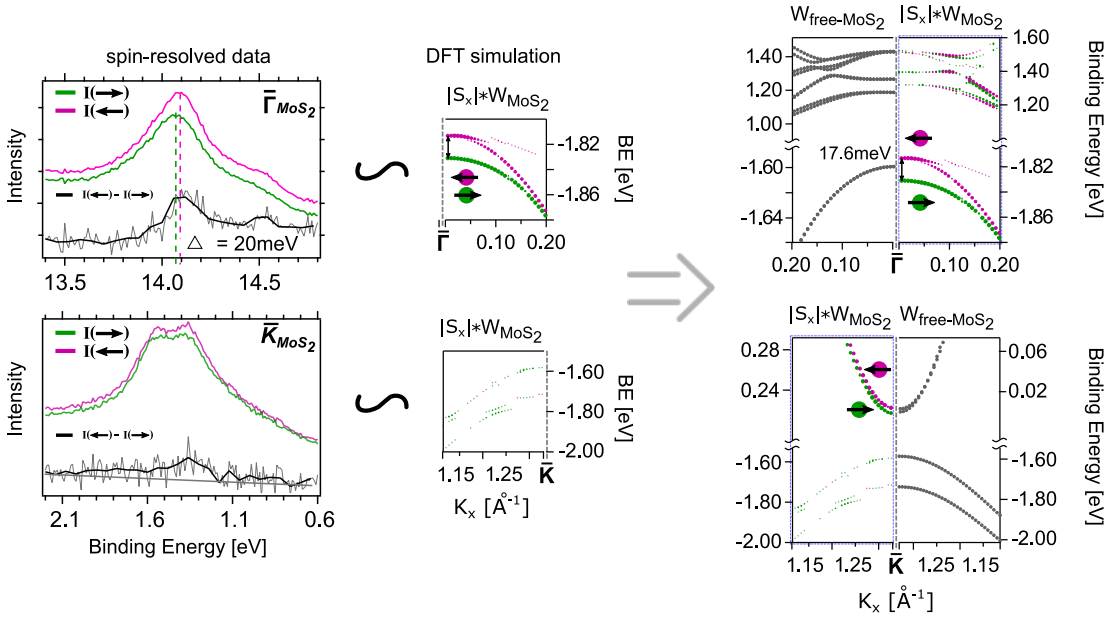

Figure 4.22: Illustration of how spin-resolved photoemission data agree with DFT calculations near $\overline{\Gamma}$ (top) and $\overline{K}$ (bottom) points in the valence band and the following assumption that DFT calculations correctly predict the band structure in the conduction band.

MoS_2 monolayer (right).

It is worth repeating that we can consider in the MoS_2 monolayer the valence band states to be out-of-plane, and the conduction band states to be in-plane spin polarized. In Fig. 4.23(right) one can see possible optical transitions given spin-valley locking. In Fig. 4.23(left), one can see that the spin-valley locking is not in place, as the spin direction of the MoS_2 states in the conduction band has tilted to the in-plane direction. In this case, the spin-up (spin-down) direction can be projected to spin-left and spin-right (in-plane) spin directions. Dark excitons are brightened, and these transitions can be coupled through a single-photon process.

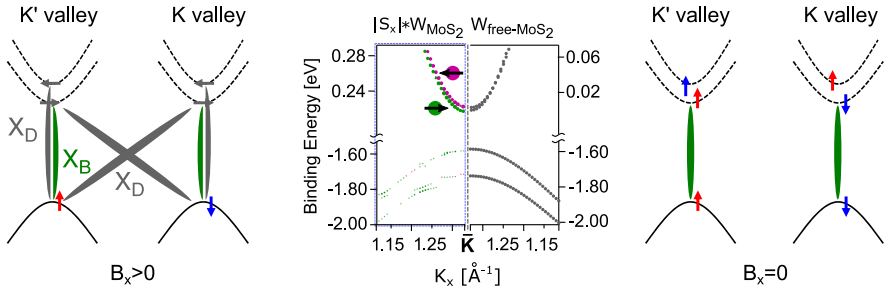

Figure 4.23: Correlation between DFT calculations of the region of $\overline{K}$ and $\overline{K'}$ points in the valence and conduction band and corresponding optical properties.

It is also worth repeating that the electronic gap differs from the optical gap. The optical gap is determined by the energy of the exciton. The exciton is a quasi-particle

that is defined by a many-body interaction between an electron-hole (a many-body interaction itself) and an electron with corresponding electron-hole and electron-electron interactions. The corresponding dark and bright exciton binding energies nicely illustrate such a difference. Looking at Fig. 4.23(left) one can assume that the dark exciton should feature a higher binding energy, however, optical experiment presented in Fig. 4.20(b) from the [15] publication tells the opposite: the MoS_2 monolayer dark exciton in an in-plane magnetic field features lower binding energy than the bright one.

4.4.4 Relation of out-of-plane spin-structure obtained from DFT to optical properties

In Fig. 4.24(middle), one can see the comparison of DFT simulations of electronic and spin structure of MoS_2/graphene/Co with out-of-plane magnetised Co film (left) and free-standing MoS_2 monolayer (right). In the case of the free-standing MoS_2 monolayer in the absence of magnetic field the exciton energies in $\overline{\mathrm{K}}$ and $\overline{\mathrm{K}'}$ valleys are predictably the same (see Fig. 4.24(right)). Oppositely, due to interaction with the magnetized Co film (magnetic proximity effect) the gap in MoS_2 monolayer states at $\overline{\mathrm{K}}$ and $\overline{\mathrm{K}'}$ points becomes different (Fig. 4.24(middle-left)) which can affect the exciton energies in $\overline{\mathrm{K}}$ and $\overline{\mathrm{K}'}$ valleys, in particular the valley splitting, which is illustrated in Fig. 4.24(left))

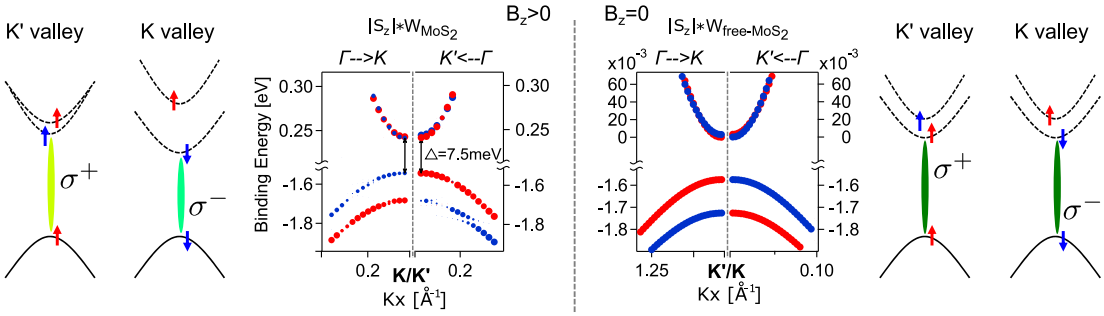

Figure 4.24: Correlation between DFT calculations of the region of $\overline{\mathrm{K}}$ and $\overline{\mathrm{K}'}$ points in the valence and conduction band and corresponding optical properties: the energy splitting of the excitons from $\overline{\mathrm{K}}$ and $\overline{\mathrm{K}'}$ valleys due to Zeeman shifts of electronic states. The Δ=7.5 meV represents the band gap energy difference between $\overline{\mathrm{K}}$ and $\overline{\mathrm{K}'}$valleys.

It is worth mentioning again that the electronic gap is not the same as the optical gap. Therefore the presented results can be considered rather like evidence of a magnetic proximity effect and prediction of an exciton valley splitting, than a precise prediction of the numeric value of the exciton valley splitting.

4.4.5 g-factor *vs* effective magnetic field

In this section, we will discuss why we cannot use the term "magnetic g-factor" but instead rely on the term "an effective magnetic field".

The magnetic g-factor is used to describe the linear dependence of an energy shift depending on the value of an applied external magnetic field:

$$\Delta E_Z = g_X \mu_B B_{ext},$$

where μ_B is the Bohr magneton, g_X is the effective exciton g-factor, and B_{ext} is an external magnetic field.

If one plots the energy shift against applied magnetic field, the slope of this line would represent the g-factor. However, we do not apply any external magnetic field but rather use a permanently magnetized Co thin film and rely on the magnetic proximity effect. In other words, we expect the substrate with an already established magnetic order to share this property with the MoS_2 monolayer placed in close proximity.

As no external magnetic field is present, we cannot rely on its value. In order to numerically estimate the order of magnitude of investigated effect, we would use the term: "an effective magnetic field." When considering an effective magnetic field, we compare a particular magnetic effect that can be measured or calculated in the MoS_2/graphene/Co system (with magnetized Co film) and free-standing MoS_2 monolayer in an external magnetic field. Suppose this effect is similar for both systems. In that case, we can say that the magnetic proximity effect in MoS_2/graphene/Co results in a similar outcome as a particular value of an external magnetic field in MoS_2 monolayer. For simplicity, we can also say that the magnetic proximity effect in MoS_2/graphene/Co features a particular effective magnetic field (the same as for free-standing MoS_2 monolayer in an external magnetic field).

The magnetic proximity effect is more complex than a simple external magnetic field. The magnetic proximity effect can depend on the region in the k-space, as electronic states from different materials can interact differently in different areas of the k-space. It is the case in our MoS_2/graphene/Co system: the magnetic proximity effect features an effective magnetic field of 100 T in the region of $\overline{\Gamma}$ and only of 80 T in the region of $\overline{\mathrm{K}}$ in the valence band.

Determining an effective magnetic field, we compare two parameters:
(1) the Zeeman shift of the electronic states in our MoS_2/graphene/Co system and free-standing MoS_2 in an external magnetic field ($\overline{\Gamma}$ point in the valence band for in-plane and out-of-plane magnetic field and $\overline{\mathrm{K}}$ point in both valence and conduction band for only out-of-plane magnetic field)
(2) The spin-direction canting from out-of-plane to in-plane direction in our MoS_2/graphene/Co system and free-standing MoS_2 in an external magnetic field ($\overline{\mathrm{K}}$ point in both valence and conduction band for only in-plane magnetic field).

In the case (1) for the in-plane magnetic proximity effect, we both experimentally and theoretically determine that for the system MoS_2/graphene/Co in the region of $\overline{\Gamma}$ point valence band, the electronic states split by approximately 20 meV. In order

to reach the same splitting in the free-standing MoS_2 monolayer, one should apply an external magnetic field of about 100 T.

In the (2) case for the in-plane magnetic proximity effect, we both experimentally and theoretically determine that for the system MoS_2/graphene/Co in the region of $\overline{K}$ point the spin of the electronic states in the valence band is canted by 15% to the in-plane direction. In order to reach the same canting in the free-standing MoS_2 monolayer, one should apply an external magnetic field of about 80 T.

Similarly, in the case (1) for the out-of-plane magnetic proximity effect, we theoretically determine 20 meV energy splitting in the region of the $\overline{\Gamma}$ point (which corresponds to about 100 T of effective magnetic field) and 7.5 meV splitting of the gap for $\overline{K}$ and $\overline{K'}$ valleys (which corresponds to about 15 T of the effective magnetic field from experimental results[13]).

Given all the values for the effective magnetic field above, one can see why the magnetic proximity effect is so interesting. Of course, the magnetic field from 7 T to 65 T is reachable in experimental setups. However, such fields require superconductive coils and liquid He temperatures. The magnetic proximity effect is cheaper and more realistic in triggering the mentioned magnetic effects. Moreover, the combination of magnetic proximity and an external magnetic field can achieve effective field values beyond each of the approaches. For further development of the method, one can use a stronger than Co-film magnets (e.g., 2D magnets).

4.5 Transfer of the magnetic proximity effect

In the current study, we investigated the possibility of a magnetic proximity effect in MoS_2/graphene/Co from magnetized Co film to MoS_2 monolayer. We used a Co thin film substrate, as it is a classic ferromagnetic material, and one can produce graphene film on it. We initially used graphene between MoS_2 and Co film for two reasons. First, it was known that the MoS_2 monolayer could be grown on a graphene monolayer[56] via MBE technology. Second, we planned to continue our study in the optical domain by performing photoluminescence studies. We knew that direct contact between MoS_2 and Co film would quench the photoluminescence signal; therefore, the graphene is needed to separate MoS_2 from Co.

Spin-resolved measurements and DFT calculations have shown that the MoS_2/graphene/Co system indeed demonstrates the magnetic proximity effect. In other words, Co thin film induces some ferromagnetic properties in the MoS_2 monolayer. The remaining question is the role of graphene in the transfer. The experimental results cannot answer this question alone, because a controlled experiment without graphene is not possible. Moreover, we cannot physically remove the graphene from the experimental system, as the possibility of synthesizing MoS_2/Co remains questionable. The metadata from

DFT simulations suggests that graphene electronic states mix with both Co and MoS_2 states. This suggests that graphene mediates the magnetic proximity effect.

The DFT simulation is more a numerical experiment than a theory; it cannot provide a theoretical explanation of the role of the graphene. However, we can tune this numerical experiment to get more insights. In doing so, we performed DFT simulations of several "hypothetical" systems. Using the term "hypothetical," we refer to the fact that these systems may not exist outside the simulation and should be treated as numerical models. Because of time constraints, we used different simulation packages (FPLO, OpenMX, Wien2k). However, we carefully checked that the results obtained in different programs are consistent with those obtained from the initially used FPLO package. The DFT results are summarized in the table below:

system	splitting (meV)			Co to MoS_2
	FPLO	WIEN2k	OpenMX	distance (Å)
MoS_2/graphene/Co	17.6	14	15	5.44
MoS_2/vacuum/Co		0.2	4	5.44
MoS_2/*h*-BN/Co			14	5.44
MoS_2/graphene bilayer/Co			0.5	8.79
MoS_2/Co			67	3.31
MoS_2/Cu/Co			66	5.44

Table 4.1: DFT-simulated splitting of the MoS_2 states at the $\overline{\Gamma}$ point for a set of different systems. The splitting characterizes the strength of the magnetic proximity effect. MoS_2/graphene/Co was used as the basis for the calculations of other systems as follows: MoS_2/vacuum/Co - graphene was replaced by vacuum, and MoS_2-Co distance was not changed. MoS_2/*h*-BN/Co - the graphene was replaced by *h*-BN, no distances were changed. MoS_2/graphene bilayer/Co - MoS_2-graphene and graphene-Co distances were kept the same, graphene-graphene relative planar position and interlayer distance were taken similar to carbon layers in graphite - 3.35ÅṀoS$_2$/Co - the graphene was erased from the system, MoS_2-Co distance was set to 3.28Å to keep MoS_2 quasi-free-standing. MoS2/Cu/Co - Cu atoms replaced the graphene; none of the distances were changed to the original cell.

4.5.1 The role of graphene in mediating the magnetic proximity effect

We considered a unit cell with empty space instead of graphene in MoS_2/graphene/Co; the MoS_2-Co distance was not changed. In order to compare the value of the magnetic proximity effect, we compared the spin splitting of MoS_2 states at the $\overline{\Gamma}$ point among different systems. The spin splitting value in MoS_2/vacuum/Co resulted in being almost four times smaller than in MoS_2/graphene/Co system. This implies that **graphene mediates mixing between Co and MoS_2 states**. Surprisingly, we have not observed any Co film-induced modifications in the graphene spin structure. One should note that a similar effect can be observed in a DFT study of the Li/graphene/Si/Co system, where the Li layer deposited on top of graphene intercalates underneath graphene, and the Li/Si interface becomes efficiently magnetized.[145].

4.5.2 Replacing graphene with *h*-BN monolayer

Is graphene something unique that can mediate the magnetic proximity effect? The first aspect that comes to mind is the band structure. In order to determine the role of the graphene band structure, we compared the spin splitting value of two similar systems: MoS_2/graphene/Co and MoS_2/*h*-BN/Co. We used similar unit cells where graphene was simply replaced by *h*-BN, the MoS_2-Co distance was not changed. While quasi-free-standing graphene features a zero-gap band structure, *h*-BN possesses a wide band gap exceeding the gap of MoS_2. While quasi-free-standing graphene states overlap in energy with the top of the MoS_2 valence band, *h*-BN states do not. However, the DFT simulations demonstrate a similar value of the splitting at the $\overline{\Gamma}$ point for both graphene and *h*-BN-containing systems. Therefore, the graphene band structure most probably does not play a significant role in the magnetic proximity effect.

Remark 1: graphene and MoS_2 monolayer feature different lattice constants. Investigating the LEED pattern of the MoS_2/graphene/Co system, we determined a four to five superstructures (four MoS_2 to five graphene unit cells). We included this parameter in the DFT calculations. Four to five MoS_2 to graphene superstructure implies that graphene electronic states overlap with different regions of the MoS_2 electronic states in the first, the second, the third, the fourth, and the fifth Brillouin zones. In brief, this implies that graphene π-states overlap with the MoS_2 top valence band at almost every K (momentum) value. It is worth noticing that in the real MoS_2/graphene/Co, the structure is even more complicated: STM studies show that the structure may not be periodic. This suggests that the graphene band dispersion does not play a significant role in the magnetic proximity effect – only the energy overlap should be taken into account.

Remark 2: the MoS_2/*h*-BN/Co system is not quasi-free-standing. DFT calculations in the work [146] suggest that in the *h*-BN/Co system, *h*-BN states are modified by hybridization with Co states. This results in a partial B and N DOS inside the *h*-BN band gap. Given a similar four to five superstructure, this additional density of *h*-BN states can overlap in energy with the MoS_2 states of interest and play a role in magnetic proximity effect.

4.5.3 The graphene efficiency in mediating the proximity effect and its alternatives

By now, we understand that graphene and *h*-BN in some way mediate the magnetic proximity effect. However, we do not know how efficiently they do so. To answer that, we erased graphene from MoS_2/graphene/Co and moved the MoS_2 monolayer closer to the Co substrate. The spin splitting value at the $\overline{\Gamma}$ point and, therefore, the proximity effect increased by a factor of four. Both graphene and *h*-BN mediate the magnetic proximity effect, but they do it with significant losses.

Next, we aim to estimate how the magnetic proximity effect would decrease if we increase the distance between the MoS_2 and the Co films. We replaced graphene in MoS_2/graphene/Co with a graphene bilayer keeping the graphene-MoS_2 and graphene-Co distances the same and using a graphene-graphene distance similar to the one in graphite. The spin splitting value at the $\overline{\Gamma}$ point decreases, almost reaching zero. It seems that graphene-graphene magnetic proximity transfer is inefficient.

In the framework of photoemission experiments and DFT calculations, we study the magnetic proximity effect through the lens of interacting electronic states: electronic states can hybridize and mix. Graphene has only one electron in the $2p_z$ orbital, which can efficiently interact with the electron in a near material, such as Co or MoS_2. Will more electrons increase the efficiency of magnetic proximity effect transfer? Copper feature a larger radius of high density of electronic states as well as a higher number of valence electrons than carbon; we replaced graphene with a copper layer (keeping the same MoS_2–Co distance). The spin splitting value at the $\overline{\Gamma}$ point increases, reaching the value for the MoS_2/Co system without any buffer layer.

Remark. Using Cu monolayer instead of graphene, we have made a few incorrect assumptions: we just replaced carbon atoms with Cu(111) monolayer, not changing any distances; we also did not relax the MoS_2/Cu/Co system. One should not consider the MoS_2/Cu/Co system as a potentially real one: we have reasonable doubts that it can be experimentally produced via MBE method.

4.6 K-doped MoS_2/graphene/Co system

4.6.1 Electron doping with K atoms

ARPES is a powerful technique that only provides information on the occupied electronic states of a material. However, many electronic and optical applications are closely related to the physics of quasi-particle transitions between valence and conduction bands. In order to gather additional information about unoccupied states of the MoS_2/graphene/Co system, we employed electron doping using alkali metal deposition. This method is well established for many 2D materials and successfully works for TMDCs (MoSe Shen) and MoS_2, in particular[56]. Following previous works, we used K as an electron donor.

The electron configuration of the atomic K atom is $[Ar]4s^1$, where [Ar] represents a fully occupied electron shell. The $4s^1$ is the only electron in the fourth electron shell and can be easily donated. The deposition of K atoms is somewhat similar to the electrostatic gating of a material. As a result of electron transfer from K to MoS_2/graphene/Co, a surface dipole is formed between K^+ and the system. The interface effective electric field may reach colossal values because of the very small distance, and sometimes it

leads to an electron mass and band gap renormalization. Thus ARPES derived values often differ from those defined by DFT calculations.

We used commercially available K getters (SAES) to perform *in-situ* deposition. The amount of material was controlled by a quartz microbalance, and the sample was annealed after the deposition. In a multilayer system such as MoS_2/graphene/Co, K atoms can occupy different positions: on top of MoS_2, intercalated between MoS_2 and graphene, intercalated between graphene and Co, or a combination of all. As we will discuss later, different K atom end-locations depend on several parameters: the amount of deposited K atoms and their rate, the substrate temperature during deposition, the annealing temperature of the substrate after K deposition, the exposure time to the synchrotron radiation during measurements at room temperature. Annealing the system up to 600°C resulted in a complete recovery of the MoS_2/graphene/Co system to the state before deposition of K atoms. This fact allowed us to perform K atom deposition multiple times and investigate the range of possible outcomes. It also allowed us to use the very same MoS_2/graphene/Co sample for ARPES and spin-resolved ARPES studies in different vacuum chambers and to secure the reproducibility of the results.

4.6.2 Phase diagram of K doped MoS_2/graphene/Co

The initial approach was to deposit K atoms in high-vacuum conditions atop the MoS_2/graphene/Co system to investigate the electronic and spin structure of the conduction band states of the MoS_2 monolayer. However, the K atoms participate in various types of doping of both MoS_2 and graphene monolayers. In Fig. 4.25 and Fig. 4.26 we summarize all observed configurations of MoS_2 and graphene doping, respectively. Additional electrons donated by K atoms may be distributed between graphene and MoS_2 in several forms: e-doped MoS_2 and pristine graphene; e-doped graphene (with different doping levels) and pristine MoS_2; and combinations of both. Intriguingly, we did not observe a phase when MoS_2 and graphene simultaneously have the highest doping level. We attribute such a rich phase diagram to multiple possible positions of the K atom in the interface.

Electron doped MoS_2 features two stable configurations: undoped or pristine (Fig. 4.25(a)) and maximally doped (Fig. 4.25(c). These two states differ by 0.39 eV Fermi energy shift. Fig. 4.25(b) presents the intermediate state where both doping configurations can be found. The phase with maximum doping features a pronounced electron pocket at the $\overline{\mathrm{K}}$ point with an extra intensity shoulder separated by a small energy gap. This peak-deep-hump structure corresponds to inelastic scattering processes during photoemission, and in the case of metallic TMDCs (e.g., $TaSe_2$), it is often related to a surface plasmon. Considering the vast similarity in appearance and the energy loss, we attribute this feature to plasmon-related loss states. We estimate the gap size to be ∼1.66 eV which corresponds to previously reported results[56].

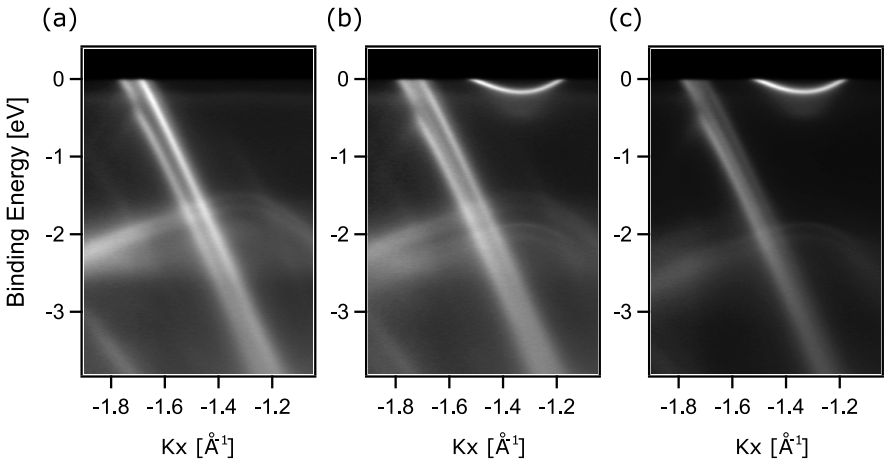

Figure 4.25: Two types of MoS_2 doping by K atoms observed in ARPES data taken in the region of MoS_2 and graphene $\overline{K}$ points in the Brillouin zone. (a) undoped MoS_2 monolayer. (b) the composition of undoped and electron-doped MoS_2 monolayers in a single data set. (c) only electron-doped MoS_2 monolayer. The Fermi Energy shift between MoS_2 doped and undoped states is 0.39 eV.

In contrast to the MoS_2 case, the phase diagram of the graphene doping shows multiple possible configurations. There is a continuous range between maximally (Dirac point at 1.2 eV) doped and a pristine state (Dirac point above the Fermi level) as presented in Fig. 4.26. Apart from the pristine state, other configurations appear simultaneously, and the doping level depends only on the local concentration of K atoms. Some of the observed phases were not stable under synchrotron radiation from the beamline (probably, light/heat induced phase transition). The different behavior of graphene in comparison to MoS_2 is related to its gap-less nature. The chemical potential smoothly moves with an increase of extra electrons, while in the case of gapped states, it first jumps to the bottom of the conduction band. Another reason for a different phase diagram is related to the structural properties of the interface.

Angular resolved XPS (ARXPS) is a powerful method to characterize layered interfaces. We attempt to gain insight into the K atom position for the abovementioned phases. However, in the case of a multilayer system such as MoS_2/graphene/Co ARXPS failed to provide solid conclusions, especially for the mixed phase. The cartoon picture 4.27 presents all possible positions where K atoms potentially may be found: (a) - atop the MoS_2 monolayer, (b) atop a graphene monolayer which is not covered by MoS_2 monolayer islands, (c) in between MoS_2 and graphene monolayers, and (d) under the graphene monolayer. Cases (a),(b) and (b),(c) potentially can coexist because the MoS_2 monolayer is not complete. This fact complicates the interpretation of AR-XPS data. Nevertheless, we found that the phase with doped MoS_2 is stable to exposure to the atmosphere. Thus we can exclude an atop position in this case. Intercalation of K under graphene is expected to provide less charge transfer to MoS_2 than to graphene.

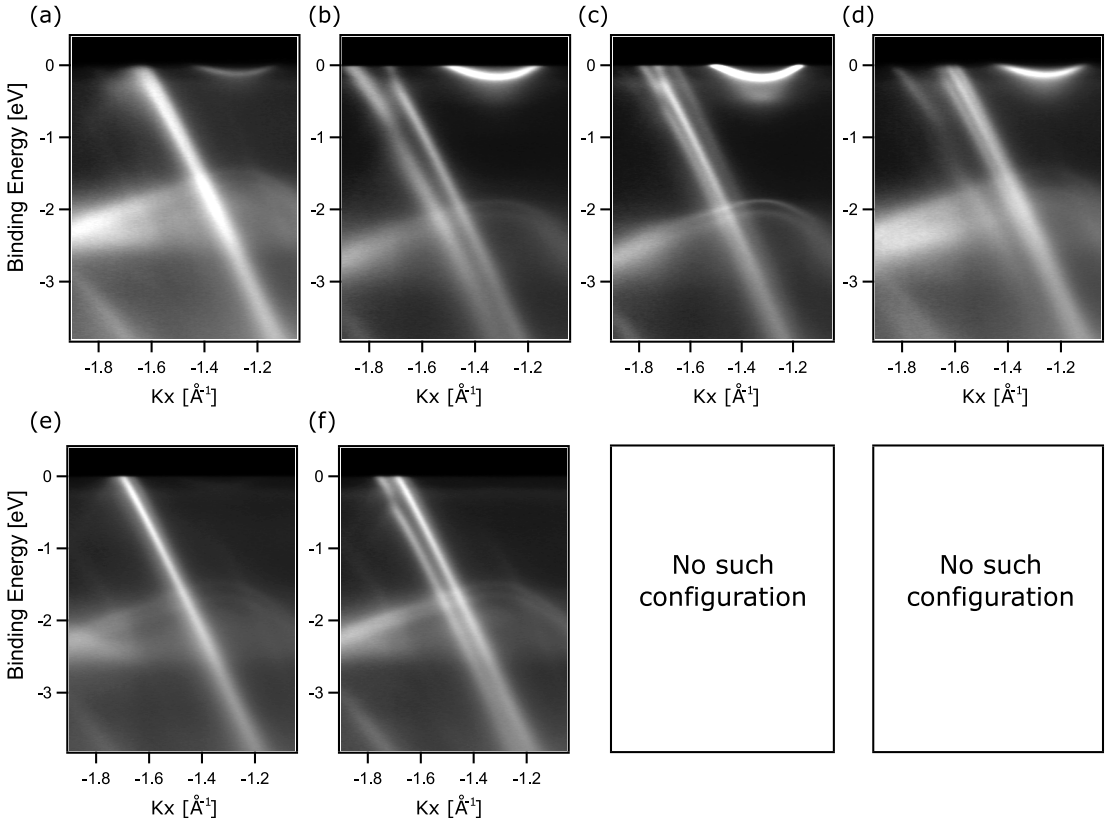

Figure 4.26: Different types of graphene doping by K atoms observed in ARPES data taken in the region of MoS_2 and graphene $\overline{K}$ points in the Brillouin zone in the direction of $\overline{\Gamma}$-$\overline{K}$: first (a–d) and the second (e,f) rows present ARPES data with doped and undoped MoS_2 monolayers respectively. Several types of graphene π states represent different stages of graphene monolayer doping: (a) slight unresolvable electron doping; (b) $\sim$ 0.78 eV and $\sim$ 0.11 eV electron doping; (c) $\sim$ 0.5 eV, $\sim$ 0.11 eV, and almost no electron doping; (d) $\sim$ 1.2 eV, $\sim$ 0.37 eV, $\sim$ 0.11 eV, and almost no electron doping; (e) almost no electron doping with blur in both energy directions; (f) $\sim$ 0.34 eV and almost no electron doping with blur towards lower binding energy.

Therefore, the heavily doped MoS_2 phase most probably corresponds to K intercalation between MoS_2 and graphene. This scenario also can explain the absence of pure heavily doped graphene: K atoms intercalated between MoS_2 and graphene create an electrostatic field preventing further K accumulation in the deeper layer and only regions free of MoS_2 become fully doped. The intercalation of the full layer under graphene (d) is either not feasible or corresponds to an unstable phase because one expects to observe two well-defined doping levels for graphene in the presence of doped or pristine MoS_2. Our study suggests that the doping level of graphene is rather not well defined.

In summary, K and MoS_2/graphene/Co have a rich phase diagram where the MoS_2 monolayer is represented in two states, and there is a continuum of configurations of the graphene monolayer. The most stable phase is related to the heavily doped MoS_2

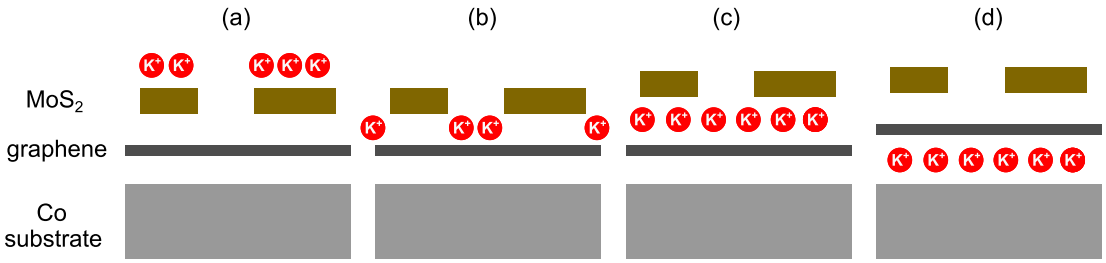

Figure 4.27: Cartoon pictures of possible locations of K^+ ions in the MoS_2/graphene/Co system. (a) K^+ is atop MoS_2 monolayer islands. (b) K^+ is atop a graphene monolayer not covered by MoS_2 islands. (c) K^+ is between MoS_2 and graphene monolayers. (d) K^+ is underneath the graphene monolayer.

monolayer and pristine graphene, where K atoms are most probably located between graphene and MoS_2.

4.6.3 K-doped MoS_2/graphene/Co system: spin resolved measurements

Electron doping of the MoS_2 monolayer provides access for ARPES to probe the conduction band states and change the distance to the Co substrate (in the case of K atoms intercalation). Both facts make the system interesting in the context of the magnetic proximity effect. Our DFT calculations predicted the strongest effect of Co magnetization on the MoS_2 states in the conduction band. We reproduced the most stable phase of K-doped MoS_2/graphene/Co. In order to obtain such a system, one needs to deposit more than one monolayer of K atoms under room temperature and then anneal the system up to 350°C.

Fig. 4.28 represents ARPES data of the doped MoS_2/graphene/Co system, where the MoS_2 monolayer is fully doped, and graphene is not. The splitting of MoS_2 valence band states is not as clear as previously shown in Fig. 4.26(b,c) because here we performed measurements at room temperature. Fig. 4.28(b) shows a Fermi surface of MoS_2 conduction band states in the region of the MoS_2 $\overline{K}$ point, where the Fermi surface area is $\sim 0.13 Å^{-2}$. This corresponds to a 0.11 e/per unit cell doping value. As mentioned above, this phase features undoped graphene, as displayed in fig. 4.28(d)

To estimate the effect of K doping on the magnetic proximity effect we recorder spin-resolved spectra in several regions of the MoS_2 monolayer band structure: $\overline{\Gamma}$ point in the valence band (Fig. 4.29(a)), $\overline{\Gamma}$ point in the valence band (Fig. 4.29(b)), and $\overline{K}$ point in the conduction band (Fig. 4.29(c)).

Before the K doping, the proximity effect resulted in the splitting of the states in the $\overline{\Gamma}$ point and the appearance of in-plane spin polarization in the $\overline{K}$ point. Fig. 4.29(a,a') show spin-resolved data for MoS_2 valence band states in the region of the $\overline{\Gamma}$ point. The out-of-plane direction shows no spin polarization as before the K deposition (see section

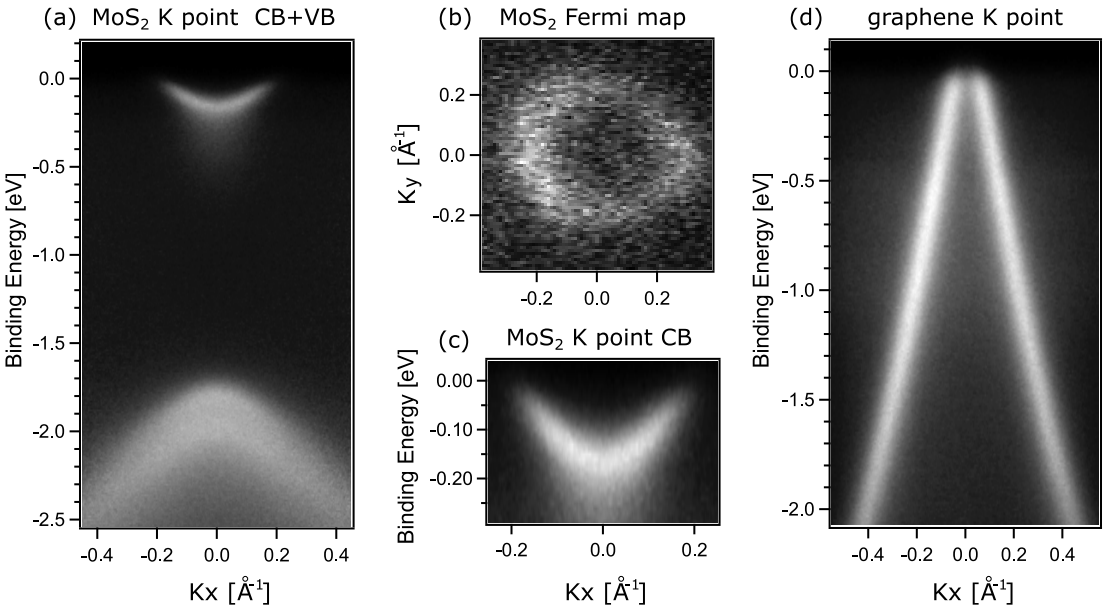

Figure 4.28: The ARPES data of the K doped MoS_2/graphene/Co system. (a) MoS_2 monolayer valence band (VB) and conduction band (CB) states in the region of MoS_2 $\overline{K}$ point measured perpendicular to the $\overline{\Gamma}$-$\overline{K}$ direction. (b) Fermi surface map of MoS_2 monolayer conduction band (CB) states in the region of MoS_2 $\overline{K}$ point. (c) Zoomed in (a) data-set in the region of MoS_2 monolayer conduction band states. (d) graphene monolayer valence band states in the region of graphene $\overline{K}$ point measured perpendicular to the $\overline{\Gamma}$-$\overline{K}$ direction. MoS_2 features 0.39 eV electron doping, while graphene shows 0.12 eV electron doping. The band gap between valence and conduction band states in MoS_2 is ∼1.66 eV. The Fermi surface area of electron-doped MoS_2 monolayer is ∼0.05Å^{-2}

4.2.5). Intriguingly, the in-plane channel also shows an absence of a spin-polarization, contrasting the spin split states observed before the K doping. In Fig. 4.29(b,b') spin-resolved spectra for MoS_2 valence band states in the region of $\overline{K}$ point are presented. Similar to the $\overline{\Gamma}$ point, the spin polarization for the out-of-plane direction remains featureless. However, unlike the $\overline{\Gamma}$ point region, the proximity effect in the region of the MoS_2 $\overline{K}$ point in the valence band seems more pronounced than in the undoped MoS_2/graphene/Co system. As discussed in the previous section, the states of overlap Co and Mo states is important for the proximity effect. K intercalation simultaneously increases the Co - MoS_2 distance and shifts the energy position of the MoS_2 states. This somewhat favors the overlap of MoS_2 and Co states in the vicinity of the $\overline{K}$ and completely blocks it at the $\overline{\Gamma}$ point.

While the magnetic proximity effect is modified by K intercalation, the spin texture of the MoS_2 conduction band still provides valuable information. In Fig. 4.29(c,c') spin-resoled data are presented. According to our DFT calculations for the undoped system, the energy splitting between two bands is about 5 meV (or even less). However, both in-plane and out-of-plane spin-resolved spectra do not show noticeable polarization. Most

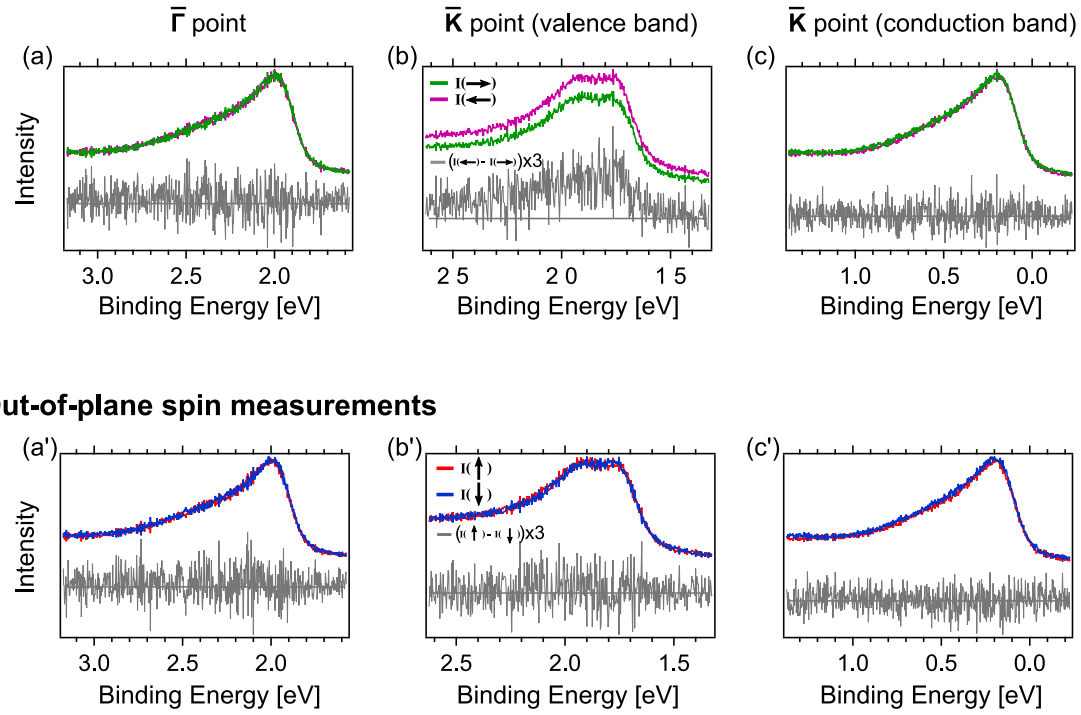

Figure 4.29: Spin-resolved photoemission results of K doped MoS_2/graphene/Co system. The first row (a-c) represents the in-plane spin measurements, and the second row (a'-c') – the out-of-plane ones. (a,a') correspond to energy-momentum cut in the region of $\overline{\Gamma}$; (b,b') (c,c') correspond to valence and conduction band states in the region of $\overline{K}$ respectively. Green and purple colors correspond to opposite spin directions in the in-plane direction, while red and blue correspond to opposite spin direction in the out-of-plane direction. The noisy grey curve underneath all spectra corresponds to the difference between two spectra of opposite spin directions.

probably, DFT overestimated the energy splitting for the states in the conduction band, and it remains below the energy resolution of the current experimental study (we can observe the energy split of 20 meV of the states with an opposite spin, but it is beyond our reach to observe the splitting of less than 20 meV).

In summary, K-doping results in the absence of the magnetic proximity effect manifestation in the regions of MoS_2 monolayer $\overline{\Gamma}$ point in the valence band and $\overline{K}$ point in the conduction band states. On the other hand, the energy downshifts of the MoS_2 bands somewhat promote the effect in the region of the $\overline{K}$ point in the valence band states.

Summary of chapter 4

We started by confirming that the MoS_2 monolayer in-plane spin structure can be manipulated via interaction with a substrate and investigated a MoS_2 monolayer on a

gold crystal. We predicted a Rashba effect by DFT computations of MoS_2/Au(111) and then confirmed it with spin-resolved ARPES measurements. We attribute the origin of the Rashba effect in MoS_2 to hybridization between MoS_2 and gold valence states. MoS_2 monolayer valence band states gain a Rashba-like spin texture in the regions outside of high symmetry points ($\overline{\Gamma}$, $\overline{K}$, $\overline{M}$) due to symmetry reasons.

After having confirmed the possibility of manipulating the in-plane spin structure of the MoS_2 monolayer, we switched to a more applicable task: control the spin texture via substrate magnetization. We chose graphene/cobalt as a substrate. DFT computations suggest that one can manipulate the MoS_2 spin structure via a magnetic proximity effect. Unlike the Rashba effect, the magnetic proximity effect can change the in-plane spin texture in the region of MoS_2 high-symmetry points: at the $\overline{\Gamma}$ point, an in-plane spin splitting of the valence band is expected, while at the $\overline{K}$ point the valence band states are expected to gain some in-plane spin projection and the conduction band states are expected to gain a 100% in-plane spin polarisation. The latter should drastically change the optical properties of the MoS_2 monolayer.

Spin-resolved ARPES measurements match with DFT predictions: the in-plane Co magnetization results in ≈20 meV MoS_2 valence state spin splitting at the $\overline{\Gamma}$ point and a slight spin canting at the $\overline{K}$ point. Further DFT investigations reveal that the spin canting at the $\overline{K}$ point valence band states comes from a mixture of MoS_2 states with Co states and is localized at Co atoms. In contrast, the 100% in-plane spin polarisation at the conduction band is caused by the exchange interaction and localized in the MoS_2 monolayer. Therefore the optical selection rules are completely changed, and the presence of dark excitons is expected. The DFT study for out-of-plane cobalt magnetization demonstrates ≈16 meV out-of-plane spin splitting at the $\overline{\Gamma}$ point and ≈8 meV spin splitting of $\overline{K}$ and $\overline{K'}$ valleys.

We benchmarked the magnetic proximity effect to an external magnetic field. We estimated the in-plane magnetic proximity effect to cause a similar spin structure modification as 100 T external in-plane magnetic field in the region of the $\overline{\Gamma}$ point and 80 T in the region of the $\overline{K}$ point.

In the MoS_2/graphene/Co system, graphene is buffering the MoS_2 monolayer from the cobalt film. This is necessary for further consideration of this system in optical applications. Given the magnetic proximity effect is present, it is important to understand the role of graphene in its transfer. One may consider electronic band structure and spatial overlap as the main actors. Comparing the magnetic proximity effect in MoS_2/graphene/Co and MoS_2/*h*-BN/Co systems, it is evident that the band structure is not playing the major role. Graphene and *h*-BN are rather similar in that the exchange interaction is mediated by the $2p_z$ orbitals. It seems to be essential which orbitals are involved in the interaction between MoS_2 and Co and how strongly these orbitals overlap. Obviously, only out-of-plane localized orbitals may play a significant

role. Particularly, the effect is almost not present in both MoS_2/graphene bilayer/Co and MoS_2/vacuum/Co systems due to smaller orbital overlap. In contrast, the effect is not suppressed at all in the case of Cu monolayer buffer due to better overlap and higher density of valence states.

In the discussion above, we were able to analyze the MoS_2 conduction band states only by means of computations. In order to fill the MoS_2 conduction band and perform photoemission measurements, we doped the system with K atoms. Spin-resolved measurements showed no in-plane spin splitting neither in the region of the $\overline{\Gamma}$ point in valence band states nor in the region of the $\overline{\mathrm{K}}$ point in conduction band states. We attribute this to two factors: K atoms intercalated underneath the MoS_2 layer increase the distance to the cobalt film, and the MoS_2 band structure has shifted relative to both graphene and Co band structures in energy. On the other hand, the magnetic proximity effect in the region of the $\overline{\mathrm{K}}$ point in valence band states has been promoted by this change.

Bibliography

[1] K. F. Mak, C. Lee, J. Hone, J. Shan, and T. F. Heinz, „Atomically Thin MoS_2: A New Direct-Gap Semiconductor“, *Phys. Rev. Lett.*, vol. 105, p. 136 805, 13 2010 (cit. on pp. iii, 7, 15, 16).

[2] B. Birmingham, J. Yuan, M. Filez, D. Fu, J. Hu, J. Lou, M. O. Scully, B. M. Weckhuysen, and Z. Zhang, „Spatially-Resolved Photoluminescence of Monolayer MoS_2 under Controlled Environment for Ambient Optoelectronic Applications“, *ACS Applied Nano Materials*, vol. 1, no. 11, pp. 6226–6235, 2018 (cit. on pp. iii, 4).

[3] H. Kwon, S. Garg, J. H. Park, Y. Jeong, S. Yu, S. M. Kim, P. Kung, and S. Im, „Monolayer MoS_2 field-effect transistors patterned by photolithography for active matrix pixels in organic light-emitting diodes“, *npj 2D Materials and Applications*, vol. 3, no. 1, 2019 (cit. on p. iii).

[4] C. L. Kane and E. J. Mele, „Quantum Spin Hall Effect in Graphene“, *Phys. Rev. Lett.*, vol. 95, p. 226 801, 22 2005 (cit. on p. iii).

[5] J. R. Schaibley, H. Yu, G. Clark, P. Rivera, J. S. Ross, K. L. Seyler, W. Yao, and X. Xu, „Valleytronics in 2D materials“, *Nature Reviews Materials*, vol. 1, no. 11, 2016 (cit. on pp. iii, 4).

[6] A. Hirohata, K. Yamada, Y. Nakatani, I.-L. Prejbeanu, B. Diény, P. Pirro, and B. Hillebrands, „Review on spintronics: Principles and device applications“, *Journal of Magnetism and Magnetic Materials*, vol. 509, p. 166 711, 2020 (cit. on pp. iii, 4).

[7] T. Cao, G. Wang, W. Han, H. Ye, C. Zhu, J. Shi, Q. Niu, P. Tan, E. Wang, B. Liu, and J. Feng, „Valley-selective circular dichroism of monolayer molybdenum disulphide“, *Nature Communications*, vol. 3, no. 1, pp. 1–5, 2012 (cit. on pp. iii, iv).

[8] D. Xiao, G.-B. Liu, W. Feng, X. Xu, and W. Yao, „Coupled Spin and Valley Physics in Monolayers of MoS_2 and Other Group-VI Dichalcogenides“, *Phys. Rev. Lett.*, vol. 108, p. 196 802, 19 2012 (cit. on p. iii).

[9] E. I. Rashba and V. I. Sheka, „Symmetry of Energy Bands in Crystals of Wurtzite Type II. Symmetry of Bands with Spin-Orbit Interaction Included“, *Fiz. Tverd. Tela: Collected Papers*, vol. 2, pp. 162–76, 1959, English translation published as the supplementary material to the article by Bihlmayer et al 2015 New. J. Phys. 17 050202 [18] (cit. on pp. iii, 66).

[10] A. G. Rybkin, A. A. Rybkina, M. M. Otrokov, O. Y. Vilkov, I. I. Klimovskikh, A. E. Petukhov, M. V. Filianina, V. Y. Voroshnin, I. P. Rusinov, A. Ernst, A. Arnau, E. V. Chulkov, and A. M. Shikin, „Magneto-Spin–Orbit Graphene: Interplay between Exchange and Spin–Orbit Couplings“, *Nano Letters*, vol. 18, no. 3, pp. 1564–1574, 2018 (cit. on pp. iii, 51).

[11] G. Aivazian, Z. Gong, A. M. Jones, R. L. Chu, J. Yan, D. G. Mandrus, C. Zhang, D. Cobden, W. Yao, and X. Xu, „Magnetic control of valley pseudospin in monolayer WSe_2“, *Nature Physics*, vol. 11, no. 2, pp. 148–152, 2015 (cit. on pp. iii, iv, 8).

[12] J. J. Hauser, „Magnetic Proximity Effect“, *Phys. Rev.*, vol. 187, pp. 580–583, 2 1969 (cit. on pp. iii, 8, 12, 92).

[13] Q. Li, X. Zhao, L. Deng, Z. Shi, S. Liu, Q. Wei, L. Zhang, Y. Cheng, L. Zhang, H. Lu, W. Gao, W. Huang, C.-W. Qiu, G. Xiang, S. J. Pennycook, Q. Xiong, K. P. Loh, and B. Peng, „Enhanced Valley Zeeman Splitting in Fe-Doped Monolayer MoS_2“, *ACS Nano*, vol. 0, no. 0, null, 0 (cit. on pp. iii, 8, 12, 90, 97).

[14] D. Usachov, A. Fedorov, M. M. Otrokov, A. Chikina, O. Vilkov, A. Petukhov, A. G. Rybkin, Y. M. Koroteev, E. V. Chulkov, V. K. Adamchuk, A. Grüneis, C. Laubschat, and D. V. Vyalikh, „Observation of Single-Spin Dirac Fermions at the Graphene/Ferromagnet Interface“, *Nano Letters*, vol. 15, no. 4, pp. 2396–2401, 2015, PMID: 25734657 (cit. on pp. iii, 44).

[15] C. Robert, B. Han, P. Kapuscinski, A. Delhomme, C. Faugeras, T. Amand, M. R. Molas, M. Bartos, K. Watanabe, T. Taniguchi, B. Urbaszek, M. Potemski, and X. Marie, „Measurement of the spin-forbidden dark excitons in MoS_2 and $MoSe_2$ monolayers“, *Nature Communications*, vol. 11, no. 1, p. 4037, 2020 (cit. on pp. iv, 9, 91, 92, 95).

[16] U. Bhanu, M. R. Islam, L. Tetard, and S. I. Khondaker, „Photoluminescence quenching in gold - MoS2 hybrid nanoflakes“, *Scientific Reports*, vol. 4, no. 1, p. 5575, 2014 (cit. on p. iv).

[17] P. Garg, R. Laishram, R. Raman, and R. K. Soni, „Photoluminescence Quenching and SERS in Tri-layer MoS_2 Flakes“, *Journal of Electronic Materials*, vol. 48, no. 9, pp. 5883–5890, 2019 (cit. on p. iv).

[18] G. Froehlicher, E. Lorchat, and S. Berciaud, „Charge Versus Energy Transfer in Atomically Thin Graphene-Transition Metal Dichalcogenide van der Waals Heterostructures“, *Physical Review X*, vol. 8, no. 1, pp. 1–15, 2018 (cit. on p. iv).

[19] J. A. Miwa, M. Dendzik, S. S. Grønborg, M. Bianchi, J. V. Lauritsen, P. Hofmann, and S. Ulstrup, „Van der Waals Epitaxy of Two-Dimensional MoS_2–Graphene Heterostructures in Ultrahigh Vacuum“, *ACS Nano*, vol. 9, no. 6, pp. 6502–6510, 2015, PMID: 26039108 (cit. on p. iv).

[20] J. Hall, B. Pielić, C. Murray, W. Jolie, T. Wekking, C. Busse, M. Kralj, and T. Michely, „Molecular beam epitaxy of quasi-freestanding transition metal disulphide monolayers on van der Waals substrates: a growth study“, *2D Materials*, vol. 5, no. 2, p. 025 005, 2018 (cit. on pp. iv, 6, 48, 50).

[21] V. Voroshnin, A. V. Tarasov, K. A. Bokai, A. Chikina, B. V. Senkovskiy, N. Ehlen, D. Y. Usachov, A. Grüneis, M. Krivenkov, J. Sánchez-Barriga, and A. Fedorov, „Direct Spectroscopic Evidence of Magnetic Proximity Effect in MoS $_2$ Monolayer on Graphene/Co“, *ACS Nano*, vol. 16, no. 5, pp. 7448–7456, 2022 (cit. on pp. v, 53).

[22] Q. H. Wang, K. Kalantar-Zadeh, A. Kis, J. N. Coleman, and M. S. Strano, „Electronics and optoelectronics of two-dimensional transition metal dichalcogenides“, *Nature Nanotechnology*, vol. 7, no. 11, pp. 699–712, 2012 (cit. on p. 1).

[23] M. M. Glazov, E. L. Ivchenko, G. Wang, T. Amand, X. Marie, B. Urbaszek, and B. L. Liu, „Spin and valley dynamics of excitons in transition metal dichalcogenide monolayers“, *Physica Status Solidi (B) Basic Research*, vol. 252, no. 11, pp. 2349–2362, 2015 (cit. on pp. 1, 19).

[24] S. H. Sung, N. Schnitzer, L. Brown, J. Park, and R. Hovden, „Stacking, strain, and twist in 2D materials quantified by 3D electron diffraction“, *Phys. Rev. Materials*, vol. 3, p. 064 003, 6 2019 (cit. on p. 1).

[25] M. Chhowalla, H. S. Shin, G. Eda, L.-J. Li, K. P. Loh, and H. Zhang, „The chemistry of two-dimensional layered transition metal dichalcogenide nanosheets“, *Nature Chemistry*, vol. 5, no. 4, pp. 263–275, 2013 (cit. on pp. 1, 3).

[26] M. Xu, T. Liang, M. Shi, and H. Chen, „Graphene-like two-dimensional materials“, *Chemical Reviews*, vol. 113, no. 5, pp. 3766–3798, 2013 (cit. on p. 1).

[27] J. A. Reyes-Retana and F. Cervantes-Sodi, „Spin-orbital effects in metal-dichalcogenide semiconducting monolayers“, *Scientific Reports*, vol. 6, no. 1, p. 24 093, 2016 (cit. on p. 1).

[28] X. Xu, W. Yao, D. Xiao, and T. F. Heinz, „Spin and pseudospins in layered transition metal dichalcogenides“, *Nature Physics*, vol. 10, no. 5, pp. 343–350, 2014 (cit. on p. 1).

[29] T. Cao, G. Wang, W. Han, H. Ye, C. Zhu, J. Shi, Q. Niu, P. Tan, E. Wang, B. Liu, and J. Feng, „Valley-selective circular dichroism of monolayer molybdenum disulphide“, *Nature Communications*, vol. 3, no. 1, p. 887, 2012 (cit. on pp. 1, 4, 7, 17).

[30] A. K. Geim and I. V. Grigorieva, „Van der Waals heterostructures“, *Nature*, vol. 499, no. 7459, pp. 419–425, 2013 (cit. on p. 2).

[31] T. Georgiou, R. Jalil, B. D. Belle, L. Britnell, R. V. Gorbachev, S. V. Morozov, Y.-J. Kim, A. Gholinia, S. J. Haigh, O. Makarovsky, L. Eaves, L. A. Ponomarenko, A. K. Geim, K. S. Novoselov, and A. Mishchenko, „Vertical field-effect transistor based on graphene–WS2 heterostructures for flexible and transparent electronics“, *Nature Nanotechnology*, vol. 8, no. 2, pp. 100–103, 2013 (cit. on p. 2).

[32] A. Kuc, „Low-dimensional transition-metal dichalcogenides“, in *Chemical Modelling*, 2014, pp. 1–29 (cit. on p. 3).

[33] R. F. Frindt, „Single Crystals of MoS $_2$ Several Molecular Layers Thick“, *Journal of Applied Physics*, vol. 37, no. 4, pp. 1928–1929, 1966 (cit. on p. 3).

[34] K. S. Novoselov, D. Jiang, F. Schedin, T. J. Booth, V. V. Khotkevich, S. V. Morozov, and A. K. Geim, „Two-dimensional atomic crystals“, *Proceedings of the National Academy of Sciences*, vol. 102, no. 30, pp. 10 451–10 453, 2005 (cit. on p. 3).

[35] B. Radisavljevic, A. Radenovic, J. Brivio, V. Giacometti, and A. Kis, „Single-layer MoS_2 transistors.“, *Nature nanotechnology*, vol. 6 3, pp. 147–50, 2011 (cit. on p. 3).

[36] K. S. Novoselov, A. K. Geim, S. V. Morozov, D. Jiang, Y. Zhang, S. V. Dubonos, I. V. Grigorieva, and A. A. Firsov, „Electric Field Effect in Atomically Thin Carbon Films“, *Science*, vol. 306, no. 5696, pp. 666–669, 2004 (cit. on pp. 3, 4).

[37] H. Wang, L. Yu, Y.-H. Lee, Y. Shi, A. Hsu, M. L. Chin, L.-J. Li, M. Dubey, J. Kong, and T. Palacios, „Integrated Circuits Based on Bilayer MoS $_2$ Transistors“, *Nano Letters*, vol. 12, no. 9, pp. 4674–4680, 2012 (cit. on p. 3).

[38] J. E. Ayers, *Ayers, J: Digital Integrated Circuits: Analysis and Design*, 2nd edition. Boca Raton: CRC Press, 2009 (cit. on p. 3).

[39] B. Radisavljevic, M. B. Whitwick, and A. Kis, „Integrated Circuits and Logic Operations Based on Single-Layer MoS $_2$“, *ACS Nano*, vol. 5, no. 12, pp. 9934–9938, 2011 (cit. on p. 3).

[40] B. Radisavljevic, M. B. Whitwick, and A. Kis, „Small-signal amplifier based on single-layer MoS $_2$“, *Applied Physics Letters*, vol. 101, no. 4, p. 043 103, 2012 (cit. on p. 3).

[41] O. Lopez-Sanchez, D. Lembke, M. Kayci, A. Radenovic, and A. Kis, „Ultrasensitive photodetectors based on monolayer MoS2“, *Nature Nanotechnology*, vol. 8, no. 7, pp. 497–501, 2013 (cit. on p. 4).

[42] D.-H. Lien, M. Amani, S. B. Desai, G. H. Ahn, K. Han, J.-H. He, J. W. Ager, M. C. Wu, and A. Javey, „Large-area and bright pulsed electroluminescence in monolayer semiconductors“, *Nature Communications*, vol. 9, no. 1, p. 1229, 2018 (cit. on p. 4).

[43] Y. K. Luo, J. Xu, T. Zhu, G. Wu, E. J. McCormick, W. Zhan, M. R. Neupane, and R. K. Kawakami, „Opto-Valleytronic Spin Injection in Monolayer MoS $_2$ /Few-Layer Graphene Hybrid Spin Valves“, *Nano Letters*, vol. 17, no. 6, pp. 3877–3883, 2017 (cit. on p. 4).

[44] M. Xu, T. Liang, M. Shi, and H. Chen, „Graphene-Like Two-Dimensional Materials“, *Chemical Reviews*, vol. 113, no. 5, pp. 3766–3798, 2013 (cit. on p. 4).

[45] C. D. Lokhande, „Chemical deposition of metal chalcogenide thin films“, *Materials Chemistry and Physics*, vol. 27, no. 1, pp. 1–43, 1991 (cit. on p. 5).

[46] K.-K. Liu, W. Zhang, Y.-H. Lee, Y.-C. Lin, M.-T. Chang, C.-Y. Su, C.-S. Chang, H. Li, Y. Shi, H. Zhang, C.-S. Lai, and L.-J. Li, „Growth of Large-Area and Highly Crystalline MoS $_2$ Thin Layers on Insulating Substrates“, *Nano Letters*, vol. 12, no. 3, pp. 1538–1544, 2012 (cit. on p. 5).

[47] C. Zhao, T. Norden, P. Zhang, P. Zhao, Y. Cheng, F. Sun, J. P. Parry, P. Taheri, J. Wang, Y. Yang, T. Scrace, K. Kang, S. Yang, G.-x. Miao, R. Sabirianov, G. Kioseoglou, W. Huang, A. Petrou, and H. Zeng, „Enhanced valley splitting in monolayer WSe_2 due to magnetic exchange field“, *Nature Nanotechnology*, vol. 12, no. 8, pp. 757–762, 2017 (cit. on p. 5).

[48] H. Bergeron, V. K. Sangwan, J. J. McMorrow, G. P. Campbell, I. Balla, X. Liu, M. J. Bedzyk, T. J. Marks, and M. C. Hersam, „Chemical vapor deposition of monolayer MoS $_2$ directly on ultrathin Al $_2$ O $_3$ for low-power electronics“, *Applied Physics Letters*, vol. 110, no. 5, p. 053 101, 2017 (cit. on p. 5).

[49] Y. Shi, W. Zhou, A.-Y. Lu, W. Fang, Y.-H. Lee, A. L. Hsu, S. M. Kim, K. K. Kim, H. Y. Yang, L.-J. Li, J.-C. Idrobo, and J. Kong, „van der Waals Epitaxy of MoS $_2$ Layers Using Graphene As Growth Templates“, *Nano Letters*, vol. 12, no. 6, pp. 2784–2791, 2012 (cit. on p. 5).

[50] A. M. van der Zande, P. Y. Huang, D. A. Chenet, T. C. Berkelbach, Y. You, G.-H. Lee, T. F. Heinz, D. R. Reichman, D. A. Muller, and J. C. Hone, „Grains and grain boundaries in highly crystalline monolayer molybdenum disulphide“, *Nature Materials*, vol. 12, no. 6, pp. 554–561, 2013 (cit. on p. 5).

[51] S. Najmaei, Z. Liu, W. Zhou, X. Zou, G. Shi, S. Lei, B. I. Yakobson, J.-C. Idrobo, P. M. Ajayan, and J. Lou, „Vapour phase growth and grain boundary structure of molybdenum disulphide atomic layers“, *Nature Materials*, vol. 12, no. 8, pp. 754–759, 2013 (cit. on p. 5).

[52] D. Fu, X. Zhao, Y.-Y. Zhang, L. Li, H. Xu, A.-R. Jang, S. I. Yoon, P. Song, S. M. Poh, T. Ren, Z. Ding, W. Fu, T. J. Shin, H. S. Shin, S. T. Pantelides, W. Zhou, and K. P. Loh, „Molecular Beam Epitaxy of Highly Crystalline Monolayer Molybdenum Disulfide on Hexagonal Boron Nitride“, *Journal of the American Chemical Society*, vol. 139, no. 27, pp. 9392–9400, 2017 (cit. on p. 5).

[53] S. G. Sørensen, H. G. Füchtbauer, A. K. Tuxen, A. S. Walton, and J. V. Lauritsen, „Structure and Electronic Properties of *In Situ* Synthesized Single-Layer MoS $_2$ on a Gold Surface“, *ACS Nano*, vol. 8, no. 7, pp. 6788–6796, 2014 (cit. on pp. 5, 37).

[54] S. S. Grønborg, S. Ulstrup, M. Bianchi, M. Dendzik, C. E. Sanders, J. V. Lauritsen, P. Hofmann, and J. A. Miwa, „Synthesis of Epitaxial Single-Layer MoS $_2$ on Au(111)“, *Langmuir*, vol. 31, no. 35, pp. 9700–9706, 2015 (cit. on pp. 5, 37).

[55] P. Yang, S. Zhang, S. Pan, B. Tang, Y. Liang, X. Zhao, Z. Zhang, J. Shi, Y. Huan, Y. Shi, S. J. Pennycook, Z. Ren, G. Zhang, Q. Chen, X. Zou, Z. Liu, and Y. Zhang, „Epitaxial Growth of Centimeter-Scale Single-Crystal MoS $_2$ Monolayer on Au(111)“, *ACS Nano*, vol. 14, no. 4, pp. 5036–5045, 2020 (cit. on pp. 5, 63).

[56] N. Ehlen, J. Hall, B. V. Senkovskiy, M. Hell, J. Li, A. Herman, D. Smirnov, A. Fedorov, V. Y. Voroshnin, G. D. Santo, L. Petaccia, T. Michely, and A. Grüneis, „Narrow photoluminescence and Raman peaks of epitaxial MoS_2 on graphene/Ir(1 1 1)“, *2D Materials*, vol. 6, no. 1, p. 011 006, 2018 (cit. on pp. 6, 7, 38, 48, 50, 64, 73, 74, 76, 97, 100, 101).

[57] H. Yuan, Z. Liu, G. Xu, B. Zhou, S. Wu, D. Dumcenco, K. Yan, Y. Zhang, S.-K. Mo, P. Dudin, V. Kandyba, M. Yablonskikh, A. Barinov, Z. Shen, S. Zhang, Y. Huang, X. Xu, Z. Hussain, H. Y. Hwang, Y. Cui, and Y. Chen, „Evolution of the Valley Position in Bulk Transition-Metal Chalcogenides and Their Monolayer Limit“, *Nano Letters*, vol. 16, no. 8, pp. 4738–4745, 2016 (cit. on p. 6).

[58] W. Lee, Y. Lin, L.-S. Lu, W.-C. Chueh, M. Liu, X. Li, W.-H. Chang, R. A. Kaindl, and C.-K. Shih, „Time-resolved ARPES Determination of a Quasi-Particle Band Gap and Hot Electron Dynamics in Monolayer MoS $_2$“, *Nano Letters*, vol. 21, no. 17, pp. 7363–7370, 2021 (cit. on p. 6).

[59] J. A. Miwa, S. Ulstrup, S. G. Sørensen, M. Dendzik, A. G. Cabo, M. Bianchi, J. V. Lauritsen, and P. Hofmann, „Electronic Structure of Epitaxial Single-Layer ${\mathrm{MoS}}_{2}$“, *Physical Review Letters*, vol. 114, no. 4, p. 046 802, 2015 (cit. on pp. 6, 42).

[60] H. Bana, E. Travaglia, L. Bignardi, P. Lacovig, C. E. Sanders, M. Dendzik, M. Michiardi, M. Bianchi, D. Lizzit, F. Presel, D. De Angelis, N. Apostol, P. Kumar Das, J. Fujii, I. Vobornik, R. Larciprete, A. Baraldi, P. Hofmann, and S. Lizzit, „Epitaxial growth of single-orientation high-quality MoS $_2$ monolayers“, *2D Materials*, vol. 5, no. 3, p. 035 012, 2018 (cit. on pp. 6, 38, 42).

[61] M. Gehlmann, I. Aguilera, G. Bihlmayer, E. Młyńczak, M. Eschbach, S. Döring, P. Gospodarič, S. Cramm, B. Kardynał, L. Plucinski, S. Blugel, and C. M. Schneider, „Quasi 2D electronic states with high spin-polarization in centrosymmetric MoS2 bulk crystals“, *Scientific Reports*, vol. 6, no. 1, p. 26 197, 2016 (cit. on p. 6).

[62] E. Razzoli, T. Jaouen, M.-L. Mottas, B. Hildebrand, G. Monney, A. Pisoni, S. Muff, M. Fanciulli, N. C. Plumb, V. A. Rogalev, V. N. Strocov, J. Mesot, M. Shi, J. H. Dil, H. Beck, and P. Aebi, „Selective Probing of Hidden Spin-Polarized States in Inversion-Symmetric Bulk MoS2“, *Physical Review Letters*, vol. 118, no. 8, p. 086 402, 2017 (cit. on p. 6).

[63] G. Wang, A. Chernikov, M. M. Glazov, T. F. Heinz, X. Marie, T. Amand, and B. Urbaszek, „Colloquium: Excitons in atomically thin transition metal dichalcogenides“, *Reviews of Modern Physics*, vol. 90, no. 2, p. 21 001, 2018 (cit. on pp. 7, 18).

[64] F. Cadiz, E. Courtade, C. Robert, G. Wang, Y. Shen, H. Cai, T. Taniguchi, K. Watanabe, H. Carrere, D. Lagarde, M. Manca, T. Amand, P. Renucci, S. Tongay, X. Marie, and B. Urbaszek, „Excitonic Linewidth Approaching the Homogeneous Limit in MoS2-Based van der Waals Heterostructures“, *Physical Review X*, vol. 7, no. 2, p. 021 026, 2017 (cit. on p. 7).

[65] W. Yao, D. Xiao, and Q. Niu, „Valley-dependent optoelectronics from inversion symmetry breaking“, *Phys. Rev. B*, vol. 77, p. 235 406, 23 2008 (cit. on p. 7).

[66] U. Bhanu, M. R. Islam, L. Tetard, and S. I. Khondaker, „Photoluminescence quenching in gold - MoS2 hybrid nanoflakes“, *Scientific Reports*, vol. 4, no. 1, p. 5575, 2014 (cit. on p. 7).

[67] A. V. Stier, K. M. McCreary, B. T. Jonker, J. Kono, and S. A. Crooker, „Exciton diamagnetic shifts and valley Zeeman effects in monolayer WS2 and MoS2 to 65 Tesla“, *Nature Communications*, vol. 7, no. 1, p. 10 643, 2016 (cit. on p. 8).

[68] A. Srivastava, M. Sidler, A. V. Allain, D. S. Lembke, A. Kis, and A. Imamoğlu, „Valley Zeeman effect in elementary optical excitations of monolayer WSe_2“, *Nature Physics*, vol. 11, no. 2, pp. 141–147, 2015 (cit. on p. 8).

[69] J. Zhou, J. Lin, H. Sims, C. Jiang, C. Cong, J. A. Brehm, Z. Zhang, L. Niu, Y. Chen, Y. Zhou, Y. Wang, F. Liu, C. Zhu, T. Yu, K. Suenaga, R. Mishra, S. T. Pantelides, Z.-G. Zhu, W. Gao, Z. Liu, and W. Zhou, „Synthesis of Co-Doped MoS $_2$ Monolayers with Enhanced Valley Splitting“, *Advanced Materials*, vol. 32, no. 11, p. 1 906 536, 2020 (cit. on p. 8).

[70] K. Zhang, L. Wang, and X. Wu, „Spin polarization and tunable valley degeneracy in a MoS2 monolayer via proximity coupling to a Cr2O3 substrate“, *Nanoscale*, vol. 11, no. 41, pp. 19 536–19 542, 2019 (cit. on p. 8).

[71] Z.-B. Yin, X.-Y. Chen, Y.-P. Wang, and M.-Q. Long, „The magnetic proximity effect at the MoS2/CrI3 interface“, *Journal of Physics: Condensed Matter*, vol. 34, no. 3, p. 035 002, 2021 (cit. on p. 8).

[72] X. Mao, Z. Liu, J. Li, C. Li, S. Teng, Y. Liu, and X. Xu, „Induced valley and spin splitting in monolayer MoS2 by interfacial magnetic proximity of half-Heusler LiBeN substrate“, *Journal of Magnetism and Magnetic Materials*, vol. 512, p. 167 061, 2020 (cit. on p. 8).

[73] A. O. Slobodeniuk and D. M. Basko, „Spin–flip processes and radiative decay of dark intravalley excitons in transition metal dichalcogenide monolayers“, *2D Materials*, vol. 3, no. 3, p. 035 009, 2016 (cit. on pp. 8, 92).

[74] T. Deilmann and K. S. Thygesen, „Dark excitations in monolayer transition metal dichalcogenides“, *Physical Review B*, vol. 96, no. 20, pp. 1–5, 2017 (cit. on p. 8).

[75] E. Malic, M. Selig, M. Feierabend, S. Brem, D. Christiansen, F. Wendler, A. Knorr, and G. Berghäuser, „Dark excitons in transition metal dichalcogenides“, *Phys. Rev. Materials*, vol. 2, p. 014 002, 1 2018 (cit. on p. 8).

[76] J. P. Echeverry, B. Urbaszek, T. Amand, X. Marie, and I. C. Gerber, „Splitting between bright and dark excitons in transition metal dichalcogenide monolayers“, *Physical Review B*, vol. 93, no. 12, pp. 1–5, 2016 (cit. on p. 8).

[77] F. Hund, *Linienspektren und Periodisches System der Elemente*. Vienna: Springer Vienna, 1927 (cit. on p. 9).

[78] W. Heisenberg, „Zur Theorie des Ferromagnetismus“, *Zeitschrift für Physik*, vol. 49, no. 9, pp. 619–636, 1928 (cit. on p. 10).

[79] M. A. Ruderman and C. Kittel, „Indirect Exchange Coupling of Nuclear Magnetic Moments by Conduction Electrons“, *Physical Review*, vol. 96, no. 1, pp. 99–102, 1954 (cit. on p. 11).

[80] T. Kasuya, „A Theory of Metallic Ferro- and Antiferromagnetism on Zener's Model“, *Progress of Theoretical Physics*, vol. 16, no. 1, pp. 45–57, 1956 (cit. on p. 11).

[81] K. Yosida, „Magnetic Properties of Cu-Mn Alloys“, *Physical Review*, vol. 106, no. 5, pp. 893–898, 1957 (cit. on p. 11).

[82] V. L. Korenev, I. A. Akimov, S. V. Zaitsev, V. F. Sapega, L. Langer, D. R. Yakovlev, Y. A. Danilov, and M. Bayer, „Dynamic spin polarization by orientation-dependent separation in a ferromagnet–semiconductor hybrid“, *Nature Communications*, vol. 3, no. 1, p. 959, 2012 (cit. on p. 12).

[83] A. I. Buzdin, „Proximity effects in superconductor-ferromagnet heterostructures“, *Rev. Mod. Phys.*, vol. 77, pp. 935–976, 3 2005 (cit. on p. 12).

[84] G. A. Ovsyannikov, K. Y. Constantinian, V. V. Demidov, and Y. N. Khaydukov, „Magnetic proximity effect and superconducting triplet correlations at the cuprate superconductor and oxide spin valve interface“, *Low Temperature Physics*, vol. 42, no. 10, pp. 873–883, 2016 (cit. on p. 12).

[85] C. Lee, F. Katmis, P. Jarillo-Herrero, J. S. Moodera, and N. Gedik, „Direct measurement of proximity-induced magnetism at the interface between a topological insulator and a ferromagnet“, *Nature Communications*, vol. 7, no. 1, p. 12 014, 2016 (cit. on p. 12).

[86] M. Bora and P. Deb, „Magnetic proximity effect in two-dimensional van der Waals heterostructure“, *Journal of Physics: Materials*, vol. 4, no. 3, p. 034 014, 2021 (cit. on p. 12).

[87] J. Li, L. Gu, and R. Wu, „Possible realization and protection of valley-polarized quantum Hall effect in Mn/ W S_2“, *Physical Review B*, vol. 101, no. 2, p. 24 412, 2020 (cit. on p. 12).

[88] J. Qi, X. Li, Q. Niu, and J. Feng, „Giant and tunable valley degeneracy splitting in $MoTe_2$“, *Phys. Rev. B*, vol. 92, p. 121 403, 12 2015 (cit. on p. 12).

[89] L. Ciorciaro, M. Kroner, K. Watanabe, T. Taniguchi, and A. Imamoglu, „Observation of Magnetic Proximity Effect Using Resonant Optical Spectroscopy of an Electrically Tunable $MoSe_2/CrBr_3$ Heterostructure“, *Phys. Rev. Lett.*, vol. 124, p. 197 401, 19 2020 (cit. on p. 12).

[90] S. Tongay, S. S. Varnoosfaderani, B. R. Appleton, J. Wu, and A. F. Hebard, „Magnetic properties of MoS2: Existence of ferromagnetism“, *Applied Physics Letters*, vol. 101, no. 12, p. 123 105, 2012 (cit. on p. 12).

[91] A. Bouarissa, A. Layadi, and H. Maghraoui-Meherzi, „Experimental study of the diamagnetism and the ferromagnetism in MoS2 thin films“, *Applied Physics A*, vol. 126, no. 2, p. 93, 2020 (cit. on p. 12).

[92] J. Frenkel, „On the transformation of light into heat in solids. i“, *Physical Review*, vol. 37, no. 1, pp. 17–44, 1931 (cit. on p. 14).

[93] W. S. Yun, S. W. Han, S. C. Hong, I. G. Kim, and J. D. Lee, „Thickness and strain effects on electronic structures of transition metal dichalcogenides: 2H-MX 2 semiconductors (M = Mo, W; X = S, Se, Te)“, *Phys. Rev. B*, vol. 85, no. 3, pp. 1–5, 2012 (cit. on p. 15).

[94] G. Sallen, L. Bouet, X. Marie, G. Wang, C. R. Zhu, W. P. Han, Y. Lu, P. H. Tan, T. Amand, B. L. Liu, and B. Urbaszek, „Robust optical emission polarization in MoS 2 monolayers through selective valley excitation“, *Phys. Rev. B*, vol. 86, no. 8, pp. 3–6, 2012 (cit. on p. 17).

[95] D. Y. Qiu, F. H. Da Jornada, and S. G. Louie, „Optical spectrum of MoS2: Many-body effects and diversity of exciton states“, *Physical Review Letters*, vol. 111, no. 21, pp. 1–5, 2013 (cit. on pp. 17, 18).

[96] G. L. Bir and G. E. Pikus, *Symmetry and strain-induced effects in semiconductors*. New York: Wiley, 1974 (cit. on p. 19).

[97] M. M. Glazov, T. Amand, X. Marie, D. Lagarde, L. Bouet, and B. Urbaszek, „Exciton fine structure and spin decoherence in monolayers of transition metal dichalcogenides“, *Phys. Rev. B*, vol. 89, p. 201 302, 20 2014 (cit. on p. 19).

[98] H. Hertz, „Über einen Einfluss des ultravioletten Lichtes auf die electrische Entladung“, *Annalen der Physik*, vol. 267, no. 8, pp. 983–1000, 1887 (cit. on p. 23).

[99] A. Einstein, „Über einen die Erzeugung und Verwandlung des Lichtes betreffenden heuristischen Gesichtspunkt“, *Annalen der Physik*, vol. 322, no. 6, pp. 132–148, 1905 (cit. on p. 23).

[100] S. Hüfner, *Photoelectron spectroscopy: principles and applications*. Springer, Berlin, Heidelberg, 2003 (cit. on p. 24).

[101] P. D. Innes, „On the Velocity of the Cathode Particles Emitted by Various Metals under the Influence of Röntgen Rays, and Its Bearing on the Theory of Atomic Disintegration“, *Proceedings of the Royal Society of London. Series A, Containing Papers of a Mathematical and Physical Character*, vol. 79, no. 532, pp. 442–462, 1907 (cit. on p. 24).

[102] C. N. Berglund and W. E. Spicer, „Photoemission Studies of Copper and Silver: Theory“, *Physical Review*, vol. 136, no. 4A, A1030–A1044, 1964 (cit. on p. 24).

[103] A. Damascelli, Z. Hussain, and Z.-X. Shen, „Angle-resolved photoemission studies of the cuprate superconductors“, *Reviews of Modern Physics*, vol. 75, no. 2, pp. 473–541, 2003 (cit. on p. 24).

[104] J. C. Vickerman and I. S. Gilmore, *Surface Analysis: The Principal Techniques, 2^{nd} Edition*. John Wiley & Sons, 2009 (cit. on p. 24).

[105] M. P. Seah and W. A. Dench, „Quantitative electron spectroscopy of surfaces: A standard data base for electron inelastic mean free paths in solids“, *Surface and Interface Analysis*, vol. 1, no. 1, pp. 2–11, 1979 (cit. on p. 24).

[106] S. Tanuma, C. J. Powell, and D. R. Penn, „Calculations of electron inelastic mean free paths. IX. Data for 41 elemental solids over the 50 eV to 30 keV range“, *Surface and Interface Analysis*, vol. 43, no. 3, pp. 689–713, 2011 (cit. on p. 24).

[107] B. Wannberg, „Electron optics development for photo-electron spectrometers“, *Nuclear Instruments and Methods in Physics Research Section A: Accelerators, Spectrometers, Detectors and Associated Equipment*, Special issue in honour of Prof. Kai Siegbahn, vol. 601, no. 1, pp. 182–194, 2009 (cit. on pp. 27, 28).

[108] W. Gerlach and O. Stern, „Der experimentelle Nachweis der Richtungsquantelung im Magnetfeld“, *Zeitschrift für Physik*, vol. 9, no. 1, pp. 349–352, 1922 (cit. on p. 29).

[109] J. Kessler, *Polarized Electrons*, ser. Springer Series on Atomic, Optical, and Plasma Physics. Springer, 1985 (cit. on p. 29).

[110] N. F. Mott, „The scattering of fast electrons by atomic nuclei“, *Proceedings of the Royal Society of London A: Mathematical, Physical and Engineering Sciences*, vol. 124, no. 794, pp. 425–442, 1929 (cit. on p. 29).

[111] C. G. Shull, C. T. Chase, and F. E. Myers, „Electron Polarization“, *Physical Review*, vol. 63, pp. 29–37, 1-2 1943 (cit. on p. 29).

[112] G. Busch, M. Campagna, P. Cotti, and H. C. Siegmann, „Observation of Electron Polarization in Photoemission“, *Physical Review Letters*, vol. 22, pp. 597–600, 12 1969 (cit. on p. 29).

[113] T. Okuda, Y. Takeichi, Y. Maeda, A. Harasawa, I. Matsuda, T. Kinoshita, and A. Kakizaki, „A new spin-polarized photoemission spectrometer with very high efficiency and energy resolution“, *Review of Scientific Instruments*, vol. 79, no. 12, p. 123 117, 2008 (cit. on p. 29).

[114] A. Winkelmann, D. Hartung, H. Engelhard, C.-T. Chiang, and J. Kirschner, „High efficiency electron spin polarization analyzer based on exchange scattering at Fe/W(001)“, *Review of Scientific Instruments*, vol. 79, no. 8, p. 083 303, 2008 (cit. on p. 29).

[115] J. Kirschner and R. Feder, „Spin Polarization in Double Diffraction of Low-Energy Electrons from W(001): Experiment and Theory“, *Physical Review Letters*, vol. 42, pp. 1008–1011, 15 1979 (cit. on p. 29).

[116] C. Tusche, M. Ellguth, A. A. Ünal, C.-T. Chiang, A. Winkelmann, A. Krasyuk, M. Hahn, G. Schönhense, and J. Kirschner, „Spin resolved photoelectron microscopy using a two-dimensional spin-polarizing electron mirror“, *Applied Physics Letters*, vol. 99, no. 3, p. 032 505, 2011 (cit. on p. 29).

[117] J. Osterwalder, „Spin-Polarized Photoemission“, in *Magnetism: A Synchrotron Radiation Approach*, E. Beaurepaire, H. Bulou, F. Scheurer, and J.-P. Kappler, Eds. Berlin, Heidelberg: Springer Berlin Heidelberg, 2006, pp. 95–120 (cit. on p. 29).

[118] D. Pierce, R. Celotta, M. Kelley, and J. Unguris, „Electron spin polarization analyzers for use with synchrotron radiation“, *Nuclear Instruments and Methods in Physics Research Section A: Accelerators, Spectrometers, Detectors and Associated Equipment*, vol. 266, no. 1, pp. 550–559, 1988 (cit. on p. 30).

[119] D. A. Norman, *The design of everyday things*, Revised and expanded edition. New York, New York: Basic Books, 2013 (cit. on p. 30).

[120] E. A. Wood, „Vocabulary of Surface Crystallography“, *Journal of Applied Physics*, vol. 35, no. 4, pp. 1306–1312, 1964 (cit. on p. 33).

[121] R. Wiesendanger and K. Von Klitzing, *Scanning Probe Microscopy: Analytical Methods*, ser. NanoScience and Technology. Springer, 1998 (cit. on p. 34).

[122] R. Wiesendanger and W. Roland, *Scanning Probe Microscopy and Spectroscopy: Methods and Applications*, ser. Scanning Probe Microscopy and Spectroscopy: Methods and Applications. Cambridge University Press, 1994 (cit. on p. 34).

[123] C. J. Chen, *Introduction to scanning tunneling microscopy*. Oxford University Press on Demand, 1993, vol. 4 (cit. on p. 35).

[124] J. Bardeen, „Tunnelling from a Many-Particle Point of View“, *Physical Review Letters*, vol. 6, pp. 57–59, 2 1961 (cit. on p. 35).

[125] C. J. Chen, „Tunneling matrix elements in three-dimensional space: The derivative rule and the sum rule“, *Physical Review B*, vol. 42, pp. 8841–8857, 14 1990 (cit. on p. 35).

[126] C. J. Chen, „Origin of atomic resolution on metal surfaces in scanning tunneling microscopy“, *Physical Review Letters*, vol. 65, pp. 448–451, 4 1990 (cit. on p. 35).

[127] D. Y. Usachov, A. V. Fedorov, O. Y. Vilkov, A. E. Petukhov, A. G. Rybkin, A. Ernst, M. M. Otrokov, E. V. Chulkov, I. I. Ogorodnikov, M. V. Kuznetsov, L. V. Yashina, E. Y. Kataev, A. V. Erofeevskaya, V. Y. Voroshnin, V. K. Adamchuk, C. Laubschat, and D. V. Vyalikh, „Large-Scale Sublattice Asymmetry in Pure and Boron-Doped Graphene“, *Nano Lett.*, vol. 16, no. 7, pp. 4535–4543, 2016 (cit. on p. 44).

[128] D. Y. Usachov, K. A. Bokai, D. E. Marchenko, A. V. Fedorov, V. O. Shevelev, O. Y. Vilkov, E. Y. Kataev, L. V. Yashina, E. Rühl, C. Laubschat, and D. V. Vyalikh, „Cobalt-assisted recrystallization and alignment of pure and doped graphene“, *Nanoscale*, vol. 10, no. 25, pp. 12 123–12 132, 2018 (cit. on p. 46).

[129] V. O. Shevelev, K. A. Bokai, A. A. Makarova, D. Marchenko, O. Y. Vilkov, V. Y. Mikhailovskii, D. V. Vyalikh, and D. Y. Usachov, „Highly Ordered and Polycrystalline Graphene on Co(0001) Intercalated by Oxygen“, *The Journal of Physical Chemistry C*, vol. 124, no. 31, pp. 17 103–17 110, 2020 (cit. on pp. 51, 52).

[130] M. Krivenkov, D. Marchenko, J. Sánchez-Barriga, E. Golias, O. Rader, and A. Varykhalov, „Origin of the band gap in Bi-intercalated graphene on Ir(111)“, *2D Materials*, vol. 8, no. 3, p. 035 007, 2021 (cit. on pp. 51, 59).

[131] T. Cheiwchanchamnangij and W. R. L. Lambrecht, „Quasiparticle band structure calculation of monolayer, bilayer, and bulk MoS_2“, *Phys. Rev. B*, vol. 85, p. 205 302, 20 2012 (cit. on pp. 64, 74).

[132] Z.-Y. Zhao and Q.-L. Liu, „Study of the Layer-Dependent Properties of MoS_2 Nanosheets with Different Crystal Structures by DFT Calculations“, *Catal. Sci. Technol.*, vol. 8, pp. 1867–1879, 7 2018 (cit. on pp. 64, 74).

[133] M. Dresselhaus, G. Dresselhaus, and A. Jorio, *Group Theory - Application to the Physics of Condensed Matter*. Springer, 2008 (cit. on p. 65).

[134] H. A. Kramers, „Théorie générale de la rotation paramagnétique dans les cristaux“, *Proceedings of the Royal Netherlands Academy of Arts and Sciences (in French)*, vol. 33, no. 6–10, pp. 959–972, 1930 (cit. on p. 65).

[135] G. Bihlmayer, Y. Koroteev, P. Echenique, E. Chulkov, and S. Blügel, „The Rashba-effect at metallic surfaces“, *Surf. Sci.*, vol. 600, no. 18, pp. 3888–3891, 2006 (cit. on p. 66).

[136] G. Dresselhaus, A. F. Kip, and C. Kittel, „Cyclotron Resonance of Electrons and Holes in Silicon and Germanium Crystals“, *Phys. Rev.*, vol. 98, p. 368, 1955 (cit. on p. 66).

[137] Y. Bychkov and E. Rashba, „Properties of a 2D electron gas with lifted spectral degeneracy“, *JETP Lett.*, vol. 39, pp. 78–81, 1984 (cit. on p. 66).

[138] Y. A. Bychkov and E. I. Rashba, „Oscillatory effects and the magnetic susceptibility of carriers in inversion layers“, *J. Phys. C Solid State*, vol. 17, no. 33, pp. 6039–6045, 1984 (cit. on p. 66).

[139] Y. Zhang, T. R. Chang, B. Zhou, Y. T. Cui, H. Yan, Z. Liu, F. Schmitt, J. Lee, R. Moore, Y. Chen, H. Lin, H. T. Jeng, S. K. Mo, Z. Hussain, A. Bansil, and Z. X. Shen, „Direct observation of the transition from indirect to direct bandgap in atomically thin epitaxial $MoSe_2$“, *Nature Nanotechnology*, vol. 9, no. 2, pp. 111–115, 2014 (cit. on p. 74).

[140] W. Ku, T. Berlijn, and C.-C. Lee, „Unfolding First-Principles Band Structures“, *Phys. Rev. Lett.*, vol. 104, p. 216 401, 21 2010 (cit. on p. 79).

[141] www.fplo.de (cit. on p. 80).

[142] M. Hehn, S. Padovani, K. Ounadjela, and J. Bucher, „Nanoscale magnetic domain structures in epitaxial cobalt films“, *Physical Review B - Condensed Matter and Materials Physics*, vol. 54, no. 5, pp. 3428–3433, 1996 (cit. on p. 81).

[143] A. Kleibert, V. Senz, J. Bansmann, and P. M. Oppeneer, „Thickness dependence and magnetocrystalline anisotropy of the x-ray transverse magneto-optical Kerr effect at the Co2p edges of ultrathin Co films on W(110)“, *Physical Review B - Condensed Matter and Materials Physics*, vol. 72, no. 14, pp. 1–10, 2005 (cit. on p. 81).

[144] P. D. Johnson, „Spin-polarized photoemission“, *Reports on Progress in Physics*, vol. 60, no. 11, pp. 1217–1304, 1997 (cit. on p. 87).

[145] D. Y. Usachov, A. V. Fedorov, O. Y. Vilkov, A. V. Erofeevskaya, A. S. Vopilov, V. K. Adamchuk, and D. V. Vyalikh, „Formation and lithium doping of graphene on the surface of cobalt silicide“, *Physics of the Solid State*, vol. 57, no. 5, pp. 1040–1047, 2015 (cit. on p. 98).

[146] D. Y. Usachov, A. V. Tarasov, K. A. Bokai, V. O. Shevelev, O. Y. Vilkov, A. E. Petukhov, A. G. Rybkin, I. I. Ogorodnikov, M. V. Kuznetsov, M. Muntwiler, F. Matsui, L. V. Yashina, C. Laubschat, and D. V. Vyalikh, „Site- and Spin-Dependent Coupling at the Highly Ordered *h*-BN/Co(0001) Interface“, *Phys. Rev. B*, vol. 98, p. 195 438, 19 2018 (cit. on p. 99).

Includes only important ones, marked with keyword "a".

Publications related to this thesis

1 V. Voroshnin, A. V. Tarasov, K. A. Bokai, A. Chikina, B. V. Senkovskiy, N. Ehlen, D. Y. Usachov, A. Grüneis, M. Krivenkov, J. Sánchez-Barriga, and A. Fedorov, „Direct Spectroscopic Evidence of Magnetic Proximity Effect in MoS_2 Monolayer on Graphene/Co“, *ACS Nano*, vol. 16, no. 5, pp. 7448–7456, 2022.

Other publications

2 S. Borisenko, A. Fedorov, A. Kuibarov, M. Bianchi, V. Bezguba, P. Majchrzak, P. Hofmann, P. Baumgärtel, V. Voroshnin, Y. Kushnirenko, J. Sánchez-Barriga, A. Varykhalov, R. Ovsyannikov, I. Morozov, S. Aswartham, O. Feia, L. Harnagea, S. Wurmehl, A. Kordyuk, A. Yaresko, H. Berger, and B. Büchner, „Fermi surface tomography“, *Nature Communications*, vol. 13, no. 1, p. 4132, 2022.

3 D. V. Potorochin, R. Kurleto, O. J. Clark, E. D. L. Rienks, J. Sánchez-Barriga, F. Roth, V. Voroshnin, A. Fedorov, W. Eberhardt, B. Büchner, and J. Fink, „Lifetime of quasiparticles in the nearly free electron metal sodium“, *Phys. Rev. B*, vol. 106, p. 125 138, 12 2022.

4 A. Kuibarov, A. Fedorov, V. Bezguba, H. Berger, A. Yaresko, V. Voroshnin, A. Kordyuk, P. Baumgärtel, B. Büchner, and S. Borisenko, „Isolated fourfold fermion in BiTeI“, *Phys. Rev. B*, vol. 105, p. 235 112, 23 2022.

5 B. Schrunk, Y. Kushnirenko, B. Kuthanazhi, J. Ahn, L.-L. Wang, E. O'Leary, K. Lee, A. Eaton, A. Fedorov, R. Lou, V. Voroshnin, O. J. Clark, J. Sánchez-Barriga, S. L. Bud'ko, R.-J. Slager, P. C. Canfield, and A. Kaminski, „Publisher Correction: Emergence of Fermi arcs due to magnetic splitting in an antiferromagnet“, *Nature*, vol. 605, no. 7909, E5–E5, 2022.

6 B. Schrunk, Y. Kushnirenko, B. Kuthanazhi, J. Ahn, L.-L. Wang, E. O'Leary, K. Lee, A. Eaton, A. Fedorov, R. Lou, V. Voroshnin, O. J. Clark, J. Sánchez-Barriga, S. L. Bud'ko, R.-J. Slager, P. C. Canfield, and A. Kaminski, „Emergence

of Fermi arcs due to magnetic splitting in an antiferromagnet“, *Nature*, vol. 603, no. 7902, pp. 610–615, 2022.

7 Y. Falke, N. Ehlen, G. Marini, A. V. Fedorov, V. Voroshnin, B. V. Senkovskiy, K. Nikonov, M. Hoesch, T. K. Kim, L. Petaccia, G. Di Santo, T. Szkopek, G. Profeta, and A. Grüneis, „Coupling to zone-center optical phonons in VSe_2 enhanced by charge density waves“, *Phys. Rev. B*, vol. 104, p. 235 137, 23 2021.

8 A. M. Shikin, A. A. Rybkina, D. A. Estyunin, I. I. Klimovskikh, A. G. Rybkin, S. O. Filnov, A. V. Koroleva, E. V. Shevchenko, M. V. Likholetova, V. Voroshnin, A. E. Petukhov, K. A. Kokh, O. E. Tereshchenko, L. Petaccia, G. Di Santo, S. Kumar, A. Kimura, P. N. Skirdkov, K. A. Zvezdin, and A. K. Zvezdin, „Non-monotonic variation of the Kramers point band gap with increasing magnetic doping in BiTeI“, *Scientific Reports*, vol. 11, no. 1, p. 23 332, 2021.

9 A. A. Rybkina, S. O. Filnov, A. V. Tarasov, D. V. Danilov, M. V. Likholetova, V. Voroshnin, D. A. Pudikov, D. A. Glazkova, A. V. Eryzhenkov, I. A. Eliseyev, V. Y. Davydov, A. M. Shikin, and A. G. Rybkin, „Quasi-freestanding graphene on SiC(0001) via cobalt intercalation of zero-layer graphene“, *Phys. Rev. B*, vol. 104, p. 155 423, 15 2021.

10 A. S. Ketterl, B. Andres, M. Polverigiani, V. Voroshnin, C. Gahl, K. A. Kokh, O. E. Tereshchenko, E. V. Chulkov, A. Shikin, and M. Weinelt, „Effect of Rashba splitting on ultrafast carrier dynamics in BiTeI“, *Phys. Rev. B*, vol. 103, p. 085 406, 8 2021.

11 M. Yao, K. Manna, Q. Yang, A. Fedorov, V. Voroshnin, B. Valentin Schwarze, J. Hornung, S. Chattopadhyay, Z. Sun, S. N. Guin, J. Wosnitza, H. Borrmann, C. Shekhar, N. Kumar, J. Fink, Y. Sun, and C. Felser, „Observation of giant spin-split Fermi-arc with maximal Chern number in the chiral topological semimetal PtGa“, *Nature Communications*, vol. 11, no. 1, p. 2033, 2020.

12 S. Borisenko, V. Bezguba, A. Fedorov, Y. Kushnirenko, V. Voroshnin, M. Sturza, S. Aswartham, and A. Yaresko, „Strongly correlated superconductor with polytypic 3D Dirac points“, *npj Quantum Materials*, vol. 5, no. 1, pp. 1–8, 2020.

13 I. I. Klimovskikh, M. M. Otrokov, D. Estyunin, S. V. Eremeev, S. O. Filnov, A. Koroleva, E. Shevchenko, V. Voroshnin, A. G. Rybkin, I. P. Rusinov, M. Blanco-Rey, M. Hoffmann, Z. S. Aliev, M. B. Babanly, I. R. Amiraslanov, N. A. Abdullayev, V. N. Zverev, A. Kimura, O. E. Tereshchenko, K. A. Kokh, L. Petaccia, G. Di Santo, A. Ernst, P. M. Echenique, N. T. Mamedov, A. M. Shikin, and E. V. Chulkov, „Tunable 3D/2D magnetism in the (MnBi2Te4)(Bi2Te3)m topological insulators family“, *npj Quantum Materials*, vol. 5, no. 1, pp. 1–9, 2020.

14 A. Chikina, A. Fedorov, D. Bhoi, V. Voroshnin, E. Haubold, Y. Kushnirenko, K. H. Kim, and S. Borisenko, „Turning charge-density waves into Cooper pairs“, *npj Quantum Materials*, vol. 5, no. 1, pp. 1–5, 2020.

15 A. G. Rybkin, A. A. Rybkina, A. V. Tarasov, D. A. Pudikov, I. I. Klimovskikh, O. Y. Vilkov, A. E. Petukhov, D. Y. Usachov, D. A. Estyunin, V. Voroshnin, A. Varykhalov, G. Di Santo, L. Petaccia, E. F. Schwier, K. Shimada, A. Kimura, and A. M. Shikin, „A new approach for synthesis of epitaxial nano-thin Pt5Gd alloy via intercalation underneath a graphene“, *Applied Surface Science*, vol. 526, p. 146 687, 2020.

16 S. O. Filnov, I. I. Klimovskikh, D. A. Estyunin, A. V. Fedorov, V. Voroshnin, A. V. Koroleva, A. G. Rybkin, E. V. Shevchenko, Z. S. Aliev, M. B. Babanly, I. R. Amiraslanov, N. T. Mamedov, E. F. Schwier, K. Miyamoto, T. Okuda, S. Kumar, A. Kimura, V. M. Misheneva, A. M. Shikin, and E. V. Chulkov, „Probe-dependent Dirac-point gap in the gadolinium-doped thallium-based topological insulator $TlBi_{0.9}Gd_{0.1}Se_2$“, *Phys. Rev. B*, vol. 102, p. 085 149, 8 2020.

17 K. A. Bokai, A. V. Tarasov, V. O. Shevelev, O. Y. Vilkov, A. A. Makarova, D. Marchenko, A. E. Petukhov, M. Muntwiler, A. V. Fedorov, V. Voroshnin, L. V. Yashina, C. Laubschat, D. V. Vyalikh, and D. Y. Usachov, „Hybrid h-BN–Graphene Monolayer with B–C Boundaries on a Lattice-Matched Surface“, *Chemistry of Materials*, vol. 32, no. 3, pp. 1172–1181, 2020.

18 A. M. Shikin, A. A. Rybkina, D. A. Estyunin, D. M. Sostina, I. I. Klimovskikh, V. Voroshnin, A. G. Rybkin, K. A. Kokh, O. E. Tereshchenko, L. Petaccia, G. Di Santo, A. Kimura, P. N. Skirdkov, K. A. Zvezdin, and A. K. Zvezdin, „Dirac cone intensity asymmetry and surface magnetic field in V-doped and pristine topological insulators generated by synchrotron and laser radiation“, *Scientific Reports*, vol. 8, no. 1, p. 6544, 2018.

19 N. Ehlen, J. Hall, B. V. Senkovskiy, M. Hell, J. Li, A. Herman, D. Smirnov, A. Fedorov, V. Voroshnin, G. D. Santo, L. Petaccia, T. Michely, and A. Grüneis, „Narrow photoluminescence and Raman peaks of epitaxial MoS_2 on graphene/Ir(1 1 1)“, *2D Materials*, vol. 6, no. 1, p. 011 006, 2018.

20 A. M. Shikin, A. A. Rybkina, D. A. Estyunin, D. M. Sostina, V. Voroshnin, I. I. Klimovskikh, A. G. Rybkin, Y. A. Surnin, K. A. Kokh, O. E. Tereshchenko, L. Petaccia, G. Di Santo, P. N. Skirdkov, K. A. Zvezdin, A. K. Zvezdin, A. Kimura, E. V. Chulkov, and E. E. Krasovskii, „Signatures of in-plane and out-of-plane magnetization generated by synchrotron radiation in magnetically doped and pristine topological insulators“, *Phys. Rev. B*, vol. 97, p. 245 407, 24 2018.

21 A. G. Rybkin, A. A. Rybkina, M. M. Otrokov, O. Y. Vilkov, I. I. Klimovskikh, A. E. Petukhov, M. V. Filianina, V. Voroshnin, I. P. Rusinov, A. Ernst, A. Arnau, E. V. Chulkov, and A. M. Shikin, „Magneto-Spin–Orbit Graphene: Interplay between Exchange and Spin–Orbit Couplings“, *Nano Letters*, vol. 18, no. 3, pp. 1564–1574, 2018.

Summary

The molybdenum disulfide (MoS_2) monolayer is a mechanically and chemically robust direct band semiconductor. Its valley properties suggest spin and valley-related spintronic, valleytronic, and optoelectronic applications. Here we investigated the possibility of the control over electronic and spin structures of MoS_2 via interaction with a substrate. Control over electronic and spin structure is essential for controlling optical properties.

We used two environmental approaches to break spin degeneracy. First, we placed MoS_2 monolayer in an electric potential gradient, and second, to the equivalent of a strong in-plane magnetic field which was created via a magnetic proximity effect. For this, we fabricated two systems: MoS_2 monolayer on a gold monocrystal and MoS_2 monolayer on graphene on a cobalt thin film.

We modified the previously suggested procedure for MoS_2 monolayer synthesis on the Au(111) surface and obtained ≈0.4 MoS_2 monolayer coverage using the MBE method. The coverage demonstrated a 10×10 superstructure and consisted of equally distributed and similarly oriented domains of ≈30 nm size. The combination of DFT simulations and spin-resolved photoemission spectroscopy confirmed the presence of a Rashba-like in-plane spin splitting of the MoS_2 valence band states in regions with $\vec{k} \neq 0$ with the exception of the $\overline{\mathrm{K}}$ point due to the symmetry reasons.

We moved on to the investigation of the possibility of magnetic proximity effect to manipulate the MoS_2 monolayer spin structure, including the regions of the high symmetry points. The regions of $\overline{\mathrm{K}}$ and $\overline{\mathrm{K}'}$ points are the most intriguing, as the MoS_2 monolayer direct band gap is located there. Shifting valence and conduction band states relative in energy to each other in these regions should provide control over the valley splitting of the MoS_2 monolayer. On the other hand, tilting the spin direction of these states toward the in-plane spin direction should drastically change optical selection rules and brighten a dark exciton.

We considered a cobalt thin film substrate as our magnetic proximity test subject due to its magnetic anisotropy in the in-plane direction. We used the CVD method to cover it with graphene and then the MBE method to produce ≈0.4 MoS_2 monolayer coverage atop. We placed graphene between MoS_2 monolayer and cobalt thin film to avoid exciton quenching from MoS_2 by metallic substrate. For the fabrication of the MoS_2 monolayer atop the graphene/Co substrate, we modified the procedure proposed for the fabrication of MoS_2 atop a graphene/Ir substrate.

The ≈0.4 monolayer MoS_2 coverage demonstrated a large area of crystalline domains of more than 200 nm size. Four MoS_2 unit cells correspond to five graphene unit cells. This suggests a 5×5 superstructure which is confirmed via LEED imaging. On the other hand, STM imaging with atomic resolution demonstrates a quasi-periodic structure with several types of moiré patterns. Because of the equal possibility of MoS_2 epitaxial growth along **A** and **B** graphene sublattices, MoS_2 monolayer demonstrates an equal amount of 180° rotated domains (mirror domains).

We first confirmed the presence of the magnetic proximity effect by observing ≈20 meV Zeeman in-plane spin splitting of MoS_2 valence band states in the region of $\overline{\Gamma}$ in both DFT calculations and spin-resolved photoemission measurements. In the region of $\overline{\mathrm{K}}$, both calculations and measurements agree on 15% spin-polarisation of the valence band states. In contrast, in the conduction band states, DFT calculations suggest 100% spin-polarisation of the states. This result implies the brightening of MoS_2 monolayer dark excitons. In the case of out-of-plane cobalt magnetization, DFT calculations predict ≈16 meV spin splitting at $\overline{\Gamma}$ and ≈8 meV spin splitting of $\overline{\mathrm{K}}$ and $\overline{\mathrm{K}'}$ valleys.

In order to investigate MoS_2 conduction band states, we doped MoS_2/graphene/Co with potassium atoms. The resulting system featured potassium atoms being intercalated underneath MoS_2, which increased the distance between MoS_2 monolayer and cobalt film. Spin-resolved measurements showed no in-plane spin splitting of MoS_2 valence band states in the region of $\overline{\Gamma}$ and MoS_2 conduction band states in the region of $\overline{\mathrm{K}}$.

As graphene is buffering MoS_2 monolayer from the cobalt film to prevent a potential exciton quenching, we investigated the role of graphene in the magnetic proximity effect. In our computations, we replaced graphene with graphene bi-layer, h-BN, vacuum, and copper monolayer and concluded that the effect strongly depends on the orbital overlap. MoS_2/h-BN/Co show similar results, while MoS_2/graphene bilayer/Co and MoS_2/vacuum/Co demonstrate almost zero magnetic proximity effect.

In conclusion, we proved that MoS_2 monolayer spin structure can be manipulated via interaction with a substrate using spectroscopic techniques and DFT calculations. We are looking forward to further optical studies to investigate the possibilities of optical control of MoS_2 and group VI dichalcogenides via magnetic proximity effect.